Politecnico di Torino

Master's Degree in Energy and Nuclear Engineering
Graduation Session: October 2024

Sono-chemistry for Hydrogen Production: Cavitation Field Characterization in a Cylindrical Vessel

Supervisor:
Massimo Santarelli

Co-supervisor:
Franco Cotana
Piergiovanni Domenighini

Candidate:
Davide Segantini

Abstract

This thesis, conducted in collaboration with the 'Università degli Studi di Perugia', aims to analyze the potential of sonolysis and photo-sonolysis in the context of hydrogen production. The primary objective of this research is to investigate the phenomena of acoustic cavitation within a cylindrical sono-reactor and to determine the feasibility of accurately simulating these phenomena within a MATLAB environment.

To achieve this objective, a methodology composed of two steps has been employed. The first step involves the implementation of a mathematical model within the MATLAB environment. The second step focuses on the experimental acquisition of pressure data within the reactor using a dedicated measurement setup, followed by signal post-processing in MATLAB.

This methodology yield time-evolving pressure maps of the reactor and pressure-height plots at specific points, which allows for a direct comparison between the simulated and experimental data. The results are significant, as they support the thesis that the acoustic disturbances predicted by the mathematical modeling simulations differ considerably from the experimental measurements, challenging what is commonly accepted in the literature as a certainty. The discrepancies observed are primarily due to the simplifying assumptions made in the mathematical modeling simulations. These assumptions result in an acoustic cavitation field characterized by symmetries within the cylindrical section and along various heights, which are not evident in the experimentally measured and post-processed results.

These findings underscore the need to refine the mathematical model by integrating additional factors to achieve more accurate simulations that closely align with experimental data. Potential enhancements include incorporating fluid viscosity, accounting for ultrasonic effects, and considering acoustic scattering between pressure waves and bubbles. Additionally, the integration of molecular-scale computing models could offer further insights and improvements.

In the light of these findings, further studies should be conducted to fully understand the cavitation field phenomena, with the goal of comprehending the full potential of sonolysis and its synergic effect with photolysis and the more established electrolysis.

Contents

Chapter 1

Introduction

1.1 Hydrogen molecule H_2

The existence of hydrogen is known by human kind from centuries — 1500s —, but the credits for its discovery were attributable to Henry Cavendish in 1766: he made a series of experiments regarding the formation of hydrogen from water and its combustion, forming water again. This is the reason why Antoine Lavoisier thought about this gas as a 'generator of water', and so the name hydro-gen — form Greek '*hydro*' and '*genes*' — [1] [25].

Hydrogen is easily the most abundant element of the universe, as the analysis of the light spectrum emitted by the stars has highlighted [25]: Jupiter, for example, is a planet mostly composed by this molecule [1], but also the Sun, our closest star, is made of hydrogen up to 90% [25]. On the Earth, with oxygen and silicon, hydrogen is one of the most spread elements. In its elementary state is very rare, but combined is abundant: it is found in the greatest quantity as water — and so combined with oxygen —, but it can be found in large quantities also combined with carbon, oxygen and other elements as fundamental organic compounds [25].

1.1.1 Characteristics

In nature hydrogen is a mixture of two different isotopes: ordinary hydrogen, or protium, that contains one proton and one electron; and deuterium, that includes also a neutron. Normally hydrogen gas is a mixture with a proportion of normal hydrogen and deuterium of 3200:1 [25].

In most of the cases, when hydrogen is not bounded to another element, it is found in its molecular form, namely H_2: this molecule, composed by two hydrogen atoms, can have two different energy states, called orto-hydrogen — or normal-hydrogen — and para-hydrogen. The difference between these two states is clear from the analysis of the molecule nuclei: in fact, considering only the case of ordinary hydrogen and neglecting the deuterium, molecular hydrogen contains two protons and two electrons, and each proton is characterized by a spin that manifest an angular momentum of the nuclei. When the two spins are parallel — and generates two nuclei angular momentum in the same direction — the molecule is orto-hydrogen, while in the case of anti-parallelism of protons' spin the molecule is para-hydrogen.

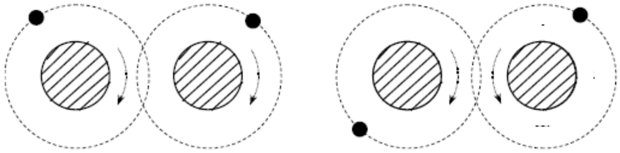

Figure 1.1: On the left: orto-hydrogen — parallel spins —. On the right: para-hydrogen [25]

When these two different molecular form of hydrogen are in equilibrium, the mixture is called equilibrium-hydrogen: this equilibrium is function of the temperature, and for example at ambient temperature the equilibrium-hydrogen is composed by 75% in volume of normal-hydrogen and the rest 25% of para-hydrogen. The equilibrium-hydrogen has properties that are the weighted average of the normal hydrogen properties and the para-hydrogen. Tables 1.1, 1.2, 1.3, 1.4 and 1.5 illustrate the main characteristics of the orto and para-hydrogen. [25].

Table 1.1: Some physical and thermo-physical properties of normal and para-hydrogen at normal temperature and pressure (NTP) point, from ISO/TR 15916:2004(E) cited in [25].

Property	**Normal hydrogen**	**Para-hydrogen**
Temperature, K	293.15	293.15
Pressure (absolute), kPa	101325	101325
Density, kg/m^3	0.08376	0.08376
Specific heat at constant pressure (c_p), kJ/kg· K	14.33	14.89
Specific heat ratio (c_p/c_v)	1416	1383
Enthalpy, kJ/kg	4129.1	4097.7
Internal energy, kJ/kg	2919.5	2888.0
Entropy, kJ/kgK	70251	64437
Velocity of sound, m/s	1294	1294
Viscosity, μ Pa· s	8.81	8.81
Thermal conductivity, mW/m· K	183.8	191.4

Heat of conversion from normal to parahydrogen at 300 K, kJ/kg	27.56	-
Volume expansivity, K^{-1}	0.00333	0.00333

Table 1.2: Some physical and thermo-physical properties of normal and para-hydrogen at critical point (CP), from ISO/TR 15916:2004(E) cited in [25].

Property	**Normal hydrogen**	**Para-hydrogen**
Temperature, K	33.19	32.976
Pressure (absolute), kPa	1315	1292.8
Density, kg/m^3	30.12	31.43
Latent heat of vaporization, kJ/kg	0	0
Specific heat at constant pressure (c_p), kJ/kg· K	Very large	Very large
Specific heat ratio (c_p/c_v)	Large	Large
Enthalpy, kJ/kg	577.4	38.5
Internal energy, kJ/kg	-	2.8
Entropy, kJ/kg · K	27.07	17.6
Velocity of sound, m/s	-	350
Viscosity, μ Pa· s	3.5 (estimate)	3.5
Thermal conductivity, mW/m· K	Anomalously large	Anomalously large

Table 1.3: Some physical and thermo-physical properties of normal and para-hydrogen at normal boiling point (NBP), from ISO/TR 15916:2004(E) cited in [25].

Property	**Normal hydrogen**	**Para-hydrogen**
Temperature, K	20.930	20.268
Pressure (absolute), kPa	101325	101325
Density, kg/m^3	1.331 (V) 70.96 (L)	1.3338 (V) 70.78 (L)
Latent heat of vaporization, kJ/kg	446.0	445.6
Specific heat at constant pressure (c_p), kJ/kg· K	12.20 (V) 9.772 (L)	12.15 (V) 9.688 (L)

Specific heat ratio (c_p/c_v)	1.683 (V) 1.698 (L)	1.869 (V) 1.688 (L)
Enthalpy, kJ/kg	717.98 (V) 272.0 (L)	189.3 (V) -256.3 (L)
Internal energy, kJ/kg	641.9 (V) 270.7 (L)	113.6 (V) -257.7 (L)
Entropy, kJ/kg · K	39.16 (V) 17.32 (L)	29.97 (V) 7.976 (L)
Velocity of sound, m/s	357 (V) 1101 (L)	355 (V) 1093 (L)
Viscosity, μ Pa· s	1.1 (V) 13.2 (L)	1.1 (V) 13.2 (L)
Thermal conductivity, mW/m · K	16.9 (V) 99.0 (L)	16.9 (V) 99.0 (L)
Volume expansivity, K^{-1}	0.0642 (V) 0.0164 (L)	0.0642 (V) 0.0164 (L)
Heat of conversion from normal to parahydrogen, kJ/kg	527.14	-

Table 1.4: Some physical and thermo-physical properties of normal and para-hydrogen at triple point (TP), from ISO/TR 15916:2004(E) cited in [25].

Property	**Normal hydrogen**	**Para-hydrogen**
Temperature, K	13.957	13.803
Pressure (absolute), kPa	7.205	7.042
Density, kg/m^3	0.1298 (V) 77.21 (L) 86.71 (S)	0.1256 (V) 77.021 (L) 86.50 (S)
Specific heat at constant pressure (c_p), kJ/kg· K	10.53 (V) 6.563 (L) - (S)	10.52 (V) 6.513 (L) - (S)
Specific heat ratio (c_p/c_v)	1.695 (V) 1.388 (L) - (S)	1.693 (V) 1.382 (L) - (S)
Latent heat of vaporization, kJ/kg	452.0	449.2
Latent heat of fusion, kJ/kg	58.09	58.29

Latent heat of sublimation, kJ/kg	-	507.39
Enthalpy, kJ/kg	669.67 (V) 217.6 (L) 159.5 (S)	140.3 (V) -308.9 (L) -367.2 (S)
Internal energy, kJ/kg	612.52 (V) 215.8 (L) 157.7 (S)	84.23 (V) -309.0 (L) -367.3 (S)
Entropy, kJ/kg $\cdot$ K	46.4 (V) 14.2 (L) 10.1 (S)	37.52 (V) 4.961 (L) 0.739 (S)
Velocity of sound, m/s	307 (V) 1282 (L) - (S)	305 (V) 1273 (L) - (S)
Viscosity, μ Pa$\cdot$ s	0.74 (V) 26.0 (L) - (S)	0.74 (V) 26.0 (L) - (S)
Thermal conductivity, mW/m$\cdot$ K	12.4 (V) 73.0 (L) 900 (S)	12.4 (V) 73.0 (L) 900 (S)
Volume expansivity, K^{-1}	0.0752 (V) 0.0102 (L)	0.0752 (V) 0.0102 (L) 0.00494 (S)

Table 1.5: Some other physical and thermo-physical properties of normal and para-hydrogen, from ISO/TR 15916:2004(E) cited in [25].

Property	**Normal hydrogen**	**Para-hydrogen**
Molecular mass	2.01564	2.01594
Equivalent volume gas at NTP/volume liquid NBP	847.1	845.1
Equivalent volume gas at CP/volume liquid NBP	2.357	2.252
Equivalent volume gas at NBP/volume liquid at NBP	53.30	52.91
Equivalent volume gas at TP/volume liquid NBP	546.3	563.8
Equivalent volume liquid at TP/volume liquid NBP	0.9190	0.9190

Equivalent volume solid at TP/volume liquid NBP	0.8184	0.8181
Pressure required to maintain NBP liquid density in NTP GH (fixed volume, no venting), MPa	-	172 (calculated)
Joule-Thomson maximum inversion temperature, K	-	200
Diffusion coefficient in NTP air, cm^2/s	-	0.61
Diffusion velocity in NTP air, cm/s	-	52.0
Buoyant velocity in NTP air, m/s	-	1.2 to 9
Vaporization rate (steady state) of liquid pool without burning, mm/s	-	0.42 to 0.83

At ambient temperature, hydrogen reveal itself as a colourless and odourless gas, that is insoluble in water. Even if generally it is not really active at low temperature, in presence of catalysts or in an higher temperature environment, it is able to generate numerous chemical reactions.
Furthermore, hydrogen has the highest content of energy per unit mass with respect to all the other fuels, with a lower heating value — LHV — of 120 MJ/kg and a higher heating value — HHV — of 142 MJ/kg [25].

Hydrogen gas is really volatile and flammable, and in some circumstances it can detonate when mixed with air. For this reason, hydrogen mixtures should be handled with care and the systems involved in its applications should be carefully designed and checked regularly, in order to limit the possibility of losses or mass accumulations and avoid to reach the lower limit of concentration that brings to ignition in air.
Table 1.6 shows all the relevant properties about hydrogen, methane and gasoline vapors for a direct comparison. The main safety problem about hydrogen is the very low ignition energy in air: this means that a mixture of air and hydrogen in the right proportion can fulfill the combustion reaction requirement with the need of a very low input energy, that can be for example a simple spark. Another safety problem that is important to take care of when hydrogen burns is that the generated flame is invisible to the naked eye.
The lower limit of concentration of hydrogen for hydrogen-air mixture combustion is similar to the one for methane-air mixture, anyway higher than the lower limit for gasoline-air mix. Nevertheless, it is important to notice that the higher limit of concentration of hydrogen for combustion is much higher than both methane and gasoline, meaning that there is a wide range of concentrations to make combustion possible: this means that any kind of hydrogen accumulation in airy environments should be completely avoided for the sake of safety.

Lower limit of concentration of hydrogen is also important for hydrogen production, as the case of alkaline electrolyzers, where the lower limit of hydrogen concentration for hydrogen-oxygen mixtures should not exceed the 2% of volume fraction for safety reasons.
Fortunately prevention of hydrogen accumulation in enclosed spaces is easy to realize thanks to the high diffusion coefficient of hydrogen in air, that permits, with the help of a low density value, to scatter more rapidly than the other gases. In fact, hydrogen is the gaseous element with the lowest molecular weight and the highest diffusion velocity in air, other than the lowest viscosity and density: these properties make hydrogen the fastest in escaping velocity through small orifices, precisely 2.8 times faster than methane.
Furthermore, the hydrogen flame emissivity is low, resulting in a lower heat transfer by radiance.
All in all, taking into account all the properties just analyzed, hydrogen does not show more dangers respect other liquid or gaseous fuels commonly used [25].

Properties	**Gasoline**	**Methane**	**Hydrogen**
Density (kg/m^3)	4.40	0.717	0.084
Diffusion coefficient in air (cm^3/s)	0.05	0.16	0.61
Specific heat at constant pressure c_p (kJ/kg·K)	1.2	2.22	14.89
Ignition limit in air (%vol)	1.0÷7.6	5.3÷15.0	4.0÷75.0
Ignition energy in air (mJ)	0.24	0.29	0.02
Auto-ignition temperature (°C)	228÷471	540	585
Flame temperature in air (°C)	2197	1875	2045
Explosion energy (gTNT/kJ)	0.25	0.19	0.17
Flame emissivity (%)	38	39	21

Table 1.6: Physical characteristics of Gasoline, Methane and Hydrogen for comparison [25].

The reason why hydrogen is considered an interesting molecule nowadays is due to multiple factors: it can be used as primary source for many chemical operations, and the most relevant one is the synthesis of ammonia NH_3 for agricultural fertilizers — Haber process — [25] [1]. Other interesting purposes are [25] [1]:

- the sulfur removal from fuels during oil refining processes;
- the production of cyclohexane and methanol for different scopes;
- the production of synthetic fuels;

- the use in hydrogenation processes of oils to form fats, such as margarine;
- the creation of a protective atmosphere in the formation of flat glass sheets;
- the use as flushing gas during the manufacturing of silicon chips.

Currently, in NASA's spatial programs hydrogen is used as fuel for direct combustion, using it in its liquid state and mixing it with liquid oxygen. Furthermore, Space Shuttles and other kind of rockets are equipped with fuel cells that, working with hydrogen and oxygen as main inputs, are used to generate electricity. Moreover, pure water is a byproduct of this technology, and it is used for alimentary purposes [25].

As it has been shown by previous examples, hydrogen can be used in a multitude of ways and for very different scopes, in particular the last example highlighted the possibility of using hydrogen as a clean source of energy. This is the reason why hydrogen is seen as a clean fuel with high potentiality for future decarbonisation scenarios: when used as direct fuel, it burns and generates only water as a waste product; while when used in a hydrogen based fuel cell, it gives back, as a byproduct of red-ox reaction, only pure water; so it can be seen as a "pollution-free" source of energy [1].

1.1.2 Production means

'Hydrogen economy' includes all the steps that start from hydrogen production and end to hydrogen end-use, and involve packaging, distribution, storage and transfer [2]: "Hydrogen economy is a vision of an energy delivery infrastructure based on hydrogen as a carbon-free energy carrier. [...] An alternative energy economy in the form of a parallel power and transportation infrastructure is needed, including technical solutions for energy-efficient hydrogen production, storage technology and delivery infrastructure" [3].

In this context, hydrogen production has an important role in the energy transition and in the whole hydrogen supply chain, since this step is determining the majority of both emitted pollutants and hydrogen price. "Hydrogen production is the main step towards transitioning to hydrogen economy, wherein hydrogen will replace fossil fuels" [12].

Since molecular hydrogen is scarce in nature, it must be extracted from sources that contain hydrogen within their molecular structure, the most important of which are fossil fuels, biomass, and water. In order to retrieve it, it is necessary to exploit a series of chemical reactions and processes that require energy: the combination of the natural source of hydrogen and the energy exploited to obtain it determine the amount of pollutants emitted, other than the hydrogen selling price. Energy sources can be renewable — like solar, wind, tidal, hydro, geothermal, etc. — or non-renewable — combustion of fossil fuels — and exploited in terms of thermal energy or electrical energy, depending on the typology of process used to retrieve hydrogen from its carrier [12].

1.1.2.1 Reforming

The most used processes for hydrogen production nowadays are the reforming processes, especially steam reforming with natural gas as feedstock. These processes in general require hydrocarbon fossil fuels as hydrogen carrier and heat as input energy — to reach the high temperature needed by the respective chemical reactions —. The main reforming methods are catalytic steam reforming, partial oxidation and autothermal reforming [12]:

- **Catalytic Steam Reforming (CSR)**: this process is based on the following chemical reactions:

  $$C_nH_m + nH_2O \rightarrow nH_2 + \left(\frac{n+m}{2}\right) CO; \qquad \Delta H^0_{298} > 0 \tag{1.1}$$

  $$CO + H_2O \rightarrow CO_2 + H_2; \qquad \Delta H^0_{298} = -40.4 \;\; kJmol^{-1} \tag{1.2}$$

  Reaction 1.1 is the steam reforming reaction for a general hydrocarbon chain: it is highly endothermic, requiring high temperature — above 600 K — and pressure — around 2-3 MPa — even in presence of Fe and Ni based catalyst.
  Reaction 1.2 is the water gas shift reaction (WGSR) that occurs spontaneously in two stages — CO is very reactive —, namely high temperature shift (HTS) at 350°C and low temperature shift (LTS) at 200°C.
  Steam reforming process efficiency is around 65-70%, depending also on the source of heat and the type of hydrocarbon used as source of hydrogen. Steam reforming of light hydrocarbons is a well established industrial process, and in particular natural gas (CH_4) CSR (Steam Methane Reforming, SMR) is the economically, technically and commercially best way to produce hydrogen, mainly used in petrochemical and chemical industries. Other interesting alternative hydrocarbons used for this process are methanol and ethanol.

- **Partial Oxidation (POX)**: as the process name suggest, it is based on the oxidation of an hydrocarbon made with a substoichiometric amount of oxygen from air, to obtain a stream containing H_2. The chemical reaction is:

  $$C_xH_yO_z + \frac{x-z}{2}(O_2 + 3.76N_2) \rightarrow xCO + \frac{y}{2}H_2 + 3.76\frac{x-z}{2}N_2 \tag{1.3}$$

  Noticeable from reaction 1.3 is the significant production of carbon monoxide, related to a presence of O_2 less than stoichiometric proportions. This process, even without a catalyst, is faster than steam reforming, and the presence of a catalyst actually worsen the efficiency and the cost. The operational temperature are 1200-1500 °C for non-catalytic (Texaco) process, and 1000 °C for a catalytic reaction.

- **Autothermal reforming (ATR)**: this process is also known as oxidative steam reforming, and is a combination of catalytic reforming and POX. The reaction in fact is:

$$\begin{aligned} C_xH_yO_z + n(O_2 + 3.76N_2) + (x - 2n - z)H_2O \rightarrow xCO \\ + \left(x - 2n - z + \frac{y}{2}\right) H_2 + 3.76N_2 \end{aligned} \tag{1.4}$$

  Reaction 1.4 is also known as autothermal since the endotermic steam reaction is feed by the exothermicity of the POX reaction.
  This kind of process has several advantages that are a lower operating temperature, a better heat integration and a faster start-up.
  Particularly promising is the oxidative methanol reforming, that is simply an autothermal reaction involving methanol and that features an overall thermally neutral reaction, or modestly exothermic. Furthermore, the presence of a Pd-ZnO catalyst can improve the whole process.

1.1.2.2 Gasification

Systems based on gasification are similar to POX, described in the Subsubsection 1.1.2.1: these can use different feedstocks, like coal, petroleum coke, municipal and hazardous waste and biomass. The gasification technology can be quite different depending on the used hydrogen carrier, and considering coal as example, it can be summarized in 3 different steps, that are the conversion of the feedstock in the presence of an oxidant to a syngas at high temperature — 1000-1500°C —, catalytic shift reaction and hydrogen purification from residuals like carbon, ash, carbon dioxide CO_2, water H_2O, methane CH_4, hydrogen cynaide HCN, hydrogen chloride HCl, hydrogen sulfide H_2S, carbonyl sulfide COS [12].
The generated syngas can be used to generate electricity or to retrieve hydrogen for different purposes [12].

1.1.2.3 Hydrogen production from biomass

“Biomass and biomass-derived fuels are renewable energy sources that can be used to produce hydrogen in a sustainable way” [12]. The CO_2 released in the atmosphere when a biomass is gasified — to produce hydrogen — has been previously absorbed from the atmosphere and fixed in the growing plants — biomass — by photosynthesis. Biomass can be classified in energy crops, agricultural or forest waste and residues, industrial and municipal waste. The different processes used to obtain hydrogen from biomass can be divided into thermochemical, biological — fermentation — or photobiological [12]:

- **Thermochemical processes**: these are combustion, liquefaction, gasification and pyrolysis. For what concerns gasification, the Subsubsection 1.1.2.2 contains all the details. Pyrolysis, instead, involves the heating of

the biomass at 370-550 °C in a pressurized enviroment — 0.1-0.5 MPa — in absence of air, in order to not burn the biomass and make possible its conversion into liquid oils, solid charcoal and gaseous compounds.
It is also interesting to cite the microwave-assisted hydrogen production: it exploits microwave energy as a different source of heat than conduction, convection or radiation for pyrolysis process [22]. "Compared to conventional pyrolysis, microwave-assisted pyrolysis usually produces more H_2 and CO" [22].

- **Biological fermentation**: this process take place in presence of hydrogen-producing enzymes, like nitrogenase, Fe hydrogenase and NiFe hydrogenase; or in presence of microorganisms, cyanobacteria, purple bacteria and microalgae. These different fermentation proccesses require bioreactors based on dark anaerobic hydrogen production, and can be divided mainly in 3 types: "water gas shift" bioreactors incorporating purple bacteria, anaerobic fermentation bioreactors incorporating chemotrophic bacteria, bioreactors with immobilized enzymes.
- **Photobiological processes**: this hydrogen production method is based on photosynthesis in bacteria and green algae, and nowadays the production is limited by low energy conversion efficiencies. The photobioreactor can be of 3 typologies: photobioreactor incorporating cyanobacteria, photobioreactor incorporating green algae, photobioreactor incorporating purple bacteria.

The biological processes for hydrogen production from biomass are at an early stage of development and requires more studies in order to improve the hydrogen yield [12].

1.1.2.4 Water splitting

The water splitting reaction is the chemical reaction that makes possible to obtain the molecular hydrogen starting from water:

$$H_2O_{(l)} \rightarrow H_{2(g)} + \frac{1}{2}O_{2(g)} \tag{1.5}$$

Reaction 1.5 illustrates that water can be dissociated into its elemental components: in standard condition of temperature and pressure — T = 298 K and P = 1 bar — water is in liquid state while the products — molecular hydrogen and oxygen — are in gaseous form. Equations 1.6, 1.7 and 1.8 show enthalpy, entropy and Gibbs free energy related to Reaction 1.5 in standard test condition:

$$\Delta H_d^0(H_2O_{(l)}) = +285.840 \;\; kJmol^{-1} \tag{1.6}$$

$$\Delta S_d^0(H_2O_{(l)}) = +163.15 \;\; Jmol^{-1}K^{-1} \tag{1.7}$$

$$\Delta G_d^0(H_2O_{(l)}) = \Delta H_d^0(H_2O_{(l)}) - T \cdot \Delta S_d^0(H_2O_{(l)}) = +237.22 \;\; kJmol^{-1} \tag{1.8}$$

Since Reaction 1.5 is strongly endothermic, as suggested by Equation 1.6 that highlight a highly positive enthaply variation, the Gibbs free energy is highly positive too — the negative entropic contribution is not enough to invert the sign of equation 1.8 —, and as a consequence, the water splitting chemical reaction is strongly non-spontaneous.
Analyzing Reaction 1.5 for temperature conditions different from the standard one, it is possible to assert, as proven by Figure 1.2, that the total energy required to split 1 mole of water is almost constant, the entropy change is also constant but as a consequence $T\Delta S$ is growing with temperature, and the Gibbs free energy decreases with temperature, even though becomes negative only for temperatures higher than $2500\,K$.

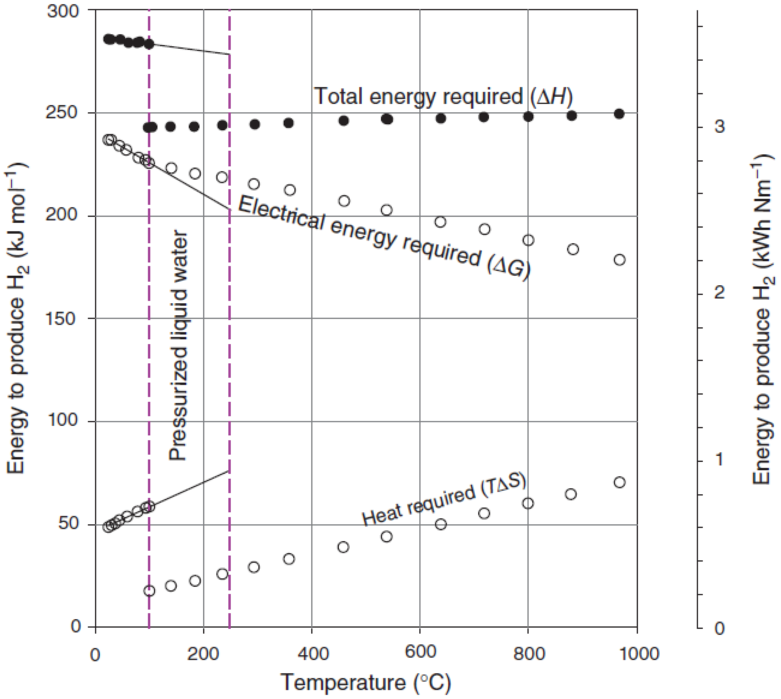

Figure 1.2: $\Delta G(T)$, $\Delta H(T)$, $T\Delta S(T)$ of the water splitting reaction at P = 1 bar [13]

In Figure 1.2 it is also possible to notice a discontinuity for both enthalpy and entropy variation at $T = 100°C$, that brings in a slope change of Gibbs free energy variation, due to the difference that exist in the reaction when the reagent water is not in liquid state but in vapour state [13]:

$$H_2O_{(vap)} \rightarrow H_{2(g)} + \frac{1}{2}O_{2(g)} \tag{1.9}$$

$$\Delta H_d^0(H_2O_{(vap)}) = +241.80 \ \ kJmol^{-1} \tag{1.10}$$

$$\Delta S_d^0(H_2O_{(vap)}) = +44.10 \ \ Jmol^{-1}K^{-1} \tag{1.11}$$

$$\Delta G_d^0(H_2O_{(vap)}) = +228.66 \ \ kJmol^{-1} \tag{1.12}$$

There exist different technologies that exploit water splitting to produce hydrogen, and the principal distinction is related to the source of energy used to reach the conditions required by Reaction 1.5. The most relevant of these technologies are:

- **Electrolysis**: this technology drives the water splitting using electricity, with a device called electrolyzer. This kind of transformation is called endoergonic.
  One electrolyzer is composed by multiple electrolysis cells, and each cell is made of two electronic conductor — electrodes — and an ionic conductor placed between the two electrodes — electrolyte —.
  Cells that drive water electrolysis work thanks to the electricity provided that is used to split water molecules into gaseous hydrogen and oxygen. Depending on the electrolyte pH, it is possible to have an acidic or an alkaline media, and the water splitting occurs with half-cell reactions and associated mechanisms — charges and ions transportation — illustrated in Reactions 1.13 and 1.14 — acidic media — and in Reactions 1.16 and 1.17 — alkaline media —:

$$anode \ \ (acidic \ \ media): \ \ H_2O_{(l)} \rightarrow \frac{1}{2}O_{2(g)} + 2H^+ + 2e^- \tag{1.13}$$

$$cathode \ \ (acidic \ \ media): \ \ 2H^+ + 2e^- \rightarrow H_{2(g)} \tag{1.14}$$

$$full \ \ reaction \ \ (acidic \ \ media): \ \ H_2O_{(l)} \rightarrow H_{2(g)} + \frac{1}{2}O_{2(g)} \tag{1.15}$$

$$anode \ \ (alkaline \ \ media): \ \ 2OH^- \rightarrow H_2O + \frac{1}{2}O_{2(g)} + 2e^- \tag{1.16}$$

$$cathode \ \ (alkaline \ \ media): \ \ 2H_2O + 2e^- \rightarrow H_{2(g)} + 2OH^- \tag{1.17}$$

$$full \ \ reaction \ \ (alkaline \ \ media): \ \ H_2O_{(l)} \rightarrow H_{2(g)} + \frac{1}{2}O_{2(g)} \tag{1.18}$$

  Reactions 1.13 and 1.16 show the oxygen evolution reaction (OER) for an acid electrolyte and an alkaline electrolyte respectively, while Reactions 1.14 and 1.17 shows the hydrogen evolution reaction (HER) again for acid and alkaline electrolyte respectively.
  In general the full reaction mechanism involves the migration of an electron toward the electric conductor and the migration of an ion toward the electrolyte (ionic conductor). The mechanism is a bit different depending

on the electrolyte media.
The electrolyzer essentially works similarly to a battery in charging condition, where the external electricity source generates a difference of potential between the two electrodes, making possible the whole migration phenomena. The main distinction between an electrolyzer and a battery is due to the electrolyzer nature: it is in fact an open system and not a closed system, and the reagents are externally provided while the products should be evacuated to permit a continuous flow of the substances [13].

- **Thermochemical cycles**: the direct thermal dissociation of water — thermolysis — is theoretically the simplest reaction to produce hydrogen, but the problem is that the complete dissociation takes place only at $4500\,K$ (even though reasonable conversion yield occurs just from $2500\,K$) and the heat provision is very challenging from both technical and economical point of view.
  To overcome this issue and reduce the temperature necessary for the thermolysis reaction, the thermochemical cycles have been developed: these cycles offer very high conversion efficiencies for large-scale production of hydrogen, therefore, since the oil crises of the 1970s, nuclear and solar heated thermochemical cycles have been studied. Furthermore these kind of processes also avoid the problem of hydrogen and oxygen separation [15].
  "Thermochemical cycles decompose water into hydrogen and oxygen via a series of chemical reactions at least one of which is highly endothermic" [15]. Heat can be provided by discarded heat from nuclear very high temperature reactors (VHTRs) or solar concentrated plants (CSP). Sulfur-based chemical cycles were originally developed for VHTRs discarded heat, but since these kind of nuclear plants are available only as research installation or very few power generation plants still under construction, it seems more appropriate the use of concentrated solar energy: this last technology consists in heliostats that concentrate sunlight onto a concentrated receiver system located on the top of a tower. Even though this technology is still under development, it is very promising for "green" hydrogen production.
  The most investigated cycles are the one based on metal oxides and on sulfuric acid, but other interesting alternatives focus on complex candidate like the UT-3 cycle — Ca/Fe/Br cycle, proposed by the University of Tokyo (UT) in 1978 —, the hybrid copper chlorine cycle and the uranium-europium cycle (better suited for nuclear waste heat).
  The main drawbacks of this technology are related to thermal losses and the irreversible formation of by-products. However, it offers significant advantages, such as more efficient use of solar energy compared to converting it into electricity and lower land requirements. This leads to reduced production costs and the potential for cogenerating both electricity and hydrogen, making thermochemical cycles a promising solution for energy

storage [15].

- **Photochemical processes**: this type of technology is based on the photoelectrochemical cell (PEC cell), where oxidation and reduction half-reactions take place in locally separated electrodes. The main complications of these devices are related to the choice and design of an efficient photocatalyst, that should be cheap, easy to produce, non toxic and should be made by not rare chemical elements [12]. More detail on this technology are treated in Subsection 2.2.1.
- **Sonolysis**: this technique involves the usage of ultrasound chemistry in the water media to induce sonochemical reactions that occur because of multi-bubble cavitation: the sonochemical reactions can be exploited to produce hydrogen both by their own or as a synergic phenomenon with photochemical processes — sono-photolysis, treated in Subsection 2.2.2 —, electrochemical processes — sonoelectrochemistry — or others [22]. This whole phenomenon is analyzed in detail in Section 2.1.

1.2 Current energetic context and hydrogen role in Europe

1.2.1 Current energetic context in Europe and Italy

The energy available in the European Union (EU) comes from the one produced and the one imported from other countries: to get a good overview of the actual energy mix, it is important to count both these contributions.

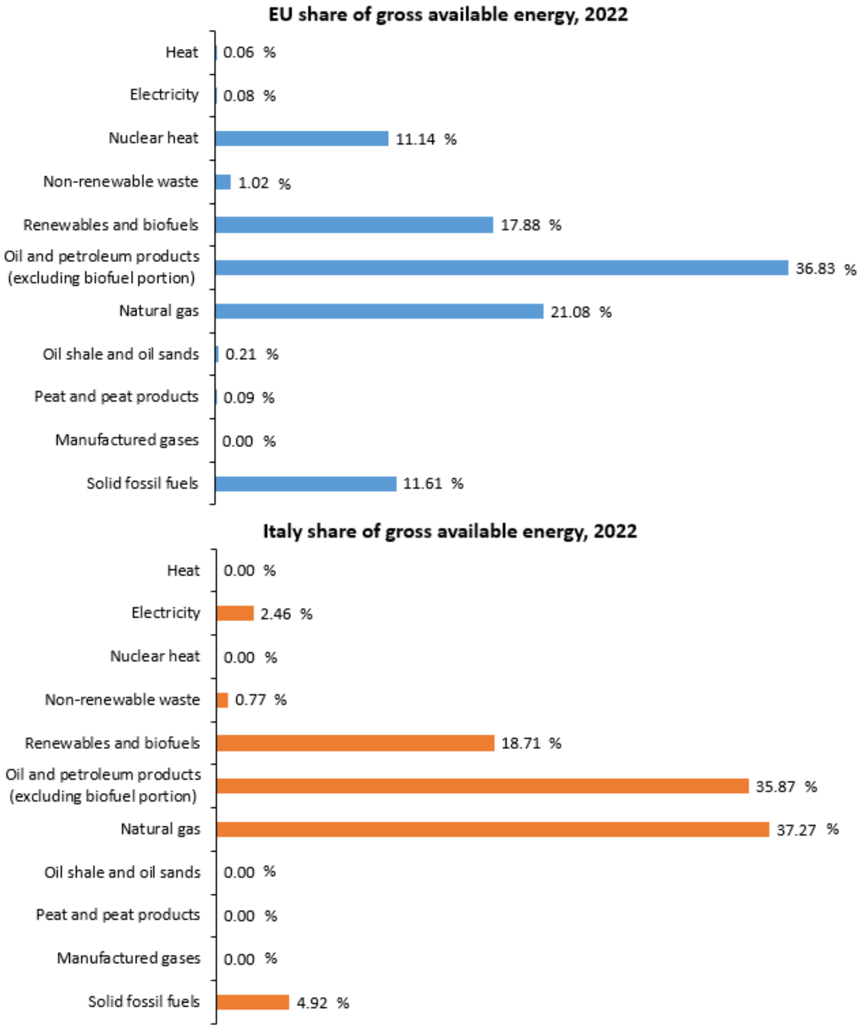

Figure 1.3: Gross available energy by sources, in European Union and in Italy, in 2022 [4].

Figure 1.3 highlights the shares of the different energy sources available in EU in 2022, with a focus on the situation in Italy.
The energy mix was mainly composed of crude oil and petroleum products, natural gas, renewable energy sources, solid fossil fuels and nuclear energy (true for EU but not for Italy) [4]. The proportion of these sources changed from country to country, but in average in the European countries the oil products were preferred, followed by natural gas, renewables, solid fossil fuels and nuclear sources, with the latter two that share similar values of gross available energy.
Focusing on the Italian energy sources, natural gas was the most available, while the other sources shared the same preferences with every European average country, apart from nuclear energy, that was completely non-available.

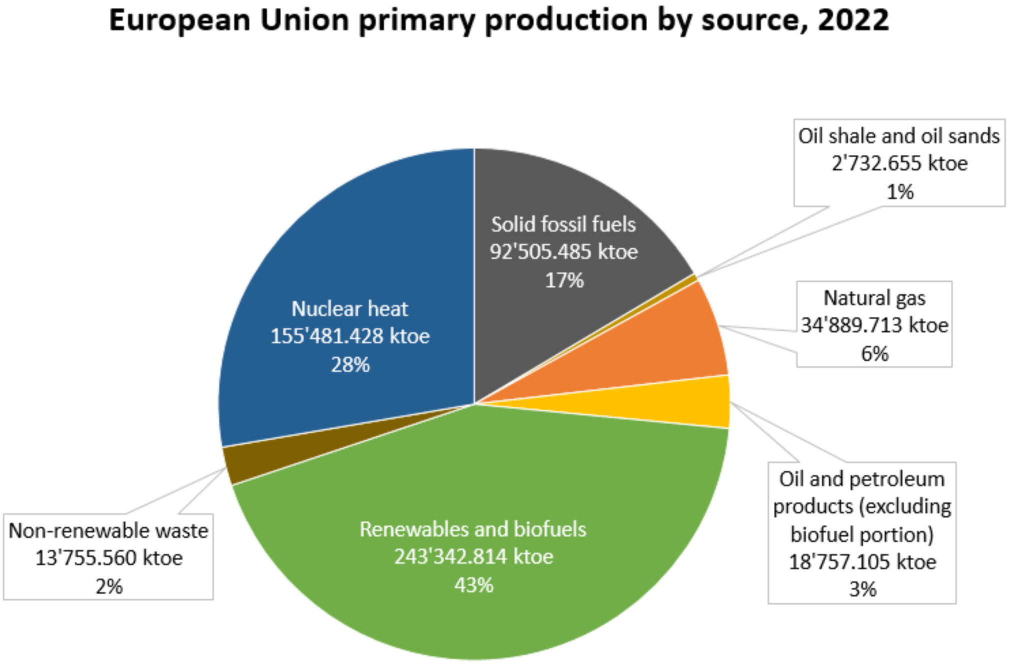

Figure 1.4: Primary production by sources, in European Union, in 2022 [4].

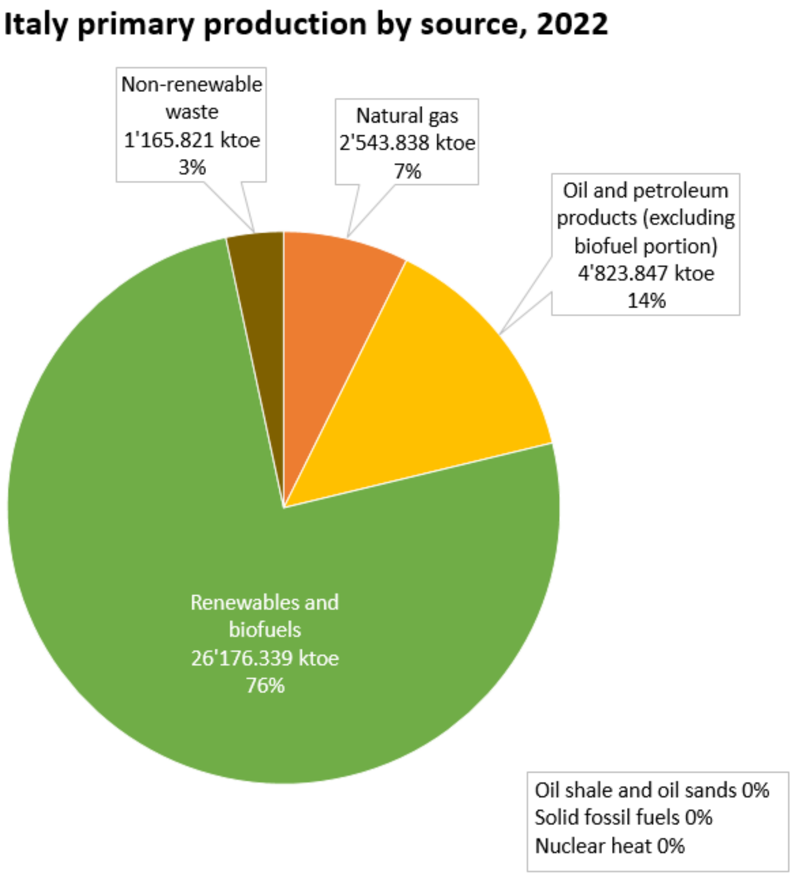

Figure 1.5: Primary production by sources, in Italy, in 2022 [4].

Figure 1.4 and Figure 1.5 instead show the energy primary production means in EU and in Italy in 2022: as primary production of energy is intended the extraction of energy in a usable form from natural sources. In the European Union the major methods of primary production of energy were the renewables and biofuels — 43% —, nuclear — 28% —, solid fossil fuels — 17% —, natural gas — 6% — and oil and petroleum products — 3% — [4].
Anyway the situation in Italy was quite different, and it is normal since the production of energy was different in each European country [4]: the main production means were renewable and biofuels, according to EU, but the share was of 76%. Since no nuclear heat was present in Italy, the following primary energy production means were crude oil — 14% — and natural gas — 7% —.

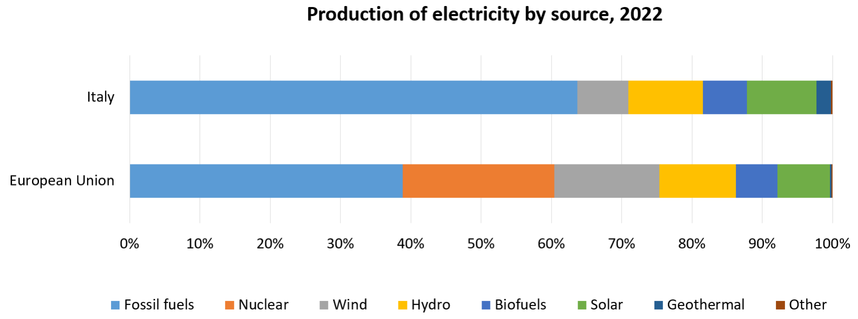

Figure 1.6: Electricity production by sources, in European Union and in Italy, in 2022 [4].

Figure 1.6 illustrates the sources from which came the electricity in Europe, that is the 23% of the final energy consumed by the end-user, and in Italy [4], in 2022. It is eye catching that in the European Union electricity was produced mainly by fossil fuels and nuclear energy sources — with a share of 61% — , with 39% of fuels and 22% of nuclear; the remaining percentage belonged to renewable sources, divided between wind turbines — 14% —, hydropower plants — 10% —, solar power — both CSP and photovoltaics, 8% — and biofuels — 5% — [4].
Sources for electricity production in Italy were a bit different from the EU average, since the fossil fuel source alone contributed for almost 63%. Also the renewables share was quite diverging, with a reduced presence of wind turbines — 8% — that was mostly substituted by a better exploit of solar energy — near 9% — and geothermal sources — 3% —.

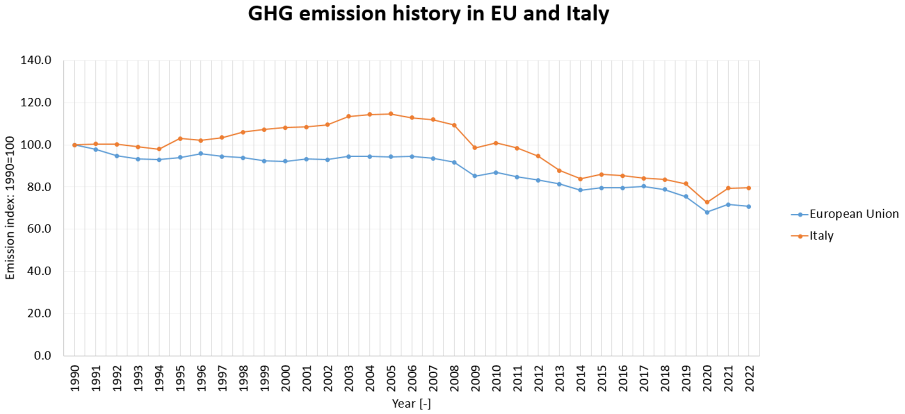

Figure 1.7: Green house gas emission history in European Union and in Italy [4].

The scientific community agrees that the greenhouse gas (GHG) emissions made by man activity on Earth are the principal cause of the increase of the average temperature: primarily these pollutant emissions come from the burning of fuels in power plants, cars or homes, but also farming and waste decaying are sources of GHG emissions [4].
From Figure 1.7, the historical trend of GHG pollutant emissions in the atmosphere by the European Union have declined since 1990 (year taken as a reference for the emission index) by 28%, but much more has to be done in order to reach the targets agreed by the European Commission, that requires a reduction of 55% until 2030 and a 100% reduction in 2050, that is the net zero emission (NZE) objective [4].
In Italy the historical trend follows a similar path with respect to the European average country, even though it is noticeable a higher GHG emission contribute in the historical period that starts in 1996 and ends in 2014: starting from that year, the emission levels have begun to be quite similar to those of the EU. It is also interesting to notice the reduction occurred in 2020 due to the COVID-19 emergency: the reduction of human activity during that year caused an important decrease in the GHG emissions, confirming what is the principal cause of pollution in the atmosphere.

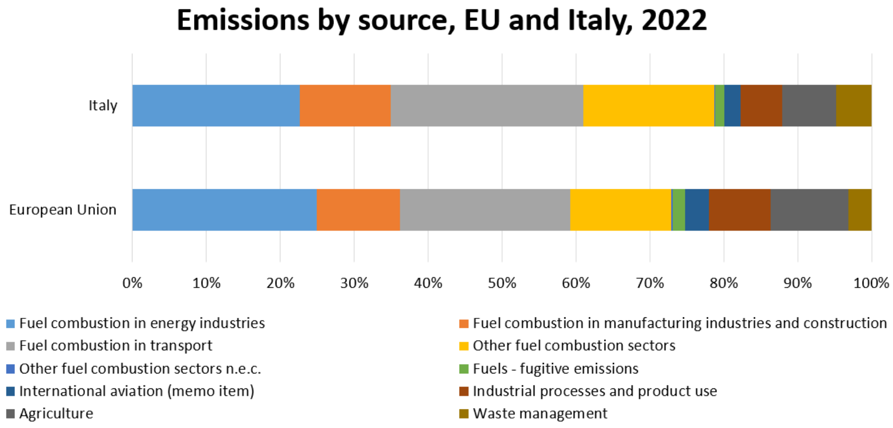

Figure 1.8: Emission by source in European Union and in Italy in 2022[4].

Figure 1.8 shows the details of the emission sources in 2022: they mainly came from fuel combustion as stated before — near 73% in EU and almost 78% in Italy —, and in particular the energy production sector, industry sector and the transport sector by their own contributed to near 60% of the total pollutant emissions in both Europe and Italy.

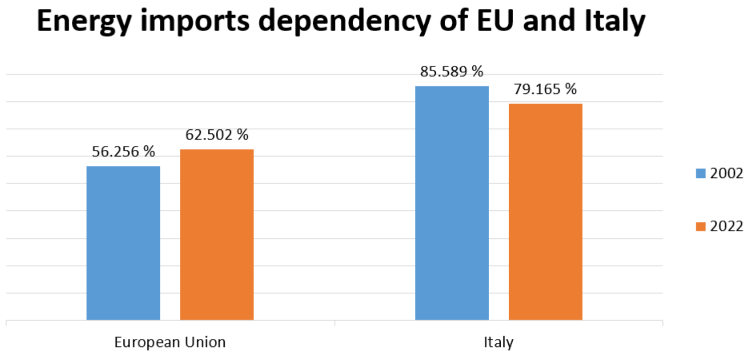

Figure 1.9: Energy imports dependence of European Union and Italy: comparison between 2002 and 2022 [4].

"In 2022, the EU produced around 37% of its own energy, while 63% was imported" [4]. This result is shown in Figure 1.9, where the energy import dependency rates of EU and Italy in 2022 are compared with levels in 2002: energy import dependency rate is defined as the proportion of energy that an economy must import to meet its energy needs, and is measured as the share of net imports — imports minus exports — in gross inland energy consumption — that is the sum of energy produced and net imports — [4].

The main imported product category was oil and petroleum products, followed by natural gas and solid fossil fuels: in particular in 2022 half of the oil products were imported from Russia — 21% —, United States — 11% —, Norway — 10% —, Saudi Arabia — 7% — and United Kingdom — 7% —; half of the natural gas imports came from Russia — 23% —, Norway — 17% —, United States — 14% — and Algeria — 11% —; while solid fossil fuel biggest share of imports arrived from Russia — 23% —, United States — 18% —, Australia — 16% —, South Africa — 14% — and Colombia — 13% —. Anyway, the situation is subject to an important change, due to the current geopolitical context, in particular the sanctions imposed by the European Union to Russia as a consequence of aggression against Ukraine in 2022 [4].

1.2.2 Importance of hydrogen development

As it as been discussed in Subsection 1.1.1, hydrogen has a great potentiality for future decarbonisation scenarios, thanks to its characteristic and many functionalities.

The reasons for which clean hydrogen is being pursued at political level depend on many policy drivers, namely factors that shape and influence the development and implementation of polices [14]: "in the context of a clean hydrogen strategy, selecting drivers that motivate the development of a hydrogen sector in the country can lead to a better framing for the future of the sector" [14].

This implicit process establishes the trajectory of the hydrogen industry and the country's role within it, thus the evaluation of the most relevant policy drivers is essential, considering the country's unique circumstances. The most common drivers for clean hydrogen are: reaching the decarbonisation goals, accelerating innovative industrial development, diversifying energy exports, increasing energy security, supporting long term renewable energy storage, improving air quality in cities, ensuring alignment with other strategic energy initiatives, responding to international market dynamics, enhancing food security [14]. "Each driver reflects the multi-faceted role that hydrogen is expected to play in addressing some of the most pressing global challenges" [14], and in particular the combination of key drivers can underscore a possible national strategy: in fact, referring to the geo-political and energetic context of the European Union and Italy, treated in Subsection 1.2.1, it comes out that their main political drivers for clean hydrogen development strategy are the reaching of decarbonisation goals — Subsubsection 1.2.2.1 — and increasing energy security — Subsubsection 1.2.2.2 —, but also the acceleration toward innovative industry sector as a consequence — Subsubsection 1.2.2.3 — and the support to long term storage of volatile renewable energy sources (VRES) — Subsubsection 1.2.2.4 —.

1.2.2.1 Reaching decarbonisation goals

The global climate crisis has put an accent to the pressing need to restrain the rising temperature, reducing or entirely eliminating emissions from all the economic activities, included the one related to the energy sector, as it has been analyzed in Subsection 1.2.1 for what concerns the European and Italian situation. In the 1.5°C scenario, direct electrification only is projected to achieve the 51% of share in total final energy consumption, leaving the remaining fraction to other means, that includes for sure biomass, hydrocarbons technologies equipped with carbon capture and storage (CCS), and of course clean hydrogen and all its derivatives [14].

Focusing in particular on clean hydrogen and derivatives, these have the great potentiality of decarbonising the "hard-to-abate" sectors, like industry or transports, which posses substantial technical and socio-economic hurdles: clean hydrogen and derivatives can play a fundamental role in the production of chemicals and fuels or can be directly used as a clean energy source, in order to achieve decarbonisation objectives [14].

The reason that can encourage the development of a national — and European — hydrogen strategy is the net-zero commitment [14].

1.2.2.2 Increasing energy security

Energy security, defined as the uninterrupted energy supply at affordable prices, is a critical point for all the energy importing countries, like EU and Italy — further details in Subsection 1.2.1 —. Energy security is a driver for developing the green hydrogen sector because it can promote the self-production of green hydrogen as a feedstock for a local industry, avoiding the price fluctuations of goods tied with fossil fuel prices. An example is the production of fertilizer,

that requires hydrogen feedstock: if it is produced by conventional natural gas reforming, the fertilizer price will be linked to the price of natural gas [14].
Another reason for energy security to be a driver is the diversification of supplier: clean hydrogen can be produced virtually everywhere, and so its trade flows are less prone to be subject of geopolitical influences, like for oil and natural gas [14].

1.2.2.3 Acceleration toward innovative industry sector

The development of an hydrogen economy is nowadays in the early stages, and it is required a massive scaling-up of all its related technologies: this bring a significant opportunity for the economic growth through building a local "industrial ecosystem". This economic opportunity is an important policy driver toward clean hydrogen development, and in particular it relies on the transition of the hard-to-abate industries from high-carbon to low-carbon processes — that also helps in the decarbonisation process —, since, looking forward to markets where the carbon footprint carries a price in the final good, it has a relevant impact [14].
Another economic opportunity is the creation of an upstream technology industry that supports the hydrogen economy, that is the production of all the equipment required to make possible an hydrogen infrastructure from production to end-use [14].

1.2.2.4 Support to long term storage of VRES

"As the power sector decarbonises, the share of VRE will have to grow to levels where over-generation becomes structural, and curtailment risk will increase substantially. There may be seasons when VRE generation exceeds demand even with the assistance of short-term storage solutions (e.g. pumped storage hydropower or lithium-ion batteries) and demand-side management" [14].
"Underground hydrogen storage is foreseen to provide an opportunity for long-duration, large-scale energy storage. This allows green hydrogen to be produced and stored underground and then used seasonally, for example during periods when renewable power production cannot cover the demand" [14].

1.2.3 Hydrogen initiatives in EU

"In 2022, hydrogen accounted for less than 2% of Europe's energy consumption and was primarily used to produce chemical products, such as plastics and fertilisers. 96% of this hydrogen was produced with natural gas, resulting in significant amounts of CO2 emissions. The priority for the EU is to develop renewable hydrogen and it aims to produce 10 million tonnes and import 10 million tonnes by 2030" [5].

1.2.3.1 Strategy

The strategy adopted in 2020 by EU for hydrogen (COM/2020/301) is composed of 5 points:

- Investment support;
- Production and demand support;
- Hydrogen market and infrastructure creation;
- Research and international cooperation.

Furthermore, hydrogen has an important role in the EU strategy for energy system integration (COM/2020/299) [5].

1.2.3.2 Legislative proposals

The ‘Fit-for-55’ package — 2021 — advances some legislative proposals to the European hydrogen strategy into a concrete policy framework, including both proposals to set targets for the uptake of renewable hydrogen by 2030 in the ‘Renewable Energy Directive’ and the ‘Hydrogen and decarbonised gas market package’ to support the creation of an hydrogen infrastructure and market; proposals that came into force in 2023 and 2024 respectively. This hydrogen policy framework was complemented with two delegated acts adopted in June 2023 and applicable to renewable hydrogen under the Renewable Energy Directive: the first delegated act covers the renewable fuels of non-biological origin (RFNBOs) and sets product criteria for ‘renewable hydrogen’, the second delegated act instead defines a scheme to calculate the life-cycle emissions of renewable hydrogen and recycled carbon fuels [5].

1.2.3.3 Investments

The “Recovery and Resiliency Facility for clean energy” was a temporary instrument for EU countries in 2021 to invest in hydrogen projects.
Investment support has been provided by the “Important Projects of Common European Interest” (IPCEIs) on hydrogen [5]:

- ‘IPCEI Hy2Tech’: approved in July 2022, included 41 projects aimed at developing innovative hydrogen technologies for the decarbonisation of industrial processes and mobility sector, focusing on the end-users;
- ‘IPCEI Hy2Use’: approved by the European Commision in September 2022 as a complement of the previous ’IPCEI Hy2Tech’, aimed at the development of the hydrogen related infrastructure and sustainable technologies for hydrogen integration in the industrial sector;
- ‘IPCEI Hy2Infra’: approved in February 2024, supports the development of electrolyzers, hydrogen distribution pipelines and transmission, large-scale hydrogen storage facilities and handling terminals;

- ‘IPCEI Hy2Move’: approved in May 2024, it covers a wide part of the hydrogen technology value chain promoting innovations.

1.2.3.4 Accelerator

After the publication of REPowerEU in May 2022, the Commision complements the EU hydrogen strategy to increase the ambition for the renewable hydrogen as an energy carrier to move away from Russia’s fossil fuel imports. The Staff Working Document (SWD/2022/230) accompanying the plan, underline the concept of ‘hydrogen accelerator’, to scale up the deployment of renewable hydrogen, which will contribute in accelerating energy transition in EU [5].

1.2.3.5 Initiatives

“The Clean Hydrogen Partnership (2021-2027) is a joint public-private partnership supported by the Commission through Horizon Europe. [...] On 1 March 2023, the Commission and key stakeholders signed a joint declaration on renewable hydrogen research and innovation, committing to step up and accelerate joint action in research, development, demonstration and deployment of Hydrogen Valleys” [5].

“The European Clean Hydrogen Alliance was launched alongside the EU hydrogen strategy in 2020 as part of the new industrial strategy for the EU. It brings together industry, national and local authorities, civil society and other stakeholders. The alliance’s objective is to achieve an ambitious deployment of hydrogen technologies by 2030 by bringing together renewable and low-carbon hydrogen production, demand in industry, transport and other sectors, and hydrogen transmission and distribution. It launched 6 thematic roundtables in key areas of hydrogen production, transportation and use and published a hydrogen project pipeline in November 2021. It also hosts the ‘Electrolyser Partnership’ to bring together electrolyser manufacturers and suppliers of components and materials to achieve a combined annual electrolyser manufacturing capacity of 17.5 GW by 2025 in Europe” [5]. “The Hydrogen Public Funding Compass is an online guide for stakeholders to identify public funding sources for hydrogen projects and it provides information on all the EU programmes and funds (2021-2027) that are relevant for the sector” [5].

Chapter 2

Sonolysis, Photolysis and Sono-Photolysis state of the art

2.1 Sonolysis

2.1.1 Power Ultrasound

‘Ultrasounds’ are the acoustic waves with a frequency that overcomes the human hearing maximum frequency range, and it is considered approximately above 20 kHz, since every person has a different hearing range. Normally, there is a distinction between ‘low power ultrasounds’ and ‘power ultrasounds’, where the former is characterized by a frequency above 1 MHz and power lower than 10 W, the latter instead develops for frequencies between 20 kHz and 100 kHz — ‘low frequency’ ultrasounds — and with power of few tens of watts, therefore making possible the alteration of the medium where the ultrasounds are propagating through [8] [22]. The intermediate range of frequencies — 100 kHz - 1 MHz — is the ‘high frequency ultrasounds’ range but is less used [8]. Figure 2.1 shows the just described ranges of frequency-power used in the US (ultrasounds) field.

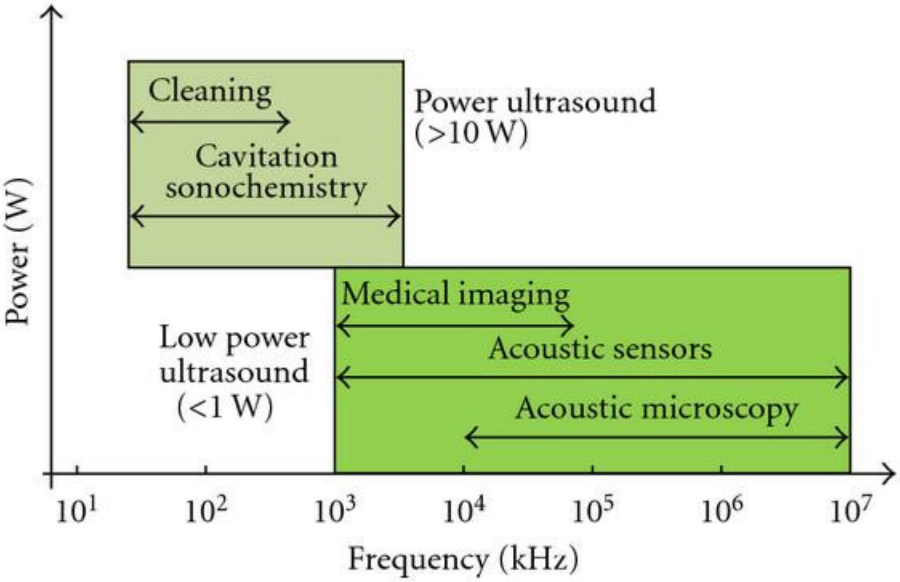

Figure 2.1: Utilization of ultrasounds according to power and frequency [8].

Power ultrasounds can be transmitted directly, with mechanical transmission of vibrations from the US transducer into a solid surface, or indirectly into a fluid, where several effects may be induced, as the heating due to the dissipation of mechanical energy — phenomenon used for "the determination of the ultrasonic energy supplied to the medium in an ultrasonic reactor, well-known as the calorimetric method" [8] —, nebulization and acoustic fountain — that occurs for high frequency US in the liquid-gas interface, reaching temperature up to 250 °C —, but mostly acoustic streaming and acoustic cavitation: acoustic streaming arises from dissipation of acoustic energy that manifest as a gradient in momentum and so the creation of a fluid stream, with an increase of the convection heat transfer coefficient mostly in the liquid-solid interfaces because of turbulence; acoustic cavitation instead consists in the formation, growth, oscillation and collapse of many tiny gas bubbles [22] [8]. Figure 2.2 and Figure 2.3 represent a scheme of these phenomena.

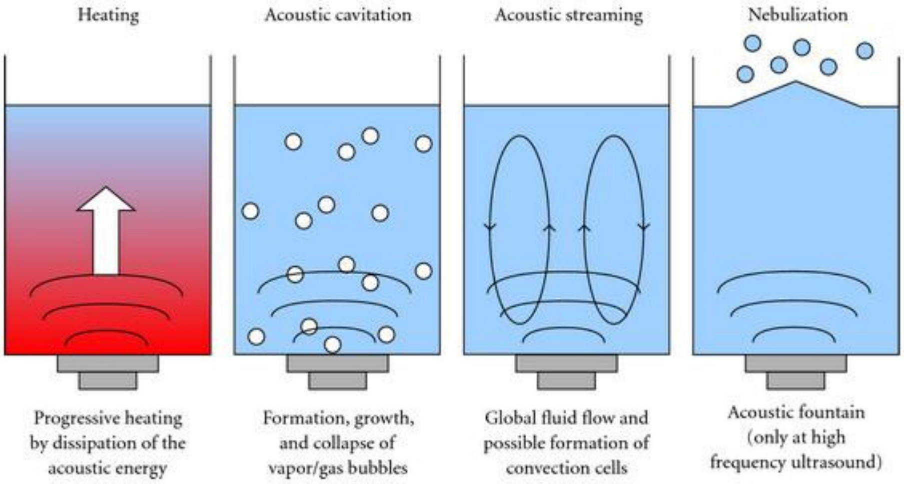

Figure 2.2: Effects resulting from propagation of ultrasounds in liquids scheme [8].

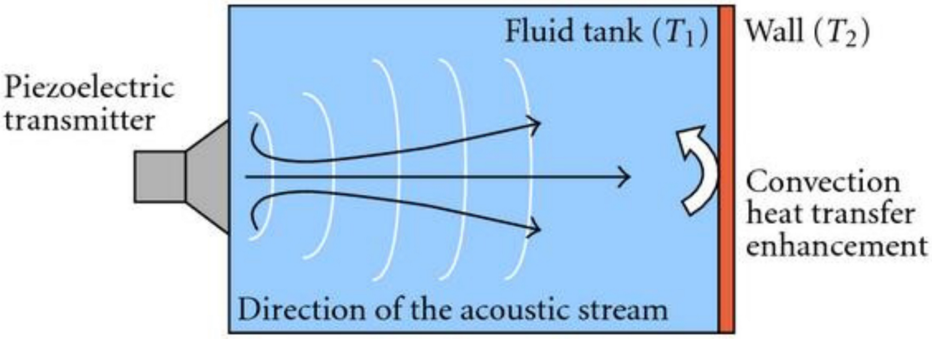

Figure 2.3: Acoustic streaming scheme [8].

Since the ultrasounds wave is a pressure wave, whenever the local pressure decreases sufficiently below the vapour pressure during the rarefaction phase, the static pressure and the cohesive forces are overcome and gas bubbles are formed, creating locally a so-called ‘weak point’: in these points, the gas bubbles — that can contain also dissolved gasses — expand whenever the local pressure outside the bubble is lower — rarefaction phase — and violently collapse when the local pressure outside the bubble becomes higher — compression phase —. This whole process of bubbles formation and collapse is named ‘acoustic cavitation’ and occurs within many different cycles of compression-rarefaction

phases of local pressure [8] [22].
The acoustic cavitation phenomenon is really important in the 'sonochemistry' field, as explained in Subsection 2.1.2, since in aqueous media each cavitation bubble acts as a local hotspot with temperatures near 5000 °C and pressures of 2000 atms, and each collapse imparts important chemical and mechanical effects: mechanical because of the massive shear force exerted by the shock wave of the bubble collapse, and chemical because of the high pressure and temperature reached locally at the bubble collapse, that can be considered as high temperature micro-reactors [22].

2.1.2 Sonolysis general principle: the role of acoustic cavitation

Thanks to the study on acoustic cavitation induced by power ultrasounds in a liquid, in the late 1970's a new field of chemistry has received attention: acoustic cavitation in fact causes the 'Sonoluminescence' and the 'Sonochemistry'. Sonochemistry takes places under multi-bubble cavitation, since this phenomenon is the most relevant one in a reactor that undergoes US stimulation [22].
Cavitation bubbles normally contain dissolved gas molecules such as N_2 and O_2 and vapor from the solvent — normally water, aqueous solution —, and the extreme temperature and pressure levels reached by bubble collapse brings to the chemical effects cited in Subsection 2.1.1, that manifest with the generation of highly reactive radicals — i.e. an atom, molecule or ion with at least an unpaired electron in the valence band — and other species through endothermic chemical reaction — $OH\cdot$ hydroxyl radical, O_3, H_2O_2 oxygen peroxide, O —. The hydroxyl radical $OH\cdot$ is the most dominant unstable specie and plays the most important role in sonochemical reactions, because O_3 presence is negligible and the O atoms generally react with water H_2O to produce oxygen peroxide H_2O_2, that anyway present an oxidation-reduction potential much lower than $OH\cdot$ — $+1.776\,V$ against $+2.06\,V$ —. Near the bubble wall, the lifetime of hydroxyl radical molecules is about $20\,ns$ with an initial concentration of $5 \times 10^{-3} M$, because of the recombination reaction 2.1 [22]:

$$OH \cdot + OH\cdot \rightarrow H_2O_2 \tag{2.1}$$

Several factors influence the sonochemical reactions — sonolysis — [22]:

- **Frequecy** (f): this is the dominant factor to consider in order to gain the maximum efficiency in sonolysis reactions. Lower values of frequency provide largest mechanical effects and lower chemical ones.

- **Acoustic power** (P_w), or **Intensity** (ψ): acoustic power absorbed by a liquid can be determined with the calorimetric method — $q = mc_p\Delta T$; q is the generated heat in J, m is the solution mass in kg, c_p is the specific heat capacity of the solution, and ΔT is the temperature gradient in K —. Increasing the acoustic power, the radicals $OH\cdot$ production increases, and increases also the number of active bubbles and bubbles size.

- **Type of dissolved gas**: this dependency is mainly connected to the thermal conductivity of the noble gas dissolved in the solution, since a lower atomic weight reflects an higher thermal conductivity, and as a consequence an higher dispersion of heat to the surrounding from the bubble, reducing the maximum temperature of the bubble collapse and so the formation of primary radicals. The type of dissolved gas also influences the reactions chain that can occur inside the bubble.
- **Bulk solution temperature** (T): an increase of bulk solution temperature leads to an increase of both vapor pressure and internal collapsing bubble pressure, that means also a lower maximum bubble collapse temperature and so a lower formation of primary radicals, that furthermore presents also an increase kinetic of the recombination reaction. In general also the gas concentration, the surface tension and other properties may be affected by an increase of bulk solution temperature, affecting indirectly the whole acoustic cavitation phenomena.
- **Type of solvent**: the typology of solvent influences directly the properties of the solution, like vapour pressure and solubility, that are strictly connected to the efficiency of the sonication process.

2.1.2.1 Sonolysis of water for hydrogen production

"The use of ultrasounds in clean hydrogen production could be a promising method if water is used as hydrogen source" [22]. Hydrogen production by water sonolysis evolves from acoustic cavitation, and in particular the rapid collapse of microbubbles that produces local enormous pressure and temperature conditions, leading to the formation of highly reactive species such as $OH\cdot$, $H\cdot$, O, $HO_2\cdot$ and H_2O_2. Hydrogen is the most occurring product in water sonolysis, with a production rate of 10-15 $\mu M/min$ [22].

"The mechanism of hydrogen production through acoustic cavitation is under discussion till date. The major part of the hydrogen is produced in the gas phase of the bubble and diffuses out to the surrounding solution. Some researchers have proposed that hydrogen is produced only at the bubble wall through recombination of hydrogen radicals" [22].

Merouani et al. [16] undertook a comprehensive numerical study in order to explain the mechanism of sonochemical hydrogen production, performing by computer simulation the kinetics of 25 chemical reactions occurring inside a bubble: it was observed the production of hydrogen as well as O_2, $HO_2\cdot$, O, H_2O_2, $OH\cdot$ and $H\cdot$, with hydrogen as the main product in all the cases. Based upon the simulation results, it was proposed that the main source of hydrogen is the gas phase of the bubbles with Reaction 2.2 [22] [16]:

$$H\cdot + OH\cdot \rightleftharpoons H_2 + O \tag{2.2}$$

"Several factors influence the sonochemical production of hydrogen. These includes ultrasonic frequency, dissolved gas, ultrasonic power and liquid temperature" [22], but also the transducer duty cycle, the ambient pressure within the reactor, the geometry of the reactor and the number of sonotrodes and their position. [10].

1. **Ultrasonic frequency** (f):
   This is probably the dominant factor in induced sonolysis on aqueous media. In sonochemistry generally the used US frequencies are in the range of 20 kHz to ~ 1 MHz.
   Merouani et al. [16] studied the effect of ultrasonic frequency in the range of 20 - 1140 kHz through numerical simulation for hydrogen production inside the mixture air-Ar bubble, with an acoustic intensity of 1 W/cm^2 and a bulk liquid temperature of 20 °C.

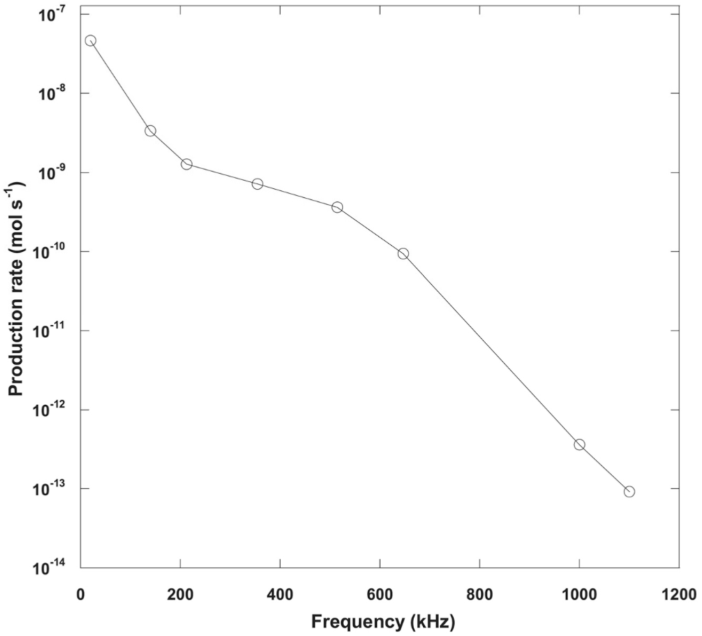

Figure 2.4: Production rate of hydrogen from a single bubble as a function of ultrasonic frequency [16].

The hydrogen production rate decreases with the increase in ultrasonic frequency, as it is shown in Figure 2.4. The reason of this behaviour is related to the influence that frequency has over the maximum bubble temperature, pressure, collapse time and quantity of water vapor trapped at the collapse: smaller frequencies implies more time for the bubbles to expand before collapse, leading to an higher expansion-compression ratio and of course higher temperature and pressure, more favourable conditions for water vapor dissociation into radicals and hydrogen production as a consequence. Even though the number of active bubbles increases with frequencies, the trend shown in Figure 2.4 highlights that the hydrogen yield is more affected by the single bubble events rather than the number of active bubbles, and data confirms this, since at 300 kHz the hydrogen yield is 0.83 $\mu M/min$ while for 1000 kHz is 0.42 - 0.68 $\mu M/min$ [22] [16].

2. **Ultrasonic intensity** (ψ):
   Increasing intensity — applied power — increases also the production of hydrogen, but the effect is more intense at higher frequencies: the study of Merouani et al. [16] simulate also this result, showing how the hydrogen yield trend with increasing frequencies changes also with different US intensity — Figure 2.5 — [22].

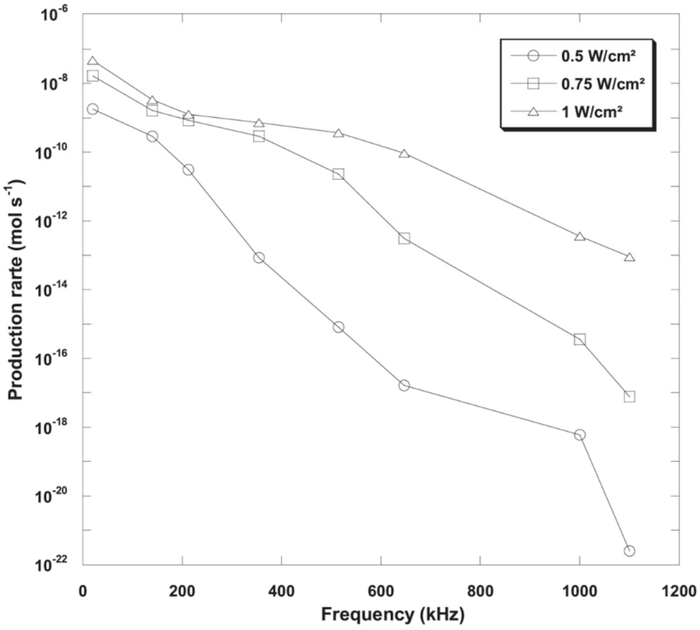

Figure 2.5: Production rate of hydrogen from a single bubble as a function of ultrasonic frequency for various acoustic intensities [16].

Radical production inside the bubble is due to the amount of water vapour trapped inside the bubble, but also the temperature, pressure and collapse time: all of these factors are positively influenced by an higher value of acoustic intensity, since this leads to higher expansion-compression ratio and to an increase of the time required for chemical evolution of water vapour into radicals — and so higher collapse time — [22].

The effect of ultrasonic intensity cannot be determined solely by the yield of a single bubble, it also depends on the number of active bubbles: a more intense US stimulation induces a molecular stretching, and in turn an increment of the volume subjected to cavitation, yielding an enhanced hydrogen production [22].

3. **Dissolved gas**:
   The chemistry of bubbles at collapse is affected by two main parameters related to the dissolved gas: the polytrophic index — $\gamma = c_p/c_v$ —, that should be the highest possible in order to increase the bubble temperature at collapse — monoatomic gasses are favoured —, and the thermal conductivity — λ — that should be the lowest possible in order to reduce the heat dissipation and maintain an high temperature inside the bubble [22].
   Argon has an higher polytrophic ratio and lower thermal conductivity than air — $\gamma_{Ar} = 1.66$ and $\lambda_{Ar} = 0.018 W/m^2K$, while $\gamma_{air} = 1.41$ and $\lambda_{air} = 0.026 W/m^2K$ — and therefore the presence of Ar as dissolved gas helps the hydrogen production increasing the bubble collapse temperature. Merouani et al. [16] have simulated this phenomenon, illustrating — Figure 2.6 — the differences in hydrogen production trend with frequency whenever the water sonolysis contains dissolved air or Ar [22].

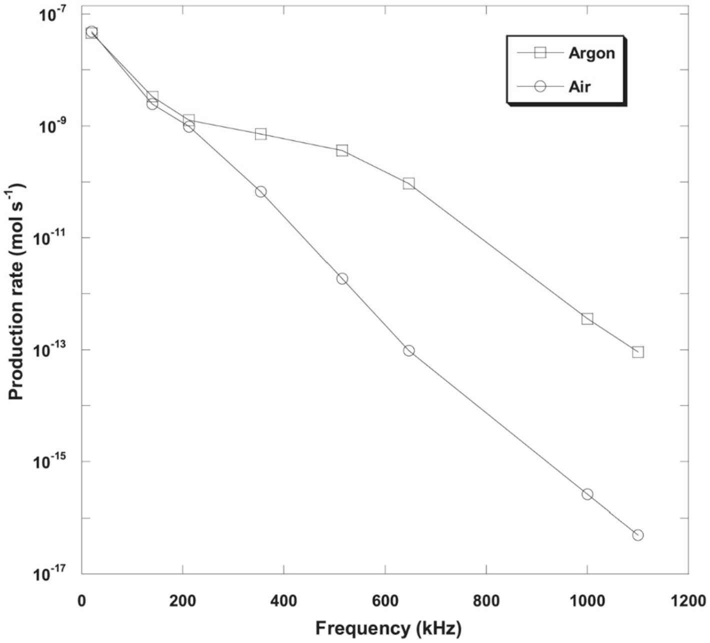

Figure 2.6: Hydrogen production rate from a single bubble as a function of acoustic frequency for different saturating gases [16].

Also the generated quantity of active bubbles is influenced by dissolved gasses and their solubility: higher the solubility and higher the number of active cavitating bubbles. The solubility of Ar in water is bigger than the one of air — $X_{Ar} = 2.746 \times 10^{-5}$ and $X_{air} = 1.524 \times 10^{-5}$ — and so the overall hydrogen yield is incremented by dissolved Ar also because of this reason [22].

Argon atmosphere anyway is not the theoretical best enhancer of cavitation activity: carbon dioxide CO_2 experimentally reports the largest production of bigger bubbles in water due to an higher solubility — $X_{CO_2} = 7.1 \times 10^{-4}$ — and heat capacity — $c_{p,CO_2} = 37.5 kJkg^{-1}mol^{-1}$ —, but its problem is related to the recombination mechanism of the carbon C atom with the set of free radical in the medium, generating species like HCO, $COOH$ or CH_2O [10] [7].

4. **Liquid temperature**:
Another significant effect on hydrogen production by water sonolysis is due to the liquid bulk temperature. Even though the expansion-compression ratio is not affected by liquid temperature, the quantity of trapped water vapour and the temperature inside the bubble are deeply influenced by it, because the liquid-vapour pressure is dependent on this parameter: as a consequence, the formation of free radicals is enhanced by high temperature conditions. Anyway there is a drawback in increasing the liquid temperature, and it is connected to the reduction of the polytrophic index — γ — leading to a lower bubble temperature and less violent collapse, and of course a reduction in radicals formation. Considering these two phenomena together, they give rise to an optimum value of liquid bulk temperature [22].
Merouani et al. [16] with their numerical simulations have confirmed the presence of an optimum temperature.

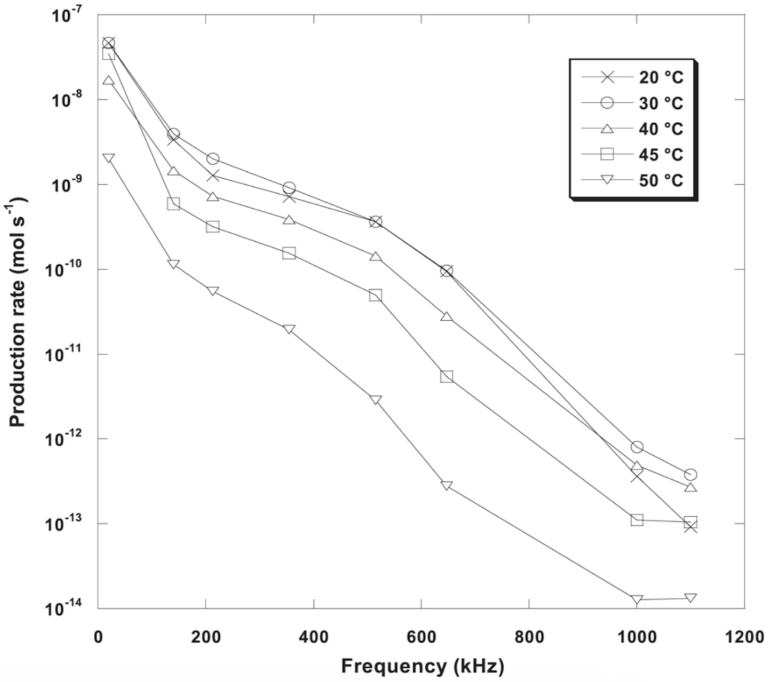

Figure 2.7: Production rate of hydrogen from a single acoustic bubble as a function of acoustic frequency for different bulk liquid temperatures [16].

Figure 2.7 shows that the hydrogen yield trend with frequency is quite the same with different liquid bulk temperatures, but each curve representative of a different temperature highlights different hydrogen yield, and the optimum belongs to the 30 °C liquid temperature curve [22].

5. **Active bubble size**:
Numerical simulation performed by Merouani et al. [17] demonstrated that the active bubble size has an optimum in the context of hydrogen production with sonochemical reactions in aqueous media — simulation conditions are the same as in [16] —. This optimum value increases with acoustic intensity and decreases with frequency and liquid temperature. An increase in bubble size brings also to an increase in trapped water vapour and bubble temperature at collapse, leading to an higher hydrogen yield [22].

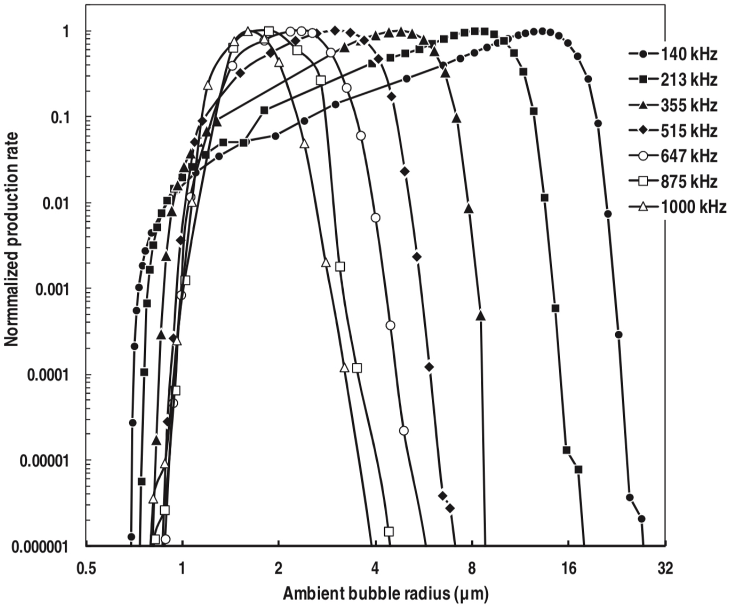

Figure 2.8: Effect of ultrasonic frequency on the size of sonochemically active bubbles for the production of H_2. The production rate values are normalized with respect to the maximum value obtained at each frequency [17].

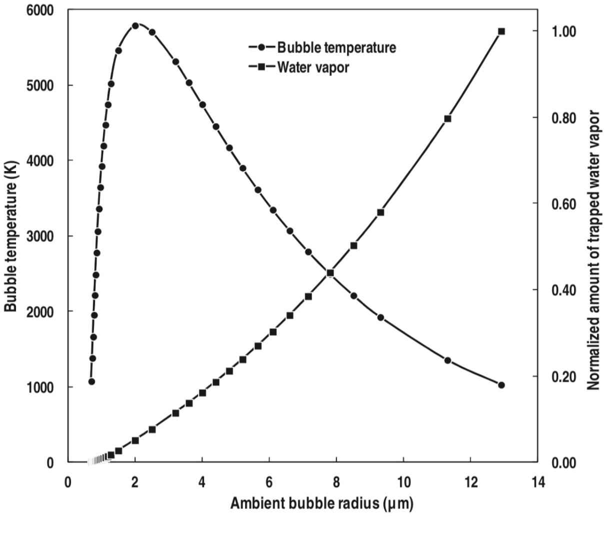

Figure 2.9: Normalized amount of vapor trapped at the collapse and the maximum bubble temperature for various ambient bubble radii at 355 kHz [17].

6. **Transducer duty cycle**:
   This parameter in particular has not been studied in the hydrogen production context, but in sonochemical process in general by Gogate et al. [11]: the comparison between different duty cycle ranges from 20 to 100% in a time period of 50 seconds results with the best sonolysis yield at 60%, while the 100% is not recommended due to maintenance problem of the transducer [10] [11].

7. **Pressure within the reactor**:
   Experimental studies performed by Cotana et al. [24] reported a decrease of hydrogen production with an increase of pressure, justified by the impossibility of cavitation bubbles to freely oscillate, reducing the heat absorption. Furthermore, the bubbles are compressed by the excessive ambient pressure, disadvantaging the bubble evolution towards significant radii [10] [23] [24].

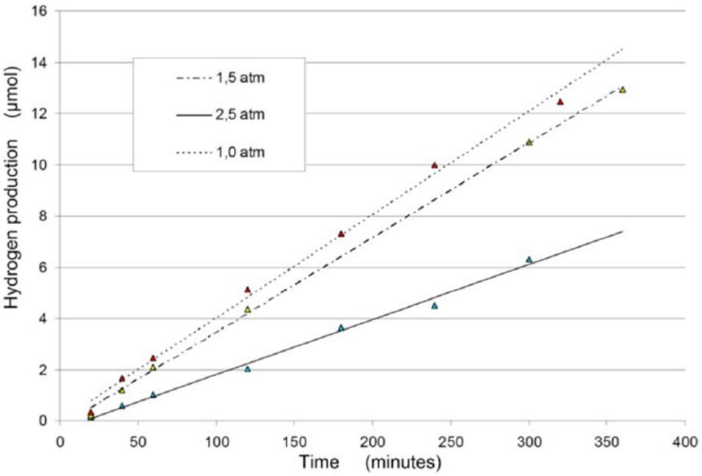

Figure 2.10: Numerical effect on the hydrogen yield from water sonolysis at different pressures within the reactor [24].

8. **Geometry of the reactor & Number and position of sonotrodes**:
   The impact of sonoreactor geometry on the sonochemical process has been extensively studied. Researchers have explored a variety of cylindrical and rectangular reactors through both numerical simulations and experimental methods, focusing on three primary sonoreactor designs, illustrated in Figure 2.11. For a type-A sonoreactor, significant variations in acoustic pressure distribution have been observed, with numerical simulations using COMSOL Multiphysics indicating that a bottom-curved geometry at $20\,kHz$ offers a distinct advantage. Understanding the relationship

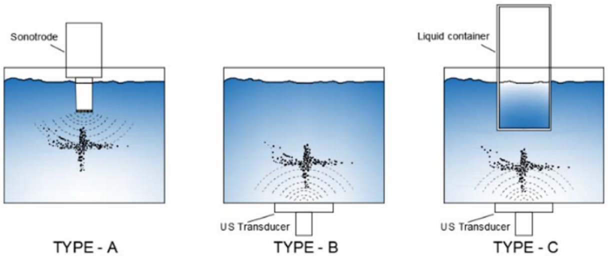

Figure 2.11: Common sono-reactor configurations [10].

between reactor geometry and cavitation distribution is essential for optimizing reactor design and predicting outcomes through simulations. The literature suggests a strong correlation between the resonance of the acoustic field within the reactor and its effect on cavitation behavior. However, questions remain regarding the true influence of eigenvalues and eigenvectors of reactor geometries. It appears that the geometry's impact on the cavitation field is more closely linked to the angle of reflective surfaces rather than the eigenvalues of the structure. Type-B reactors have been studied less extensively.

In rectangular reactors, Koch [19] found no clear geometric correlation with the acoustic field. A comparison of simulations and pressure measurements did not demonstrate any significant eigenvalue effects, and the distribution of sound pressure symmetry was debated [10].

In a type-A reactor, the number of sonotrodes plays a significant role in determining the cavitation coverage within the sonoreactor. Based on Blake's cavitation analysis, a configuration with three sonotrodes operating at 20 kHz in a rectangular reactor increases the cavitation percentage to 61.1% across the reactor volume. However, further increases in the number of sonotrodes per unit volume in a type-A reactor does not necessarily result in a higher cavitation volume [10].

2.2 Sono-Photolysis

2.2.1 Photolysis

Photolysis, or photochemical process, is a mechanism that can be exploited in a water medium to generate the water splitting reaction, as already mentioned in Subsubsection 1.1.2.4. In this case, the energy supply for the reaction is retrieved by the solar irradiation, but not as a source of heat, but as a source of photons: as a first approximation, the solar spectrum composition can be assumed as the radiation generated by a black body at $5800\,K$ — solar surface temperature —, and ranges from short wave ultraviolet (UV-C) at $120\,nm$ wavelength to

near infrared (IR) at $100\,\mu m$ wavelength. Anyway the sun rays absorbed by water are firstly filtered by the atmosphere, and in addition only a portion of the spectrum contains enough energy to cast the H_2O splitting process: because of this issue, it is required a chemical compound that absorbs some of the solar radiation and transfers it into water, helping, or for better saying catalyzing, the whole reaction. This kind of chemical is named photocatalyst, and it plays a really important role in the definition of the photolysis [10].
For large scale hydrogen production, is practical to use as photocatalyst an heterogeneous semiconductor in the form of a particulate material dispersed in the water medium: the semiconductor material absorbs energy equal or larger than its band gap (BG), allowing the promotion of an electron from the valence band (VB) to the conduction band (CB), generating a separated electron - hole pair — $e^- - h^+$ pair —. The opposite charges migrates toward the surface of the solid particles trying to fulfill the two half reaction of the water splitting reaction: the electron reduces the hydrogen ion while the hole takes back an electron from the water molecule, splitting it in oxygen and hydrogen ion [10]:

$$(e^-_{VB} - h^+_{VB})_s + h\nu \rightarrow e^-_{CB,s} + h^+_{VB,s} \tag{2.3}$$

$$H_2O + 2h^+_{VB,s} \rightarrow \frac{1}{2}O_{2,g} + 2(e^-_{VB} + h^+_{VB})_s + 2H^+_{aq} \tag{2.4}$$

$$2H^+_{aq} + 2e^-_{CB,s} \rightarrow H_{2,g} \tag{2.5}$$

Reaction 2.3 is the absorption of the photon by the semiconductor used to make the electron pass to the valence band, Reaction 2.4 is the oxygen evolution reaction (OER) and Reaction 2.5 is the hydrogen evolution reaction (HER): OER is possible only if the electric potential of the hole is higher than the reduction potential of the oxidation reaction of oxygen — 1.23 V —, while HER is possible only if the electric potential of the electron is lower than the hydrogen reduction potential — 0 V —. Summing Reactions 2.4 and 2.5 with the double of the Reaction 2.3 the complete water splitting reaction — with the energetic contribute of the photon — is obtained [10]:

$$H_2O + 2h\nu \rightarrow H_2 + \frac{1}{2}O_2 \tag{2.6}$$

Considering the complete reaction, it seems that suffice to have a photon with $1.23\,eV$, and so a wavelength of $\lambda = 1011\,nm$, to split one water molecule, but in reality the energy provided by the photon to the electron-hole pair is internal energy and not Gibbs free energy, and so all kind of different losses should be taken into account: firstly the entropic factor, that reduces the range of effective solar spectrum, but also other kinetic factors like activation barriers — that may hider the charges migration — and overpotentials. For what concerns the activation barriers, these may be overcome by a photocatalyst with a nanometric structure and high crystallinity, since reducing the internal defects may facilitate the charge motion. Overpotential instead can be circumvented by the usage of a co-catalyst — that helps both the oxydative and reductive steps

—, using material with large band gap — even though this will limit the solar radiation absorption capability — or utilizing a sacrificial reagent that makes the oxidation step easier than the oxidation of oxygen in water [10].

There exist some strategies that can be pursued with the aim of optimize the photocatalysis of H_2 from water, and these includes [10]:

- Engineering the BG of the photocatalyst: usually heterogeneous photocatalyst employed are metal oxides, but their problem is their colour, since they are white and do not absorb the visible light. Three principal strategies have been developed to synthesize colored metal oxides: doping, extension of the valence band and the synthesis of solid solution with colored solvents.
- Utilization of a co-catalyst: different reasons makes this choice valuable as assist to the redox reactions, like the enhancement of the light absorption properties, the facilitation in charge separation, the addition of new catalytically active centers and the reduction of the overpotential, as already mentioned. The typical co-catalyst is based on nobile metals, such as Pt, Au, Ir and Ru, since they are very efficient in offering alternative low energy pathways for electrons and holes, but the major problem related to these materials is their high cost and scarcity.
- The up-conversion of the low-frequency solar radiation input: this strategy helps in reducing the waste of low-frequency component of the incoming radiation, deforming the shape of the spectrum in order to convert two or more low-energy photons into one high-energy photon — blue-shift of the solar spectrum —. These higher-energy photon could be absorbed by the photocatalyst and allow an higher hydrogen yield. The possible mechanisms for the up-conversion are the sequential ground state/excited state absorption, the energy transfer processes, the cooperative processes, the photon avalanche and the sensitized adiabatic photoreactions.

2.2.2 Sonolysis & Photolysis: synergic effect

"The combined action of solar radiation and ultrasounds can exert a synergistic effect on some chemical reactions carried out in liquid phase in the presence of a heterogeneous photocatalyst" [10].

Sono-photolysis is a phenomenon which involves two different processes, sonolysis — analyzed in Section 2.1 — and photolysis — discussed in Subsection 2.2.1 —, with the aim of hydrogen production through water splitting: a water based solution is exposed to both ultrasounds and solar radiations, realizing a possible synergic alternative to electrolysers. This synergic effect is usually computed with Equation 2.7 [10]:

$$\eta_{syn} = \frac{k_{h\nu+US} - (k_{h\nu} + k_{US})}{k_{h\nu+US}} \tag{2.7}$$

where $k_{h\nu}$, k_{US} and $k_{h\nu+US}$ are the kinetic constants of H_2 production when solar radiation — $h\nu$ —, ultrasounds (US) or both inputs are exploited, respectively.
Whenever Equation 2.7 is higher than zero, a synergic effect is present between sonolysis and photolysis: this is a promising field of research although still scarcely investigated, and different aspects of the synergy between light and ultrasounds still need to be completely understood, since it can be due to many different factors [10].
Acoustic cavitation induce the fragmentation of the catalyst's solid particles with an increase of the superficial area of the material, and so a better catalysis; in addition it exploits a stirring effect of the reactive medium, favouring the contact between the liquid and solid phases and lifting the photocatalytic particles from the bottom of the reactor up to the top part, making easier the light capture phenomenon. The photo-induced water splitting instead might provide extra nuclei for bubble formation, promoting the cavitation phenomenon. Another interesting cause to synergy is due to the collapse of cavitation bubbles, affecting the electronic structure of the semiconductor catalyst and causing the acoustic luminescence — promotion of the electrons migration from the valence band to the conduction band —. Additional effects can be observed in presence of a pietzoelectric photocatalyst, that generates a periodic electric potential because of the interaction with the US stimulation and so enhances the charge separation in the catalyst. The presence of a photocatalyst in the form of a dispersed powder in the solution affects the US acoustic field behaviour, and in particular it is manifested in a variation of the kinematic viscosity of the solution that results in a change in the acoustic absorption of the medium: it has been proved that there exist a inverse proportionality between the kinematic viscosity — that increases with the presence of a powdered catalyst — and the acoustic absorption — that instead decreases —.

It is important to remark some consideration highlighted by the scientific literature [10]:

- The sono-photo reactor should be covered by a transparent quartz glass to allow a broader transmission of light from the UV spectrum;
- The proper function of the photolysis is ensured by the presence of a dispersed photocatalyst and the use of a sacrificial agent;
- The use of a bioproduct as a sacrificial reagent permits an hydrogen production without the production of oxygen, that can partially deplete the hydrogen yiled because of combustion reactions;
- The up-converting material capsules should be used to reduce the waste of low-energy photons;
- Sonolysis hydrogen production is sensitive to the chemical composition of the solution, and a solution with 20% of water and ethanol accelerates the production rates of around 40% than the solutions with only water;

- The volume of the solution and so the reactor geometry deeply influence the efficiency of the sonolysis, since these parameters determine the peak resonance points of the water volume exposed to the US stimulation, as explained in Section 3.2;
- Atmospheric pressure conditions give the best results in terms of efficiency of the sonolysis and sono-photolysis;
- Type A or B sonoreactor can achieve the best performances for low frequency range ultrasounds, with a duty cycle transducer activity of 60%, in Ar atmosphere to achieve the largest bubble dimension at the highest temperature.
- It is possible to have catalysts that reduce the kinematic viscosity of the solution and as a consequence increase the acoustic absorption;
- Sono-photolysis exhibits a synergic effect of approximately 13%, and the efficiency advantages with a sulfur doping of the catalysts are relevant in the initial three hours of combined actions of US and solar radiation.

2.3 Aim of this work

Sonochemistry is a really versatile technology, and can be employed for many different purposes, such as the purification of water, surface cleaning, disinfection, synthesis of drugs and medicines, and last but not least the production of hydrogen [26]. The focus of this thesis is on the potentiality of the sonolysis of water in the context of hydrogen production, and mostly when this technology is adopted in combination with photolysis: the sono-photolysis process is in fact a promise for the incoming future in the production of green hydrogen, and it is important deepen those aspects that require a major comprehension in order to optimize the production and making it competitive in the hydrogen economy [10]. What will be analyzed in Chapter 3 and Chapter 4 are respectively the methods and results coming from the study of the acoustic cavitation field in a cylindrical sono-reactor, comparing a software simulation procedure with direct measurements.

In Subsection 3.2.1 it has been shown the mathematical modeling framework for the propagation of sound in a generic enclosed medium volume, with different simplified hypothesis and approximations: the Laplace's hypothesis — negligible internal heat, that implies an isoentropic propagation of US —, ideal fluid with no viscosity, possibility of ignore the second — and higher — order terms in the acoustic equations — linearization —. This framework is used in many studies in order to understand the efficacy of the sonochemistry in all its application fields, and so also in the production of hydrogen context [26].
Anyway, the simplifications made are not negligible in understanding the whole sonolysis and photo-sonolysis phenomena: first of all, in literature are never underlined the differences that exist in sound propagation in a medium whenever

it is subjected to a sound disturbance with frequencies in the range of audible or in the range of ultrasounds, and this can manifest significant errors in the evaluation of the final acoustic field.
As it is discussed in Subsections 3.2.2 and 3.2.3, further approximations made in order to obtain the solutions of the Helmoltz equations in the case of a cylindrical reactor return a symmetric acoustic pressure field. In addition, no scattering phenomena between the US disturbance propagation and the collapsing cavitation bubbles is taken into account in the mathematical model, generating another source of errors that cannot be ignored. Finally, for the case of sono-photolysis of water, the medium contains a dispersed photocatalyst in powder form, and this affect the kinematic viscosity of the fluid medium and as a consequence the acoustic absorption parameter, as discussed in Subsection 2.2.2, but none of these effects are considered in the actual mathematical simulations [10]. In [27] the simulation efficacy is doubted, because results and measurements are affected by differences: this is due to the impossibility to simulate the cavitation-bubbling evolution, their spatial distribution and the acoustic scattering of ultrasounds by the bubbles in a finite volume software.

This thesis aims to deepen the understanding of the acoustic field within a cylindrical reactor, both when filled with pure water and when containing a mixture of water and $NiAlTi$ photocatalyst. An experimental setup was designed to assess whether mathematical modeling can accurately represent the ultrasonic acoustic disturbances in the sono-reactor.

Chapter 3

Materials and Methods

In alignment with the objective discussed in Section 2.3, an experimental setup was developed in collaboration with the 'Università degli Studi di Perugia' to study the acoustic cavitation field within a cylindrical sono-reactor. This chapter details the process: Section 3.1 describes the laboratory equipment used to generate sonolysis in the reactor and to measure the resulting pressure oscillations; Section 3.2 presents the mathematical model employed to characterize the cavitation field within the cylindrical reactor; and Section 3.3 outlines the measurement procedure, including data post-processing to obtain the pressure field evolution over time, as well as the simulation process, which applies the mathematical model from Section 3.2 within a MATLAB environment.

3.1 Materials

"The sono-reactor is an AISI 304 staineless steel system provided by a $50W$ pietzoelectric transducer at the bottom of a cylindrical vessel, and a multiple solts for temperature probes, gas inlet and outlet (in case of reactor closed configuration)" [9]. Its lateral surfaces are covered by a thermo-isolating material — refractory ceramic wool — in order to avoid any thermal influence from the external when this reactor is used for sono-photolysis reactions.

Figure 3.1: The cylindrical reactor in 'Università degli studi di Perugia', Terni's lab.

Figure 3.2: The cylindrical reactor in 'Università degli studi di Perugia', Terni's lab.

The cylindrical reactor has a diameter of $160\,mm$. When filled with 1 liter of liquid — firstly pure water and then a mixture of pure water and pulverized photocatalyst during the experiments — the liquid's surface is positioned $50\,mm$ above the reactor's bottom.

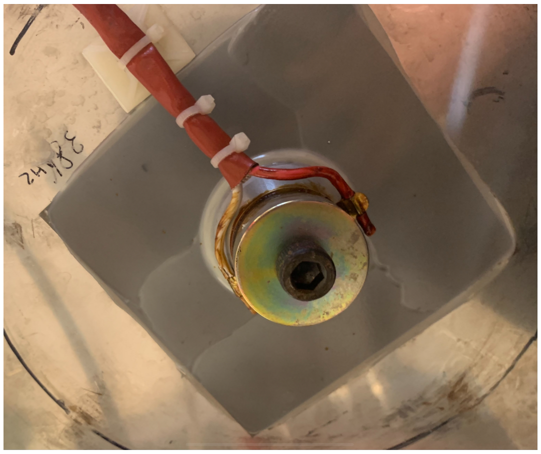

Figure 3.3: Piezoelectric element under the cylindrical vessel, used to induce ultrasounds.

Figure 3.4: Piezoelectric element under the cylindrical vessel, used to induce ultrasounds.

Figures 3.3 and 3.4 represent the pietzoelectric element placed just under the reactor, in order to induce the US acoustic disturbance from the bottom. This pietzoelectric is feed by a 'FISMET 38 kHz PZT-2T series' US generator — maximum power of 50 W and minimum power of 5 W —, shown in Figure 3.5.

Figure 3.5: 'FISMET 38 kHz PZT-2T series' US generator.

The study, as already mentioned, has been performed with two solutions, that are pure water and a mix of pure water and the photocatalyst: the photocatalyst used for the study of the acoustic cavitation field for sono-photolysis application is the $NiAlTi$ — with molar fractions $X_{Ni} = 0.33$, $X_{Al} = 0.33$ and $X_{Ti} = 0.33$ — in a pulverized form. As discussed in Subsections 2.2.1 and 2.2.2, a dispersed photocatalyst permits a better exploitation of the sun rays energy for the water splitting reaction.

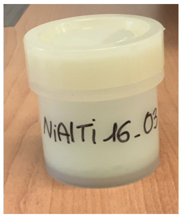

Figure 3.6: $NiAlTi$ photocatalyst in its case.

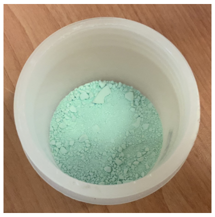

Figure 3.7: $NiAlTi$ photocatalyst in pulverized form: it is possible to notice its characteristics clear green color.

In order to get a specific amount of photocatalyst it has been used a 'KERN ABJ 320-4NM' analytical balance, shown in Figures 3.8 and 3.9.

Figure 3.8: ‘KERN ABJ 320-4NM’ analytical balance.

Figure 3.9: ‘KERN ABJ 320-4NM’ analytical balance during the weight measuring phase.

The oscillating pressure values have been measured by a ‘Miniature Brüel & Kjær Type 8103’ hydrophone probe: it is shown in Figures 3.10 and 3.11. It presents an accuracy of $\pm 10^{-6}\,V$ and a nominal voltage sensitivity of $29\,\mu V/Pa$ [18].

Figure 3.10: ‘Miniature Brüel & Kjær Type 8103’ hydrophone probe.
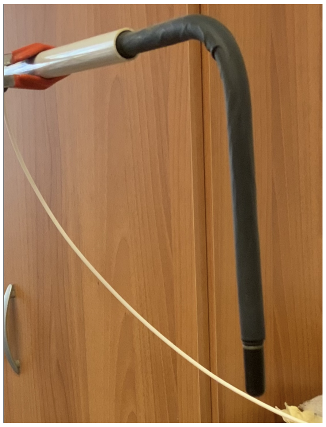
Figure 3.11: ‘Miniature Brüel & Kjær Type 8103’ hydrophone probe in ‘Unversità degli studi di Perugia’, Terni’s lab.

Last but not least, the ‘Picoscope 2000 series Model 2204A’ USB oscilloscope is used to analyze and save on a PC the electrical signal coming from the hydrophone probe, in order to perform the post-processing manipulation of the data on a MATLAB environment — this process is discussed in detail in Section 3.3 —.

Figure 3.12: Picoscope 2000 series Model 2204A' USB oscilloscope.

3.2 Mathematical modeling

3.2.1 Acoustic wave field

The analytical method used to characterize the acoustic field in a certain volume follows closely the conventional approach used to determine the 'room modes' in building acoustics [6].

Acoustic perturbations can usually be regarded as small-amplitude oscillations to an ambient state fluid characterized by certain pressure p_0, density ρ_0 and velocity $\boldsymbol{v_0}$. The overall value of the pressure and density state variables is, considering the acoustic disturbances as p' for pressure and ρ' for density [21]:

$$p = p_0 + p', \qquad \rho = \rho_0 + \rho' \tag{3.1}$$

In order to retrieve the acoustic relations, it is important to remark some hypothesis: firstly, Laplace's hypothesis states that any sound propagation event occurs with negligible internal heat flow, and so with an isoentropic relation true for any fluid particle that undergoes the sound propagation phenomenon — $Ds/Dt = 0$, where s is the unit mass entropy and t is time —. This hypothesis leads to, using also the first principle of thermodynamics and relations in 3.1 [21]:

$$TdS = du + pd\rho^{-1}$$

$$\implies p = p(\rho, s) \implies p_0 + p' = p(\rho_0 + \rho', s_0) \tag{3.2}$$

Another important hypothesis is the one related to the nature of the fluid, that should be ideal and so with no viscosity: as a consequence, the definition of the Euler's equation is [21]:

$$\rho(\frac{\partial}{\partial t} + \boldsymbol{v'}\cdot\nabla)\boldsymbol{v'} = -\nabla p \implies (\rho_0 + \rho')(\frac{\partial}{\partial t} + \boldsymbol{v'}\cdot\nabla)\boldsymbol{v'} = -\nabla(p_0 + p') \tag{3.3}$$

In Equation 3.3, $\boldsymbol{v'}$ is intended the velocity vector induced by the presence of the acoustic disturbance. Last but not least, the mass conservation equation should be taken into account [21]:

$$\frac{\partial \rho}{\partial t} + \nabla \cdot (\rho \boldsymbol{v'}) = 0 \implies \frac{\partial}{\partial t}(\rho_0 + \rho') + \nabla \cdot [(\rho_0 + \rho')\boldsymbol{v'}] = 0 \tag{3.4}$$

In Equations 3.2, 3.3 and 3.4 it has been considered that the ambient state of the medium in which the sounds propagate is quiescent, meaning that $\boldsymbol{v_0} = 0$ and the ambient state variables are independent on time. Furthermore, these equations can be grouped in zero-order terms — not present —, first-order terms — the one that present only one primed variable — and second-order terms — with two primed variables —. For Example the equation 3.2 becomes the Taylor-series expansion of p' [21]:

$$p' = \left(\frac{\partial p}{\partial \rho}\right)_0 \rho' + \frac{1}{2}\left(\frac{\partial^2 p}{\partial \rho^2}\right)_0 (\rho')^2 + \cdots \tag{3.5}$$

where, thanks to the isoentropic sound propagation approximation, each derivative is considered at constant entropy. The linear approximation, that brings to the **linear acoustic equations**, is given considering only the zero and first order terms of Equations 3.2, 3.3 and 3.4 [21]:

$$\frac{\partial \rho'}{\partial t} + \rho_0 \nabla\cdot\boldsymbol{v} = 0 \tag{3.6}$$

$$\rho_0 \frac{\partial \boldsymbol{v'}}{\partial t} = -\nabla p \tag{3.7}$$

$$p' = c^2 \rho', \qquad c^2 = \left(\frac{\partial p}{\partial \rho}\right)_0 \tag{3.8}$$

Thermodynamics requires that c^2 is always positive, and it is, since c represents the speed of sound [21].

From the linear acoustic equations 3.6, 3.7 and 3.8 it is possible to retrieve the **wave equation** of the acoustic propagation — from now on, the use of the prime sign for the sound propagating variables is avoided — [21]:

$$
\begin{aligned}
p = c^2\rho &\implies \rho = \frac{p}{c^2} \\
\frac{\partial \rho}{\partial t} + \rho_0 \nabla \cdot \boldsymbol{v} = 0 &\implies \frac{1}{c^2}\frac{\partial p}{\partial t} + \rho_0 \nabla \cdot \boldsymbol{v} = 0 \\
\implies \frac{1}{c^2}\frac{\partial^2 p}{\partial t^2} + \rho_0 \frac{\partial}{\partial t}(\nabla \cdot \boldsymbol{v}) = 0 &\implies \frac{1}{c^2}\frac{\partial^2 p}{\partial t^2} + \nabla \cdot \frac{\partial \boldsymbol{v}}{\partial t} = 0 \\
\rho_0 \frac{\partial \boldsymbol{v}}{\partial t} = -\nabla p &\implies \frac{1}{c^2}\frac{\partial^2 p}{\partial t^2} - \nabla \cdot \nabla p = 0
\end{aligned}
$$

$$
\left(\frac{1}{c^2}\frac{\partial^2}{\partial t^2} - \nabla^2\right) p(\boldsymbol{x}, t) = 0 \tag{3.9}
$$

Equation 3.9 is the **wave equation** defining the acoustic pressure fluctuation for an enclosed volume V in the location $\boldsymbol{x}$ at time t [6].
“The hypothesis that sound is a wave phenomenon is supported by the fact that the linear acoustic equations and therefore the wave equation have solutions conforming to the notion of a wave as a disturbance traveling through a medium with little or no net transport of matter” [21]. Since sound presents itself as a pressure wave, it is possible to represent it as a sum of constant-frequency waveforms [21]:

$$
p(\boldsymbol{x}, t) = \sum_{h=1}^{N} p_h^{\omega}(\boldsymbol{x}, t); \qquad p_h^{\omega}(\boldsymbol{x}, t) = p_h(\boldsymbol{x}) cos(\omega_h t - \phi_h) \tag{3.10}
$$

In Equation 3.10, ω_h is the angular frequency (and the frequency in Hz is $f_h = \omega_h / 2\pi$), ϕ_n is the phase constant and $p_h^{\omega}(\boldsymbol{x}, t)$ represent the h_{th} frequency component of the whole acoustic disturbance including the sinusoidal time dependency. It is considered that each ω_h is different and they are in ascending order — $\omega_1 < \omega_2 < \cdots$ —.
“If a given waveform $p(t)$ is of interminably long duration but is not immediately recognizable as a superposition of discrete frequency components, one way of describing it as such [...] is with a **Fourier series**” [21]:

$$
p(\boldsymbol{x}, t) = \sum_{h=-\infty}^{\infty} p_h(\boldsymbol{x}) cos(\omega_h t - \phi_h) \tag{3.11}
$$

In Equation 3.11, ω_h is the h_{th} Fourier component angular frequency and ϕ_h is its phase angle at $t = 0\,s$. Substituting Equation 3.11 in Equation 3.9 and imposing that each Fourier component should satisfy independently Equation 3.9, it is defined the **Helmholtz equation** [6]:

$$
\left(\nabla^2 + k_h^2\right) p_h(\boldsymbol{x}) = 0 \tag{3.12}
$$

where $k_h = \omega_h / c$ is the wavenumber of the h^{th} Fourier component. The Helmoltz equation is a second-order partial differential equation, therefore it is important to define two independent boundary conditions for each spatial dimension in order to find a solution. Adding the hypothesis of an enclosure with rigid walls, the wall-normal flow velocity is zero, and as such, by the conservation of momentum in normal direction inside the Euler equation 3.7, it is possible to obtain the boundary conditions [6]:

$$\begin{aligned} \rho_0 \frac{\partial \boldsymbol{v}}{\partial t} \cdot \boldsymbol{n} &= 0 \\ \implies \left(\rho_0 \frac{\partial \boldsymbol{v}}{\partial t} + \nabla p \right) \cdot \boldsymbol{n} &= 0 \end{aligned}$$

$$\nabla p_h(\boldsymbol{x}) \cdot \boldsymbol{n} = 0 \tag{3.13}$$

where $\boldsymbol{n}$ is the inward wall-normal unit vector.

The solution of the Helmoltz equation 3.12 with the boundary conditions 3.13 represents the acoustic pressure field inside an enclosure with rigid walls. It is important to remark that this method is analogous with the one used to retrieve the vibrating modes of mechanical system when subjected to an oscillating force: in fact, in mechanical systems it is necessary to solve the differential equations that come from the application of the second Newton law, while for what concerns the evaluation of the acoustic pressure filed, it comes from the application of the wave equation — combination of the linear acoustic equations, that considers the Euler equation, a fluid dynamic version of the second Newton law — to an oscillatory pressure developed with the Fourier expansion series. The result will give the 'room modes', that are nevertheless that resonances between the oscillating sound perturbation and the medium.

Another interesting point can be observed from the Helmoltz equation 3.12: since the Laplacian ∇^2 is an operator, k_h^2 is a scalar value, and this equation is defined for many pressure components in all the frequency spectrum, it is possible to consider the pressure $p_h(\boldsymbol{x})$ as a vector, and the solutions of the Helmoltz equation as eigenvectors with eignevalues $k_h^2 = \omega_h^2/c^2$ and so eigenfrequencies $f_h = \omega_h/2\pi$.

3.2.2 Helmoltz equations and their boundary conditions for the cylindrical reactor

In order to perform the simulation of the acoustic wave field in the reactor described in Section 3.1, it is necessary to solve the Helmoltz equations expressed in cylindrical coordinates. The following procedure is a reminder on how to convert the gradient of a function and the Laplace's operator from Cartesian to cylindrical coordinates:

$$df(r,\theta,z)=\frac{\partial f}{\partial r}dr+\frac{\partial f}{\partial \theta}d\theta+\frac{\partial f}{\partial z}dz \implies \begin{cases}\frac{\partial f}{\partial x}=\frac{\partial f}{\partial r}\frac{\partial r}{\partial x}+\frac{\partial f}{\partial \theta}\frac{\partial \theta}{\partial x}\\ \frac{\partial f}{\partial y}=\frac{\partial f}{\partial r}\frac{\partial r}{\partial y}+\frac{\partial f}{\partial \theta}\frac{\partial \theta}{\partial y}\\ \frac{\partial f}{\partial z}=\frac{\partial f}{\partial z}\end{cases}$$

$$\begin{cases}x=rcos\theta\\ y=rsin\theta\\ z=z\end{cases} \implies \begin{cases}r=(x^2+y^2)^{\frac{1}{2}}\\ \theta=arctg\left(\frac{y}{x}\right)\\ z=z\end{cases}$$

$$\begin{cases}\frac{\partial r}{\partial x}=\frac{x}{(x^2+y^2)^{\frac{1}{2}}}=cos\theta\ ;\ \frac{\partial \theta}{\partial x}=-\frac{y}{x^2+y^2}=-\frac{sin\theta}{r}\\ \frac{\partial r}{\partial y}=\frac{y}{(x^2+y^2)^{\frac{1}{2}}}=sin\theta\ ;\ \frac{\partial \theta}{\partial y}=\frac{x}{x^2+y^2}=\frac{cos\theta}{r}\end{cases}$$

$$\implies \begin{cases}\frac{\partial}{\partial x}=\frac{\partial r}{\partial x}\frac{\partial}{\partial r}+\frac{\partial \theta}{\partial x}\frac{\partial}{\partial \theta}=cos\theta\frac{\partial}{\partial r}-\frac{sin\theta}{r}\frac{\partial}{\partial \theta}\\ \frac{\partial}{\partial y}=\frac{\partial r}{\partial y}\frac{\partial}{\partial r}+\frac{\partial \theta}{\partial y}\frac{\partial}{\partial \theta}=sin\theta\frac{\partial}{\partial r}+\frac{cos\theta}{r}\frac{\partial}{\partial \theta}\end{cases}$$

$$\begin{cases}\boldsymbol{u_x}=\boldsymbol{u_r}cos\theta-\boldsymbol{u_\theta}sin\theta\\ \boldsymbol{u_y}=\boldsymbol{u_r}sin\theta+\boldsymbol{u_\theta}cos\theta\\ \boldsymbol{u_z}=\boldsymbol{u_z}\end{cases}$$

$$\implies \nabla_{xyz}=\frac{\partial}{\partial x}\boldsymbol{u_x}+\frac{\partial}{\partial y}\boldsymbol{u_y}+\frac{\partial}{\partial z}\boldsymbol{u_z}=$$

$$=\left(cos\theta\frac{\partial}{\partial r}-\frac{sin\theta}{r}\frac{\partial}{\partial \theta}\right)\boldsymbol{u_x}+\left(sin\theta\frac{\partial}{\partial r}+\frac{cos\theta}{r}\frac{\partial}{\partial \theta}\right)\boldsymbol{u_y}+\frac{\partial}{\partial z}\boldsymbol{u_z}=$$

$$=\left(cos\theta\frac{\partial}{\partial r}-\frac{sin\theta}{r}\frac{\partial}{\partial \theta}\right)(cos\theta\boldsymbol{u_r}-sin\theta\boldsymbol{u_\theta})+$$

$$+\left(sin\theta\frac{\partial}{\partial r}-\frac{cos\theta}{r}\frac{\partial}{\partial \theta}\right)(sin\theta\boldsymbol{u_r}+cos\theta\boldsymbol{u_\theta})+\frac{\partial}{\partial z}\boldsymbol{u_z}=$$

$$=\left(cos^2\theta+sin^2\theta\right)\frac{\partial}{\partial r}\boldsymbol{u_r}+\left(\frac{sin\theta cos\theta}{r}-\frac{sin\theta cos\theta}{r}\right)\frac{\partial}{\partial \theta}\boldsymbol{u_r}+$$

$$+(sin\theta cos\theta-sin\theta cos\theta)\frac{\partial}{\partial r}\boldsymbol{u_\theta}+\left(\frac{cos^2\theta}{r}+\frac{sin^2\theta}{r}\right)\frac{\partial}{\partial \theta}\boldsymbol{u_\theta}+\frac{\partial}{\partial z}\boldsymbol{u_z}=$$

$$=\frac{\partial}{\partial r}\boldsymbol{u_r}+\frac{1}{r}\frac{\partial}{\partial \theta}\boldsymbol{u_\theta}+\frac{\partial}{\partial z}\boldsymbol{u_z}=\nabla_{r\theta z}$$

$$\nabla_{xyz}=\frac{\partial}{\partial x}\boldsymbol{u_x}+\frac{\partial}{\partial y}\boldsymbol{u_y}+\frac{\partial}{\partial z}\boldsymbol{u_z}=\frac{\partial}{\partial r}\boldsymbol{u_r}+\frac{1}{r}\frac{\partial}{\partial \theta}\boldsymbol{u_\theta}+\frac{\partial}{\partial z}\boldsymbol{u_z}=\nabla_{r\theta z} \qquad (3.14)$$

$$\nabla^2_{xyz} = \frac{\partial^2}{\partial x^2} + \frac{\partial^2}{\partial y^2} + \frac{\partial^2}{\partial z^2}$$

$$\frac{\partial^2}{\partial x^2} = \frac{\partial}{\partial x}\left(\frac{\partial}{\partial x}\right) =$$
$$= cos\theta\frac{\partial}{\partial r}\left(cos\theta\frac{\partial}{\partial r} - \frac{sin\theta}{r}\frac{\partial}{\partial\theta}\right) - \frac{sin\theta}{r}\frac{\partial}{\partial\theta}\left(cos\theta\frac{\partial}{\partial r} - \frac{sin\theta}{r}\frac{\partial}{\partial\theta}\right) =$$
$$= cos^2\theta\frac{\partial^2}{\partial r^2} + \frac{sin\theta cos\theta}{r^2}\frac{\partial}{\partial\theta} - \frac{sin\theta cos\theta}{r}\frac{\partial^2}{\partial r\partial\theta} +$$
$$+\frac{sin^2\theta}{r}\frac{\partial}{\partial r} - \frac{sin\theta cos\theta}{r}\frac{\partial^2}{\partial\theta\partial r} + \frac{sin\theta cos\theta}{r^2}\frac{\partial}{\partial\theta} + \frac{sin^2\theta}{r^2}\frac{\partial^2}{\partial\theta^2}$$

$$\frac{\partial^2}{\partial y^2} = \frac{\partial}{\partial y}\left(\frac{\partial}{\partial y}\right) =$$
$$sin\theta\frac{\partial}{\partial r}\left(sin\theta\frac{\partial}{\partial r} + \frac{cos\theta}{r}\frac{\partial}{\partial\theta}\right) + \frac{cos\theta}{r}\frac{\partial}{\partial\theta}\left(sin\theta\frac{\partial}{\partial r} + \frac{cos\theta}{r}\frac{\partial}{\partial\theta}\right) =$$
$$= sin^2\theta\frac{\partial^2}{\partial r^2} - \frac{sin\theta cos\theta}{r^2}\frac{\partial}{\partial\theta} + \frac{sin\theta cos\theta}{r}\frac{\partial^2}{\partial r\partial\theta} +$$
$$+\frac{cos^2\theta}{r}\frac{\partial}{\partial r} + \frac{sin\theta cos\theta}{r}\frac{\partial^2}{\partial\theta\partial r} - \frac{sin\theta cos\theta}{r^2}\frac{\partial}{\partial\theta} + \frac{cos^2\theta}{r^2}\frac{\partial^2}{\partial\theta^2}$$

$$\nabla^2_{xyz} = \frac{\partial^2}{\partial x^2} + \frac{\partial^2}{\partial y^2} + \frac{\partial^2}{\partial z^2} = \frac{\partial^2}{\partial r^2} + \frac{1}{r}\frac{\partial}{\partial r} + \frac{1}{r^2}\frac{\partial^2}{\partial\theta^2} + \frac{\partial^2}{\partial z^2} = \nabla^2_{r\theta z} \qquad (3.15)$$

Considering the Helmoltz equations 3.12 and using the definition of the Laplace's operator in cylindrical coordinates expressed in Equation 3.15:

$$\left(\frac{\partial^2}{\partial r^2} + \frac{1}{r}\frac{\partial}{\partial r} + \frac{1}{r^2}\frac{\partial^2}{\partial\theta^2} + \frac{\partial^2}{\partial z^2} + k_h^2\right)p_h(r,\theta,z) = 0 \qquad (3.16)$$

The boundary conditions defined in Subsection 3.13 are not used in all the three dimensions r, θ and z: the circular boundary surfaces on the top and on the bottom are the only one considered rigid (and so perfectly reflective surfaces), and so it is reasonable to adopt a Neumann boundary condition (null velocity in the direction normal to the surfaces) along the z axis direction on the top and bottom circular enclosures of the cylinder. Considering a reference system placed at the centre of the top surface with the vertical z axis going outward the cylinder [6]:

$$\begin{cases} \frac{\partial}{\partial z}p_h(r,\theta,-D) = 0 \\ \frac{\partial}{\partial z}p_h(r,\theta,0) = 0 \end{cases} \qquad (3.17)$$

where D is the depth of the cylinder from the top surface.
Since the dimension θ is an angular dimension, it has no physical boundary surface enclosing its possible values between two limits, and a Neumann boundary condition has no physical meaning when applied to it: a periodic boundary condition is better suited to this situation, so this condition applied to the azimuthal direction:

$$p_h(r,\theta,z) = p_h(r,\theta+2\pi,z) \tag{3.18}$$

For what concerns the radial dimension r, first of all it is considered that the pressure field in the vertical axis (when $r = 0\,mm$) should be finite (again, no physical surface in this situation), and so the boundary condition is:

$$p_h(0,\theta,z) \in \mathbb{R} \tag{3.19}$$

For the second boundary condition in the radial direction instead it has been chosen to consider a Robin boundary condition: it is a mixed condition between the Neumann condition ($\frac{\partial p_h}{\partial n} = 0$, rigid perfectly reflective walls) and the Dirichelet condition ($p_h = 0$, perfectly absorbing walls) that is formally expressed with the Equation 3.20 valid at the boundary surface [20]:

$$\alpha p_h + \beta \frac{\partial p_h}{\partial n} = \gamma \tag{3.20}$$

The coefficient are imposed as $\alpha = \frac{1}{R}$, $\beta = 1$ and $\gamma = 0$, with R the cylinder radius, and the final boundary condition for the radial direction on the lateral surface becomes:

$$\left(\frac{\partial}{\partial r} + \frac{1}{R}\right) p_h(R,\theta,z) = 0 \tag{3.21}$$

This condition implies an acoustic impedance on the lateral walls that is neither infinite — as it happens with the rigid wall hypothesis — nor zero — as it happens with a perfectly absorbing wall —.
In order to better understand the relation between the Robin boundary condition and the impedance value it is necessary to evaluate each h_{th} harmonic component of the acoustic state variables (pressure, velocity flow and density of the propagation medium) as the real part of a complex value. Equation 3.22 shows this reasoning for the pressure wave:

$$P_h = \hat{p}_h e^{-i\omega_h t} = p_h e^{-i(\omega_h t - \phi_h)} = p_h cos(\omega_h t - \phi_h) - i p_h sin(\omega_h t - \phi_h) \tag{3.22}$$

$$\hat{p}_h = p_h e^{i\phi_h} \tag{3.23}$$

$$\implies p_h^{\omega}(r,\theta,z,t) = p_h(r,\theta,z) cos(\omega_h t - \phi_h) = Re\{P_h\} \tag{3.24}$$

where i is the imaginary unit ($i^2 = -1$), $\hat{p}_h$ represents the complex amplitude of the pressure perturbation (that contains info on the phase of the wave) and the Equation 3.24 is obtained combining Equations 3.22 and 3.10. Similar equations and notations apply for velocity and density. The specific acoustic impedance is defined as [21]:

$$Z_s(\omega_h) = \left.\frac{\hat{p}_h}{\hat{v}_{in,h}}\right|_{S_0} \tag{3.25}$$

In Equation 3.25, $\hat{v}_{in,h}$ is the h_{th} frequency component of the complex amplitude of the inward velocity flow ($\boldsymbol{v} \cdot \boldsymbol{n_{in}} = v_{in}$, where $\boldsymbol{n_{in}}$ in the cylindrical reactor case is $\boldsymbol{u_r}$ and the inward velocity complex amplitude is obtained with the same procedure shown for pressure in Equations 3.22 and 3.23) and S_0 is the boundary lateral surface. The real R_s and imaginary X_s parts of the impedance Z_s are named respectively specific acoustic resistance and reactance.
When a Dirichelet boundary condition is applied — $p_h|_{r=R} = 0$, pressure release surface and so complete absorption —, what happens is that also $\hat{p}_h$ is zero, making $Z_s = \frac{0}{\hat{v}_{in,h}} = 0$ (true for both real and imaginary part), while for a Neumann boundary condition ($\left.\frac{\partial p_h}{\partial r}\right|_{r=R} = 0$, null radial velocity at the boundary surface and so complete reflection) happens that, since $v_{in,h} = 0$ also $\hat{v}_{in,h} = 0$, making $Z_s = \frac{\hat{p_h}}{0} = \infty$ for both resistance and reactance.
What happens with the Robin condition described in Equation 3.21 is a bit different. Using the Euler equation 3.7 in radial direction for the complex values of velocity flow and pressure h_{th} frequency component:

$$\rho_0 \frac{\partial V_{r,h}}{\partial t} = -\frac{\partial P_h}{\partial r}$$

$$\Longrightarrow \rho_0 \hat{v}_{r,h} \frac{\partial e^{-i\omega_h t}}{\partial t} = -\frac{\partial \hat{p}_h}{\partial r} e^{-i\omega_h t}$$

$$\Longrightarrow \rho_0(-i\omega_h)\hat{v}_{r,h} = -\frac{\partial \hat{p}_h}{\partial r}$$

$$\Longrightarrow \hat{v}_{r,h} = -\frac{i}{\rho_0 \omega_h} \frac{\partial \hat{p}_h}{\partial r}$$

$$\Longrightarrow \begin{cases} \omega_h = k_h c_0 \\ \hat{v}_{r,h} = -\frac{i}{\rho_0 k_h c_0} \frac{\partial \hat{p}_h}{\partial r} \end{cases} \tag{3.26}$$

The relation $k_h = \frac{\omega_h}{c_0}$ defines the h_{th} wavenumber. Rewriting Equation 3.21 as $\frac{\partial p_h}{\partial r} = -\frac{1}{R} p_h$ and considering that $p_h = \frac{\hat{p_h}}{e^{i\phi_h}}$ from Equation 3.23, it is possible to obtain:

$$\frac{1}{e^{i\phi_h}} \frac{\partial \hat{p}_h}{\partial r} = -\frac{1}{R \cdot e^{i\phi_h}} \hat{p}_h$$

$$\implies \frac{\partial \hat{p}_h}{\partial r} = -\frac{1}{R}\hat{p}_h \tag{3.27}$$

and so, substituting Equation 3.27 in Equation 3.26 evaluated at the lateral wall of the reactor:

$$\hat{v}_{r,h}\big|_{r=R} = -\frac{i}{\rho_0 k_h c_0}\left(-\frac{1}{R}\,\hat{p}_h\big|_{r=R}\right)$$

$$\hat{v}_{r,h}\big|_{r=R} = \frac{i}{\rho_0 k_h c_0 R}\,\hat{p}_h\big|_{r=R} \tag{3.28}$$

Using Equation 3.28 in Equation 3.25 it is possible to finally understand the value that the impedance assumes whenever the Robin boundary condition 3.21 is applied to the lateral walls of a cylindrical reactor:

$$Z_s = \frac{\hat{p}_h}{\hat{v}_{r,h}} = \frac{\hat{p}_h}{\frac{i}{\rho_0 k_h c_0 R}\hat{p}_h} = \frac{\rho_0 k_h c_0 R}{i} = -i\rho_0 k_h c_0 R \tag{3.29}$$

What is eye-catching from the equation 3.29 is that the impedance is reactive, purely imaginary:

$$\begin{cases} Re\{Z_s\} = R_s = 0 \\ Im\{Z_s\} = X_s = -\rho_0 k_h c_0 R \end{cases} \tag{3.30}$$

The Robin condition effect is just to make the velocity flow and the pressure wave out of phase of 90°. The negative sign instead is due to the velocity direction reversal after the impact of the particle with the wall. The wall behaves like a perfectly reflecting boundary, with the difference of imparting a phase shift between velocity and pressure.

3.2.3 Solutions of the Helmoltz equations for the cylindrical reactor

The Helmoltz equation in cylindrical coordinates Equation 3.16 is solved by the separation of variables approach. Letting $p_h(r,\theta,z) = p_{r,h}(r)p_{\theta,h}(\theta)p_{z,h}(z)$, substituting it in Equation 3.16 and dividing it by $p_{r,h}(r)p_{\theta,h}(\theta)p_{z,h}(z)$ [6]:

$$\frac{1}{p_{r,h}}\frac{\partial^2 p_{r,h}}{\partial r^2} + \frac{1}{p_{r,h}}\frac{1}{r}\frac{\partial p_{r,h}}{\partial r} + \frac{1}{p_{\theta,h}}\frac{1}{r^2}\frac{\partial^2 p_{\theta,h}}{\partial \theta^2} + k_h^2 = -\frac{1}{p_{z,h}}\frac{\partial^2 p_{z,h}}{\partial z^2} \tag{3.31}$$

The left hand side is independent from z and the right end side is independent from r and θ, and so the two sides of the equation must match by a constant ζ^2 independent from r, θ and z, leading to the possibility of decoupling the equation Equation 3.31 into the System 3.32 [6]:

$$\begin{cases} \frac{1}{p_{r,h}}\frac{\partial^2 p_{r,h}}{\partial r^2} + \frac{1}{p_{r,h}}\frac{1}{r}\frac{\partial p_{r,h}}{\partial r} + \frac{1}{p_{\theta,h}}\frac{1}{r^2}\frac{\partial^2 p_{\theta,h}}{\partial \theta^2} + k_h^2 = \zeta^2 \\ \left(\frac{\partial^2}{\partial z^2} + \zeta^2\right) p_{z,h} = 0 \end{cases} \tag{3.32}$$

The same reasoning can be applied on the first equation of System 3.32:

$$\left(\frac{1}{p_{r,h}}\frac{\partial^2 p_{r,h}}{\partial r^2}+\frac{1}{p_{r,h}}\frac{1}{r}\frac{\partial p_{r,h}}{\partial r}+k_h^2-\zeta^2\right)r^2=-\frac{1}{p_{\theta,h}}\frac{\partial^2 p_{\theta,h}}{\partial\theta^2} \tag{3.33}$$

with the left hand side independent from θ and the right end side independent from r and z. Making both sides equal to η^2 independent from r, θ and z, it is possible to obtain the system of independent differential equation which solutions returns the three pressure components of the acoustic pressure disturbance in the cylindrical reactor [6]:

$$\left(\frac{\partial^2}{\partial r^2}+\frac{1}{r}\frac{\partial}{\partial r}+\xi^2-\frac{\eta^2}{r^2}\right)p_{r,h}=0 \tag{3.34}$$

$$\left(\frac{\partial^2}{\partial\theta^2}+\eta^2\right)p_{\theta,h}=0 \tag{3.35}$$

$$\left(\frac{\partial^2}{\partial z^2}+\zeta^2\right)p_{z,h}=0 \tag{3.36}$$

with $\xi^2=k_h^2-\zeta^2$, η^2 and ζ^2 all independent from r, θ and z.
The general solution of Equation 3.36 is $p_{z,h}=A_z cos(\zeta z-\alpha_\zeta)$, where A_z is the amplitude of the pressure fluctuation independent from z while α_ζ is the phase angle. Using the boundary conditions for the vertical axis defined by Equations 3.17 it is straightforward that [6]:

$$\begin{cases}\left.\frac{\partial p_{z,h}}{\partial z}\right|_{z=0}=-A_z\zeta sin(-\alpha_\zeta)=0\\[2ex]\left.\frac{\partial p_{z,h}}{\partial z}\right|_{z=-D}=-A_z\zeta sin(-\zeta D-\alpha_\zeta)=0\end{cases}$$

$$\Longrightarrow\begin{cases}\alpha_\zeta=\mp n\pi;\;\; n\in\mathbb{N}^+\\[2ex]-A_z\zeta sin(-\zeta D\mp n\pi)=0\\[2ex]\Longrightarrow\;\zeta=\pm\frac{n\pi}{D};\;\; n\in\mathbb{N}^+\end{cases} \tag{3.37}$$

Therefore:

$$p_{z,h}(z)=A_z cos\left(\frac{n\pi z}{D}\right) \tag{3.38}$$

where it has to be chosen to use a $\alpha_\zeta=0$ since the contribution of the integer n is already highlighted by $\zeta=\frac{n\pi}{D}$ [6].

The general solution for the angular component, since Equation 3.35 has the same form of Equation 3.36, is $p_{\theta,h} = A_\theta cos(\eta\theta - \alpha_\theta)$, with A_θ the oscillation amplitude independent from θ and α_η is the phase-shift angle. Using the periodic boundary condition 3.18 it is possible to obtain [6]:

$$A_\theta cos(\eta\theta - \alpha_\eta) = A_\theta cos[\eta(\theta + 2\pi) - \alpha_\eta] \implies \eta(\theta + 2\pi) = \eta\theta \pm 2m\pi;\;\; m \in \mathbb{Z}^+$$

$$\implies \eta = \pm m;\;\; m \in \mathbb{Z}^+ \tag{3.39}$$

and therefore:

$$p_{\theta,h}(\theta) = A_\theta cos(\pm m\theta - \alpha_m) \tag{3.40}$$

The phase-shift angle with respect to the $\theta = 0$ angle α_m remains indeterminate, and there is no solid boundary nor other reference to lock any of the azimuthal modes to a specific phase angle. Since both $\eta = +m$ and $\eta = -m$ satisfy the periodic boundary condition, the azimuthal component of the h_{th} frequency component of the acoustic pressure can be made up of any arbitrary combination of anti-clockwise $+m$ modes and clockwise $-m$ modes, so it is possible to use superposition to write the final solution for $p_{\theta,h}$ [6]:

$$p_{\theta,h}(\theta) = A_\theta cos(m\theta - \alpha_m) + B_\theta cos(-m\theta - \beta_m) \tag{3.41}$$

The general solution for the Equation 3.34 is instead $p_{r,h} = A_r J_m(\xi r) + B_r Y_m(\xi r)$, where A_r and B_r are the amplitudes for the radial acoustic pressure fluctuation, independent from r, J_m is the m_{th} order Bessel function of the first kind and Y_m is the m_{th} order Bessel function of the second kind. Since Y_m is singular at $r = 0$ and considering the boundary condition 3.19, $B_r = 0$ and so $p_{r,h} = A_r J_m(\xi r)$. Using the Robin boundary condition 3.21 [6]:

$$\frac{\partial J_m}{\partial r} = \frac{\partial J_m}{\partial \xi r}\frac{\partial \xi r}{\partial r} = \xi \frac{\partial J_m}{\partial \xi r}$$

$$\implies \xi R \frac{\partial J_m}{\partial \xi r}(\xi R) + J_m(\xi R) = 0 \tag{3.42}$$

and using the Bessel function property $\xi R \frac{\partial J_m}{\partial \xi r}(\xi R) = m J_m(\xi R) - \xi R J_{m+1}(\xi R)$ [6]:

$$f_m(\xi R) = (m + 1) J_m(\xi R) - \xi R J_{m+1}(\xi R) = 0 \tag{3.43}$$

The Equation 3.43 can be solved numerically for ξ to determine the wavenumbers that satisfy the radial component of the acoustic pressure disturbance, as it is discussed in 3.3.3. Figure 3.13 shows $f_m(\xi R)$ evaluated for five different values of m $(-1, 0, 1, 2, 3)$. The intercept of f_m with the abscissa are the roots of Equation 3.43 [6].

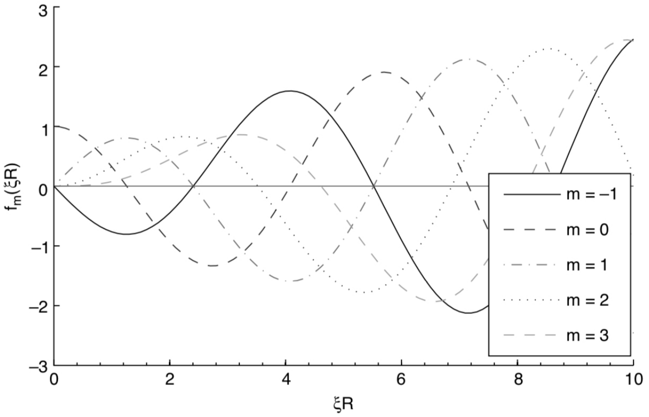

Figure 3.13: f_m function for different m values [6].

Due to the Bessel function properties $J_m = (-1)^m J_{-m}$ and $2mJ_m = \xi R(J_{m+1} + J_{m-1})$, then $f_m = (-1)^m f_{-m}$, and so the clockwise and anti-clockwise spinning modes of the same order m share the same eigenvalue roots (that implies same propagation characteristics) [6].
The oscillatory nature of the Bessel function is such that, for any given m, there is an infinite number of intersections of f_m with the abscissa for $\xi R \geq 0$. The roots of Equation 3.43 have been numbered consecutively for increasing ξR, so that $\xi_{l,m}R$ is the l_{th} root of f_m for the azimuthal mode m, where $l \in \mathbb{Z}^+$. Therefore the radial acoustic pressure wave is [6]:

$$p_{r,h}(r) = A_{l,m} J_m(\xi_{l,m} r) \tag{3.44}$$

Considering that the eigenfrequencies $f_h = \omega_h/2\pi$, $\omega_h = c \cdot k_h$ and $k_h^2 = \xi^2 + \zeta^2$, then the resonance eigenfrequencies are [6]:

$$f_{l,m,n} = \frac{c}{2\pi}\sqrt{\xi_{l,m}^2 + \left(\frac{n\pi}{D}\right)^2} \tag{3.45}$$

with $l, m, n \in \mathbb{Z}^+$. The h_{th} acoustic harmonic component for any given acoustic resonance $f_{l,m,n}$ is [6]:

$$\begin{aligned} p_h(r,\theta,z) = p_{r,h}(r)p_{\theta,h}(\theta,h)p_z(z) = p_{l,m,n}(r,\theta,z) = \\ = A_{l,m,n}J_m(\xi_{l,m}r)cos(m\theta - \alpha_m)cos\left(\frac{n\pi z}{D}\right) + \\ + B_{l,m,n}J_m(\xi_{l,m}r)cos(-m\theta - \beta_m)cos\left(\frac{n\pi z}{D}\right) \end{aligned} \tag{3.46}$$

That, using $J_m = (-1)^m J_{-m}$ and factorizing $(-1)^m$ in $B_{l,m,n}$ becomes [6]:

$$p_{l,m,n}(r,\theta,z) = A_{l,m,n}J_m(\xi_{l,m}r)cos(m\theta - \alpha_m)cos\left(\frac{n\pi z}{D}\right) \tag{3.47}$$

where again $l, m, n \in \mathbb{Z}^+$ [6].

The time dependent acoustic pressure fluctuation inside the cylindrical reactor due to all the resonant modes can be obtained, according to the Fourier series expansion 3.11 [6]:

$$p(r,\theta,z,t) = \sum_{l=0}^{\infty}\sum_{m=0}^{\infty}\sum_{n=0}^{\infty} p_{l,m,n}(r,\theta,z)cos(2\pi f_{l,m,n}t - \phi_{l,m,n}) \tag{3.48}$$

where $\phi_{l,m,n}$ is the phase angle mode (l, m, n) at time $t = 0$ and $p_{l,m,n}(r, \theta, z)$ is the one obtained with Equation 3.47.

3.3 Methods

3.3.1 Measurements acquisition

As already introduced in Section 3.1, the acoustic cavitation field measurements are performed for two different liquid mixtures subjected to sonolysis, that are first 1 liter ($50\,mm$ high form the bottom) of pure water and then 1 liter of pure water mixed with $0.5\,g$ of $NiAlTi$ photocatalyst: it is important to understand the pressure oscillation differences (and so the differences in the cavitation bubbles generation) between the two cases, with the prospective of application of sono-photolysis process for hydrogen production.

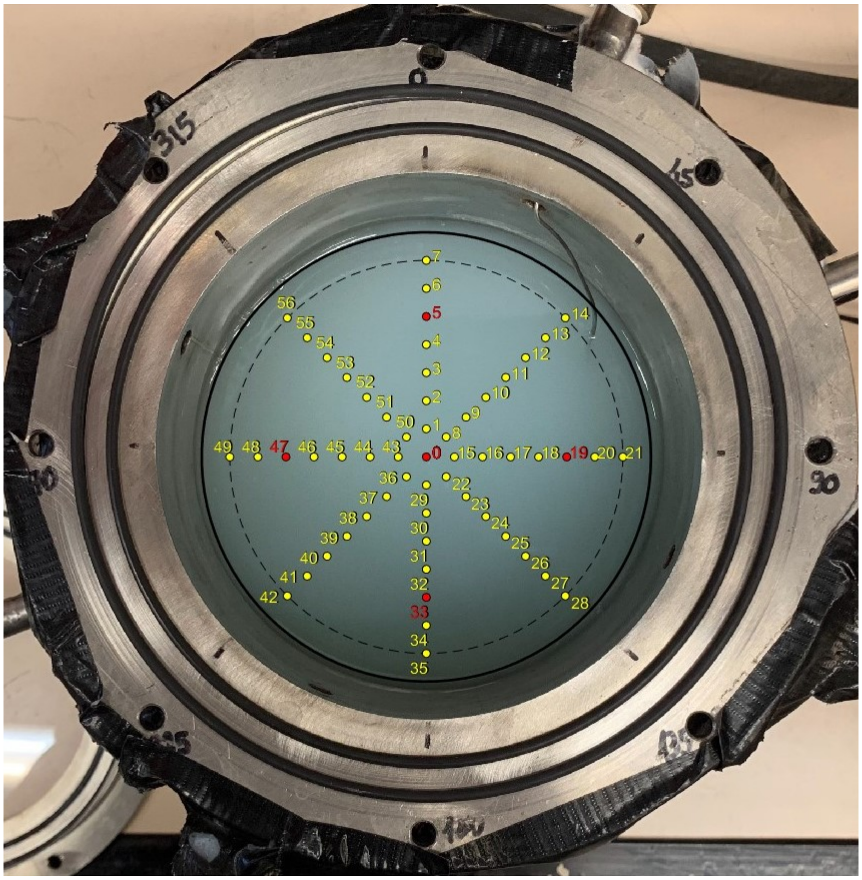

Figure 3.14: Mesh of measurement points from the top-view of the sono-reactor. Each measurement point is numbered to make it recognizable. In point 0 (centre), point 5, point 19, point 33 and point 47 the measurements are performed also at different height.

Figure 3.14 shows the mesh of points measured in this experimental set up with the 'Miniature Brüel & Kjær Type 8103' hydrophone probe: all the measurements are performed at 10 mm from the bottom, with the exception of the red points, in which the measures are taken for four different heights (10 mm, 20 mm, 30 mm and 40 mm from the bottom of the reactor). The angle between each direction is 45° for a total of 4 directions and the distance between each adjacent point in the same direction is of 10 mm, and so considering 7 points between the centre and the lateral wall, each line covers 140 mm with 14 points on a diameter of 160 mm. Only 10 mm from the borders are not taken into account by the mesh that, considering the 4 measuring direction, covers most of the reactor surface and is possible to detect any asymmetry if present.

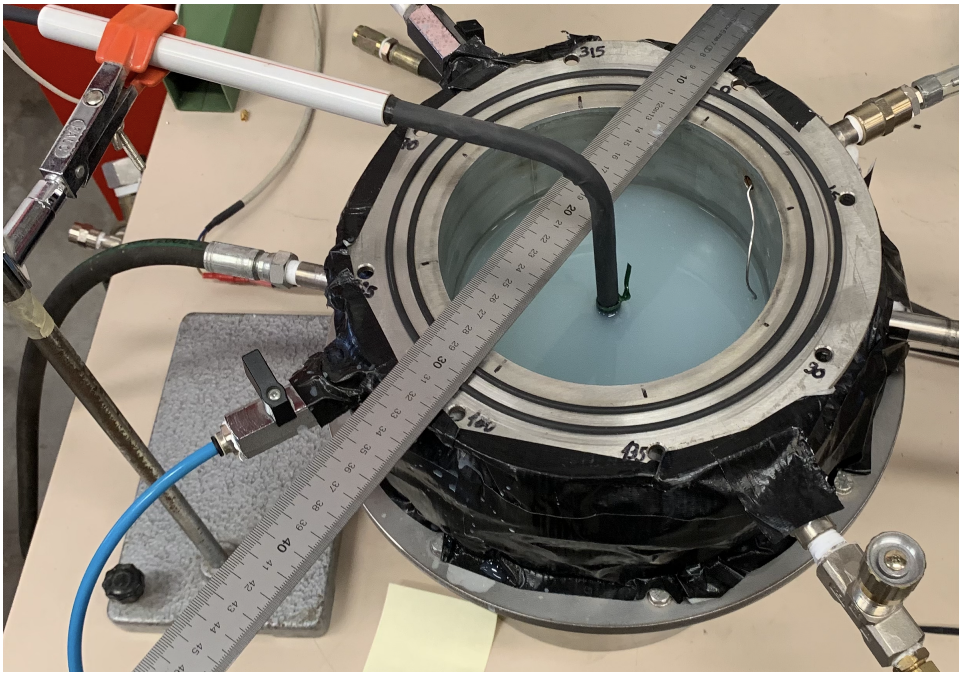

Figure 3.15: Final configuration for the experimental setup (case sonolysis of mixture water-$NiAlTi$ photocatalyst).

The hydrophone probes measures the pressure oscillations, converting them into an electric signal that is sent to the connected 'Picoscope 2000 series Model 2204A' USB oscilloscope, connected in turn to a PC that, using 'Picoscope7 Test & Measurement' software, displays the acquired signal.
The data acquisition phase is made setting up from the software the sampling frequency to $250\,kS/s$ that, in a $50\,s$ acquisition (with 10 divisions, resulting in $5\,s$ per division), correspond to $12.5\,MS$ per acquisition.

Each acquisition includes 3 different steps: the first step (between $0\,s$ and $15\,s$) is the acquisition of the signal when the reactor is subjected to a minimum power sonolysis, the second step (between $15\,s$ and $30\,s$) is the transient phase acquisition, with a gradual increase of US generator power from the minimum to the maximum, while the third phase (between $30\,s$ and $50\,s$) involves the acquisition of the signal when the sonolysis is occurring with a maximum power input. The power levels of the 'FISMET $38\,kHz$ PZT-ZT series' US generator, as described in Section 3.1, are $50\,W$ for the maximum power and $5\,W$ for the minimum.
Figure 3.16 is showing a result from the procedure just explained.

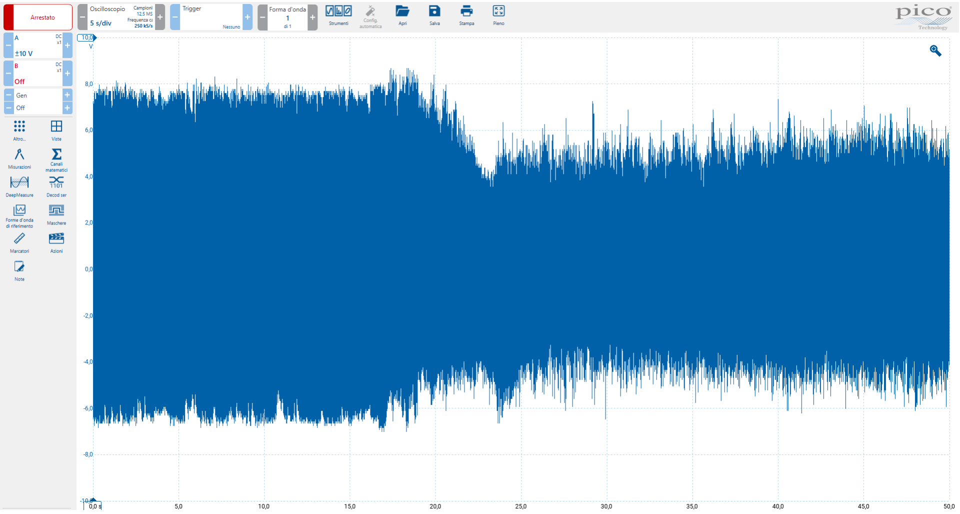

Figure 3.16: Exampe of a signal aquisition with 'Picoscope7 Test & Measurement' software. The signal in this case is taken in the centre of the sono-reactor, when it is filled with water-photocatalyst mixture.

Each $50\,s$ acquisition is saved in two formats: '.psdata' as a backup save compliant with the 'Picoscope7 Test & Measurement' software, and '.mat' compliant with MATLAB and used in the successive post-processing phase of the measurements.
This procedure is repeated for all the 57 points of the mesh at $10\,mm$ height, and for 5 points (position 0, position 5, position 19, position 33 and position 47) at other 3 height levels ($20\,mm$, $30\,mm$, $40\,mm$) before the signal post-processing step.

3.3.2 Data post-processing

3.3.2.1 Pressure maps

The post-processing phase of the acquired data is made with the MATLAB environment.
The saved '.mat' version of the acquired data is loaded into the environment, and some useful parameters are defined, as the sampling frequency $F_s = 250\,kS/s$, the number of samples $S_{\#} = 12.5\,MS$, the time between one sample acquisition and another $\Delta t_s = 50\,s/S_{\#}$ (where $50\,s$ is the time duration of the signal acquisition), the discrete time vector (useful for time-domain plots) where each i_{th} element is $t_i = i \cdot \Delta t_s$, for $i = 0, 1, ..., (S_{\#} - 1)$; the Niquist frequency $F_{Niq} = F_s/2$, the discrete frequency vector (useful for frequency-domain plots), where each i_{th} element is $F_i = i \cdot \frac{F_{Niq}}{S_{\#}} - \frac{F_{Niq}}{2}$, for $i = 0, 1, ..., (S_{\#} - 1)$; and last but not least the hydrophone probe sensitivity $Hyd_{Sens} = 29 \cdot 10^{-6}\,V/Pa$ used

to convert the electric signal acquired in V in a pressure oscillation in Pa.

The loaded data are then converted from electrical to a pressure signal and then collected in a single matrix with 57 rows (one for each measured point) and $12.5 \cdot 10^6$ columns (one for each sample of the $50\,s$ acquisition): this matrix represent a collection of time-domain pressure signals. After that it is calculated the matrix that represent instead the collection of frequency-domain pressure signals, made using the MATLAB function 'fft()', that calculates the discrete Fourier transform (DFT) of a function using a fast Fourier transform (FFT) algorithm.

Analyzing the signals' spectrum, the resonant frequency is in between $38\,kHz$ and $50\,kHz$, and so the next step involves the band pass filtering of the signals in that range of frequencies in order to analyze just the resonant pressure component of all the signals and compare them with the results of the simulation, made with the process described in Subsection 3.3.3. This filtering process is made with the MATLAB function 'bandpass()' set for the range $[38\,kHz, 50\,kHz]$ with a sample rate $F_s = 250\,kS/s$ just defined. Figures 3.17 and 3.18 shows the filtering action on the pressure signal for the central position and the 5^{th} position in the reactor, respectively, both for the case of the reactor filled with 1 liter of water-$NiAlTi$ mixture:

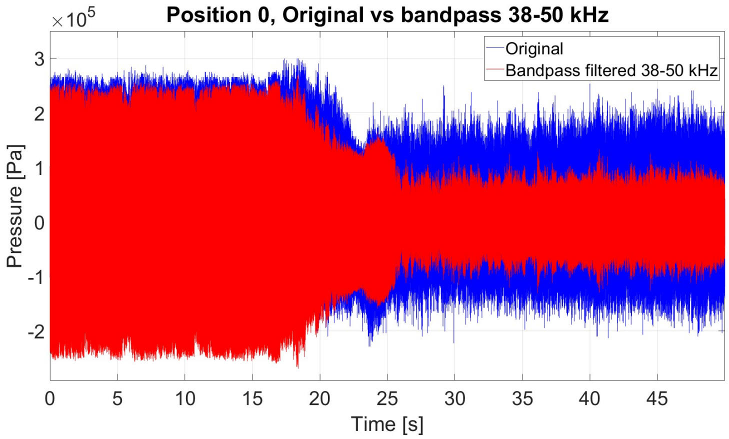

Figure 3.17: Filtering action on the pressure signal in position 0, water-$NiAlTi$ mixture.

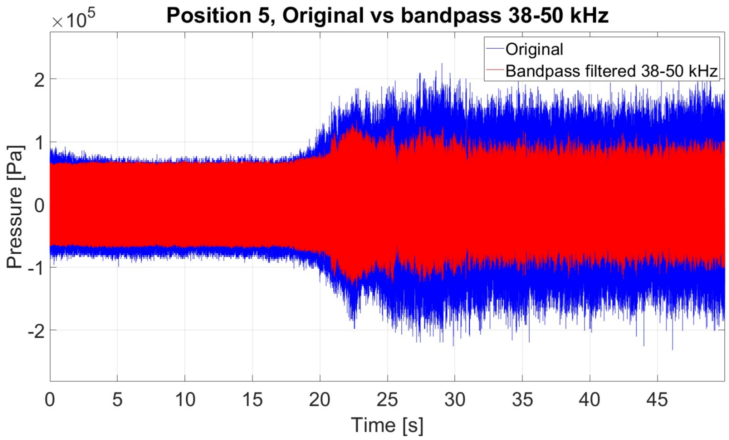

Figure 3.18: Filtering action on the pressure signal in position 5 water-$NiAlTi$ mixture.

The filtered pressure oscillation signals matrix is used to generate time-dependent pressure maps that are analyzed in detail in Chapter 4. Despite the mesh of measured points covers most of the cylindrical surface of the reactor, there are many other points that requires to be measured in order to derive a proper pressure map. In order to overcome this problem, the pressure values between different points are obtained with a cubic interpolation, that permits to get a smoother interpolation that could better represent the real pressure trend between points. This cubic interpolation is made between $250 \times 250 = 62500$ points created considering 250 elements in the r domain (250 elements in a $70\,mm$ radius means $\Delta r = 160/250 = 0.28\,mm$ definition) and 250 elements in the θ domain ($\Delta\theta = 2\pi/250 = \pi/125 = 0.0251\,rad$ definition), that are converted in Cartesian coordinates for a proper use in the ‘contourf()’ function (that creates the pressure map).

A time-evolving pressure map is generated, choosing three specific frames in both the low power stimulation time interval ($[0\,s, 15\,s]$) and the high power stimulation time interval ($[30\,s, 50\,s]$): each frame is a peculiar moment of the measurement in that time interval, and in particular these are the maximum peak, the minimum peak and a zero crossing value in the center of the time interval (the point with the pressure value closest to zero).

3.3.2.2 Pressure-height plots

For what concerns the measures taken at different heights, these are taken only at position 0, position 5, position 19, position 33 and position 47: the post-processing procedure follows the same process described for the extrapolation of the pressure maps (data loading in MATLAB, electrical-pressure signal conversion, signal filtering, plot generation), with the main difference that the generated results are linear plots pressure-height, with a focus on their maximum and minimum amplitudes during the low and high power phases. The plot generation does not require a cubic interpolation with high definition, and so the graphs results linear.

3.3.3 Acoustic cavitation field simulation

3.3.3.1 Pressure maps

The simulation procedure is made implementing the mathematical model defined in Section 3.2 into the MATLAB environment.

Firstly it is required to define the input data, that are the reactor dimensions $R = 80\,mm$ (radius) and $D = 50\,mm$ (water depth) and the speed of sound in aqueous media $c \simeq 1500\,m/s$. The values of ξ for $\xi R \in [0, 10]$ with a discrete ξR definition equal to 10^{-4} are also defined at this stage.

The next step is the calculation of the numerical solution of Equation 3.43 to determine the wavenumbers ξ: this calculation is performed for the azimuthal wavenumbers $m = -1, 0, 1, 2, 3$. The solutions are obtained interpolating linearly between each ξR pair lying on either side of each zero crossing [6], with an interval $\Delta\xi R = 10^{-6}$. Per each f_m are obtained 3 wavenumbers, characterized by the index $l = 1, 2, 3$.

After that, the values $\xi_{l,m}$ that satisfy the Equation 3.43 are known, and it is possible to calculate the eigenfrequencies using the formulation 3.45. This calculation is performed for $n \in [1, 10^4]$, $m \in [-1, 5]$ and $l \in [1, 3]$ and in particular only the modes l, m, n that gives eigenfrequencies in the range $[38\,kHz, 50\,kHz]$ are selected, as a sort of filtering action on the total pressure wave, as it happens for measured data in Subsection 3.3.2.

The final step involves the calculation of the eigenvectors, that are the acoustic pressure components, and the plotting of the total pressure maps (obtained by superimposing all the spectral components in the selected spectrum and multiplying them by their time dependency factor, as shown by Equation 3.48) for different time steps. Each acoustic mode is calculated in the same 57 points shown in Figure 3.14 that have been measured following the procedure described in Subsection 3.3.1, considering the height $z = -40\,mm$, all their initial phases $\alpha_m = \pi/2$ (following the hypothesis explained in [6]), and all their amplitudes $A_{l,m,n} = 1.7 \times 10^5$, to make them compliant with the order of magnitude observed for the measured pressure oscillations.

For the total pressure calculation it has been chosen to restrict the investigation on the time interval $[24.9975\,s, 25.0025\,s]$ that stands in the middle the total acquisition time of $50\,s$ and that lasts for $0.005\,s$: this choice has been made to permit the use of a sufficiently fine time discretization ($\Delta t = 4 \times 10^{-6}\,s$) that can catch even the variations of the highest frequency component of the total

pressure (that is the one of $50\,kHz$, corresponding to a $2 \times 10^{-5}\,s$ period) without having to many pressure map frames to calculate. Considering in fact an interval of $0.005\,s$ discretized by a $\Delta t = 4 \times 10^{-6}\,s$ there are 1250 time instant for which a pressure map should be retrieved, and considering that a pressure map requires a calculation on 57 different points of the reactor and that in each point should be calculated and summed together all the l,m and n components ($6 \times 4 \times 10^4 = 24 \times 10^5$ elements), the number of calculations involved in the total pressure map time evolution in the interval $[24.9975\,s, 25.0025\,s]$ amounts to 1.62×10^{11}. Enlarging the time interval without changing the number of points in the discretization of time implies a loss in definition of the total pressure function, risking a loss of information on the higher frequency components. On the other hand, a wider time interval with the same Δt increases the number of points of the discretization, heavily affecting the time required by MATLAB to compute the pressure maps.
With the current set-up, the time required for the calculation of the total pressure map in each instant in the selected interval requires almost 35 minutes. The evaluation of the pressure in points not covered by the mesh is obtained with the same cubic interpolation procedure (and the same interpolating mesh) described in Subsection 3.3.2.

The pressure map frames plotted are chosen to be the one with the maximum and minimum pressure peak inside the reactor, the one with the maximum and minimum pressure peak in the central position of the reactor and the one that presents the pressure value closest to the zero crossing in the central position.

3.3.3.2 Pressure-height plots

The pressure dependence on height z is showed with different plots, obtained at the coordinates of position 0, position 5, position 19, position 33 and position 47 for $z = -40\,mm$, $z = -30\,mm$, $z = -20\,mm$, $z = -10\,mm$: in particular the obtained figures highlights the maximum and minimum pressure amplitude for each position in the same interval selected for the pressure map frames. The procedure to obtain each acoustic mode is the same seen for the pressure maps, but are evaluated on different z values and not in a mesh of copious points of a single planar circular surface.

Chapter 4

Results Analysis

This chapter presents a discussion of the results obtained through the methodology outlined in Section 3.3. The first part focuses on the simulation results derived from the procedure detailed in Section 3.3.3, which are based on the mathematical model described in Section 3.2 and implemented in the MATLAB environment. The second section examines the experimental results of the pressure field measurements within the sono-reactor, following the methodology described in Subsection 3.3.1 and Subsection 3.3.2, for both water sonolysis and the sonolysis of the water-photocatalyst mixture. In the final two sections, a direct comparison between the simulation and experimental results is made, highlighting the key limitations of the simulation, which are further discussed in the conclusions.

4.1 Simulation Results

4.1.1 Pressure maps

In the present subsection, the total pressure map frames, generated by the mathematical simulation model introduced in MATLAB, are discussed in detail. To begin, it is important to recall which frames were selected as representative of the situation within the sono-reactor. As discussed in Subsection 3.3.3, the simulation was conducted over a $0.005\,s$ time interval $[24.9975\,s, 25.0025\,s]$, chosen to represent the overall propagation of the acoustic disturbance, since it stands in the middle of the $50\,s$ duration of the parallel signal acquisition and encompasses 250 periods of the highest frequency component ($50\,kHz$) and 190 periods of the lowest frequency component ($38\,kHz$) of the total pressure wave.

The pressure map frames selected for a graphical representation correspond to those containing both maximum and minimum pressure peaks, whatever the position: these peaks occur at the same time instant, $t = 24.9981\,s$, and are located in position $(r, \theta) = (40\,mm, 45°)$ (position 11, maximum pressure) and position $(r, \theta) = (40\,mm, 315°)$ (position 55, minimum pressure). These peaks present a pressure value of $\pm 3.27 \times 10^5\,Pa$. Figures 4.1 and 4.2 illustrate the total pressure trend over time for position 11 and position 55 respectively, with a focus on the maximum and minimum pressure values used to select the significant time frame for the pressure map, while Figure 4.3 presents the pressure map at the instant $t = 24.9981\,s$.

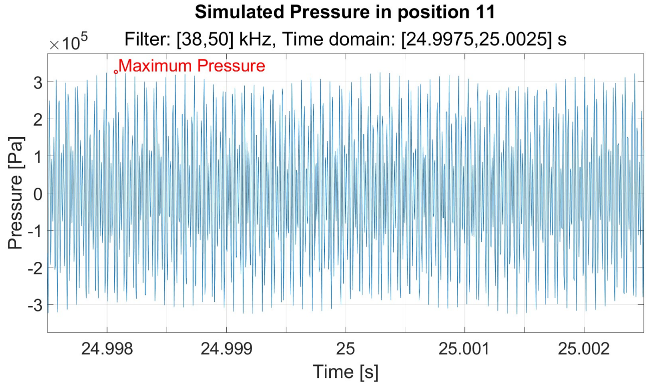

Figure 4.1: Simulated pressure trend in position 11 $(r, \theta) = (40\,mm, 45°)$, time domain $[24.9975\,s, 25.0025\,s]$. Pressure filtered in $[38, 50]\,kHz$. Focus on the maximum pressure value ($t = 24.9981\,s$, $p = 3.27 \times 10^5\,Pa$).

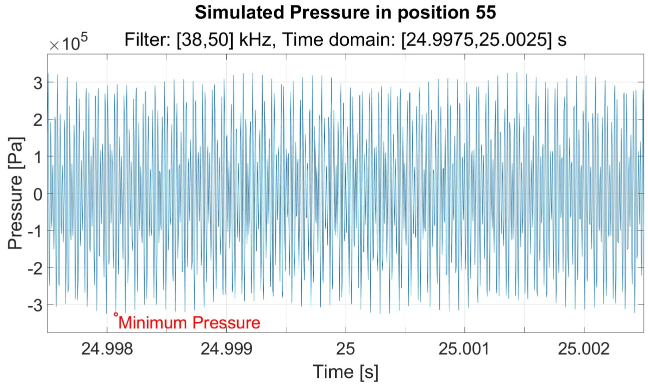

Figure 4.2: Simulated pressure trend in position 55 $(r, \theta) = (40\,mm, 315°)$, time domain $[24.9975\,s, 25.0025\,s]$. Pressure filtered in $[38, 50]\,kHz$. Focus on the minimum pressure value ($t = 24.9981\,s$, $p = -3.27 \times 10^5\,Pa$).

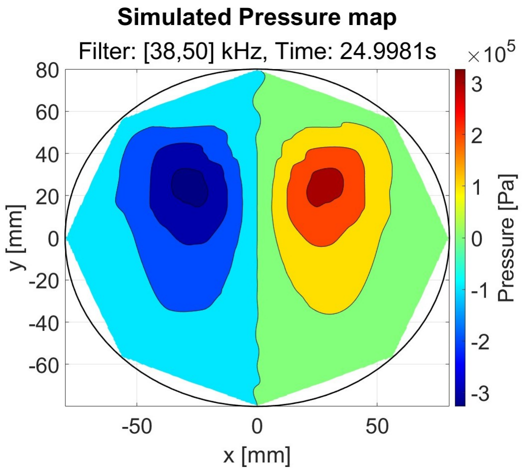

Figure 4.3: Simulated pressure map at time $24.9981\,s$, instant in which are present the maximum values in position 11 ($3.27 \times 10^5\,Pa$) and position 0 ($2.38 \times 10^{-11}\,Pa$), and the minimum value in position 55 ($-3.27 \times 10^5\,Pa$).

An examination of Figure 4.1 and 4.2 reveals the periodic nature of the total pressure. Varying the time interval of analysis would not yield additional information beyond what is presented in this section. Additionally, from Figure 4.1, 4.2 and 4.3, it is important to highlight the symmetry observed relative to the diameter of the circular section of the reactor: while the left side consistently exhibits a negative pressure trend across all positions, the exact opposite occurs on the right side. This symmetrical specular behavior is maintained across all analyzed frames of the pressure maps generated by the MATLAB simulation.

At the same time instant also the central position (position 0) exhibits the maximum pressure value of $2.38 \times 10^{-11}\,Pa$, which is significantly lower than the pressure at position 11.
The central position is particularly useful for identifying other notable frames, including those with the minimum pressure and the pressure value closest to zero: the total pressure trend with an emphasis on these selected points is shown in Figure 4.4, with a zoom on the zero-crossing point in Figure 4.5. Figure 4.6 and 4.7 display the pressure maps at $t = 24.9978\,s$ (zero-crossing point in the centre) and $t = 25.0014\,s$ (minimum pressure at the centre), respectively.

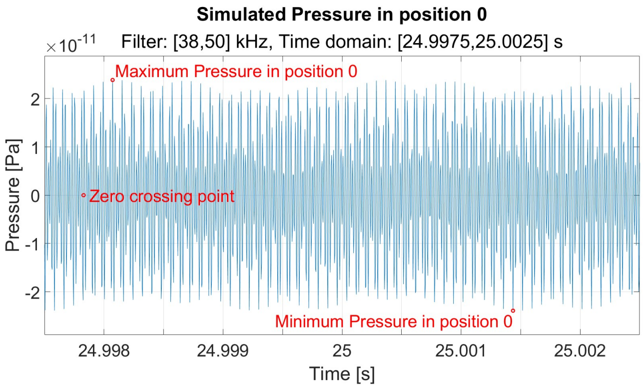

Figure 4.4: Simulated pressure trend in position 0 ($r = 0\,mm$), time domain $[24.9975\,s, 25.0025\,s]$. Pressure filtered in $[38, 50]\,kHz$. Focus on the maximum pressure value ($t = 24.9981\,s$, $p = 2.38 \times 10^{-11}\,Pa$), minimum pressure value ($t = 25.0014\,s$, $p = -2.38 \times 10^{-11}\,Pa$) and the point closest to zero pressure value ($t = 24.9978\,s$, $p = 9.18 \times 10^{-15}\,Pa$).

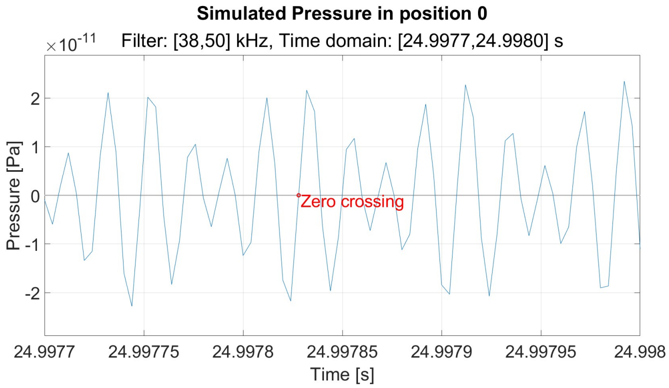

Figure 4.5: Simulated pressure trend in position 0 ($r = 0\,mm$), time domain $[24.9977\,s, 24.9980\,s]$. Pressure filtered in $[38, 50]\,kHz$. Focus on the point closest to zero pressure value ($t = 24.9978\,s$, $p = 9.18 \times 10^{-15}\,Pa$).

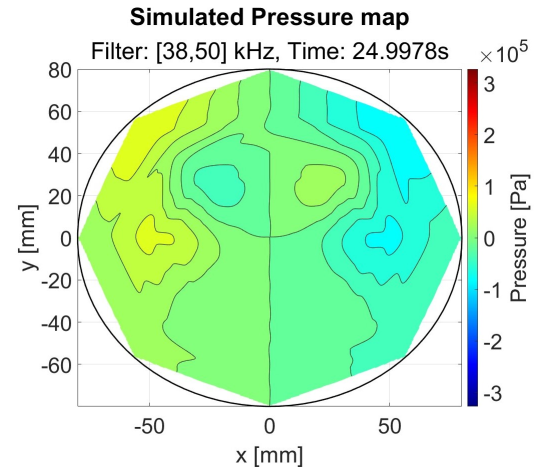

Figure 4.6: Simulated pressure map at time $24.9978\,s$, instant in which is present the point closest to zero pressure value in position 0 ($9.18 \times 10^{-15}\,Pa$).

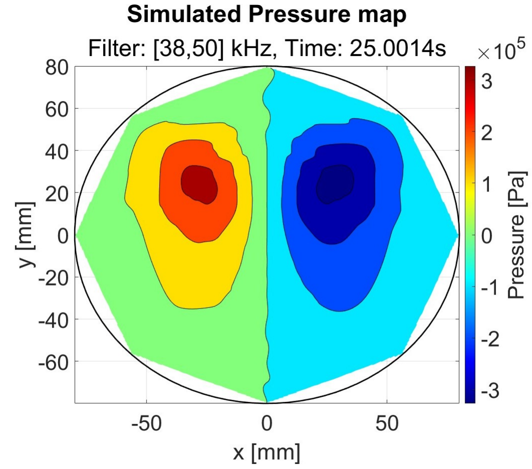

Figure 4.7: Simulated pressure map at time $25.0014\,s$, instant in which is present the minimum value in position 0 ($-2.38 \times 10^{-11}\,Pa$).

As previously noted, the symmetry trend is preserved, though Figure 4.7 exhibits an exact inverse trend compared to 4.3. In contrast, Figure 4.6 displays a markedly different pattern, with pressure values across the map remaining very close to zero, despite minor disturbances.

For completeness, Figure 4.8 presents the time-ordered sequence of pressure map frames, illustrating the time evolution of the simulated total acoustic pressure disturbance.

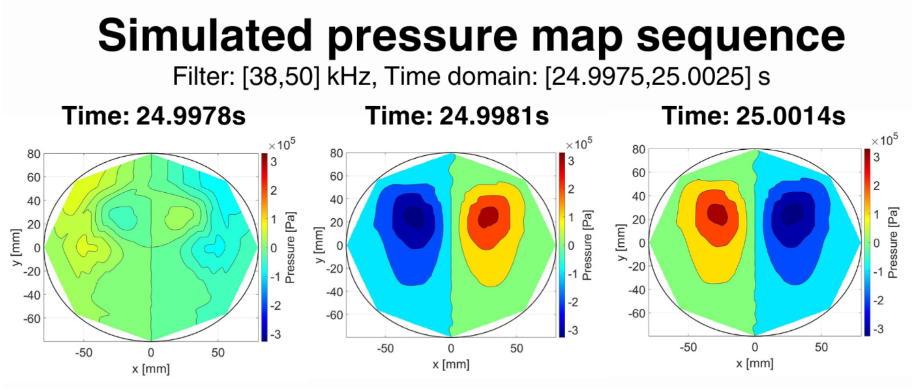

Figure 4.8: Simulated pressure map, time-ordered frames sequence.

4.1.2 Pressure-height plots

This subsection presents and explains the simulated total pressure variation with height. Following the procedure outlined in Subsection 3.3.3, the generated pressure-height plots for position 0, 5, 19, 33 and 47, shown in Figure 4.9, illustrate the maximum and minimum amplitude values obtained within the time interval $[24.9975\,s, 25.0025\,s]$.

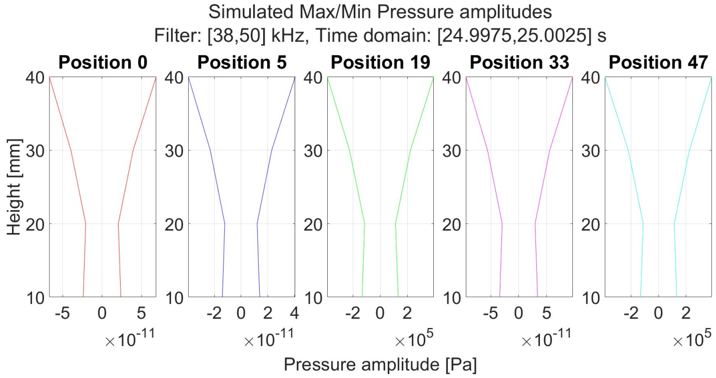

Figure 4.9: Simulated maximum and minimum pressure amplitude trend at different height from the bottom in position 0 ($r = 0\,mm$), position 5 ($(r, \theta) = (50\,mm, 0°)$), position 19 ($(r, \theta) = (50\,mm, 90°)$), position 33 ($(r, \theta) = (50\,mm, 180°)$) and position 47 ($(r, \theta) = (50\,mm, 270°)$). Time domain $[24.9975\,s, 25.0025\,s]$. Pressure filtered at $[38\,kHz, 50\,kHz]$.

Due to the sinusoidal behavior of the total pressure over time at each position and height within the reactor, the maximum and minimum pressure amplitudes are, as expected, opposite in sign but not exactly equal in modulus. The amplitude values increase with height at all positions following a consistent trend. Notably, the symmetry property is preserved at different altitudes from the bottom of the reactor: positions 0, 5 and 33, which lie along the symmetry axis, exhibit amplitude values of the same order of magnitude ($10^{-11}\,Pa$) which are significantly lower than those at positions 19 and position 47 ($10^5\,Pa$).
Upon closer examination, the positions along the symmetry axis show variations in amplitude values, despite having similar trends: lowest consistently occur at $20\,mm$ from the bottom, with values of $\pm 2 \times 10^{-11}\,Pa$, $\pm 1.2 \times 10^{-11}\,Pa$ and $\pm 2.9 \times 10^{-11}\,Pa$ respectively at position 0, 5 and 33. Conversely, the highest amplitudes consistently occur at $40\,mm$ from the bottom, with values of $\pm 6.7 \times 10^{-11}\,Pa$, $\pm 4 \times 10^{-11}\,Pa$ and $\pm 9.5 \times 10^{-11}\,Pa$ respectively in position 0, 5 and 33.
For position 19 and 47 symmetry along the height is evident. At a height of $20\,mm$ the difference between the minimum and maximum amplitudes is $-0.2\,Pa$ for position 19 ($-1.14 \times 10^5\,Pa$ as minimum and $1.12 \times 10^5\,Pa$ as maximum) and $0.2\,Pa$ for position 47 ($-1.12 \times 10^5\,Pa$ as minimum and $1.14 \times 10^5\,Pa$ as maximum), obtained from the same values just reverted in sign. At $40\,mm$ from the bottom instead the difference in amplitudes is $0.05\,Pa$ at position 19 ($-3.87 \times 10^5\,Pa$ as minimum and $3.92 \times 10^5\,Pa$ as maximum) and $-0.05\,Pa$ at position 47 ($-3.92 \times 10^5\,Pa$ as minimum and $3.87 \times 10^5\,Pa$ as maximum). Not only does the absolute difference between amplitudes change with height, but the sign also reverses, indicating that while symmetry is maintained, it is inverted as the altitude changes, thereby shifting the phase of the pressure map.

4.2 Experimental set-up results

4.2.1 Pressure maps

In this subsection, the pressure maps generated from the measured acoustic signals in the sono-reactor are analyzed for both the case of water sonolysis and the sonolysis of the water-NiAlTi mixture.

As outlined in Subsection 3.3.2, the pressure map frames are selected for two time intervals: $[0\,s, 15\,s]$ (low power input) and $[35\,s, 50\,s]$ (high power input). More in detail, for each interval and mixture, the frames representing the time instant when the maximum and minimum pressure levels occur at the central position are selected, along with the frame where the pressure value is closest to zero at the midpoint of the interval (near $7.5\,s$ for the low power stimulation and near $42.5\,s$ for the high power stimulation).

Starting with the examination of water-sonolysis post processed data, Figures 4.10 and 4.11 illustrate the frame selection process just explained, for the low power input interval of time.

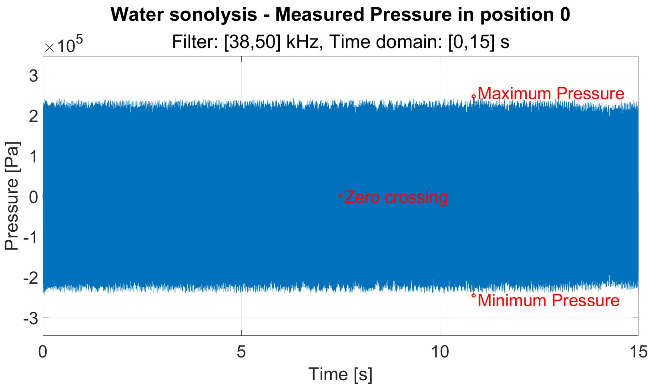

Figure 4.10: Measured water sonolysis pressure trend in position 0 ($r = 0\,mm$), time domain $[0\,s, 15\,s]$. Pressure filtered in $[38, 50]\,kHz$. Focus on the maximum pressure value ($t = 10.85104\,s$, $p = 2.47 \times 10^5\,Pa$), minimum pressure value ($t = 10.85105\,s$, $p = -2.46 \times 10^5\,Pa$) and the point closest to zero pressure value ($t = 7.49869\,s$, $p = 0.52\,Pa$).

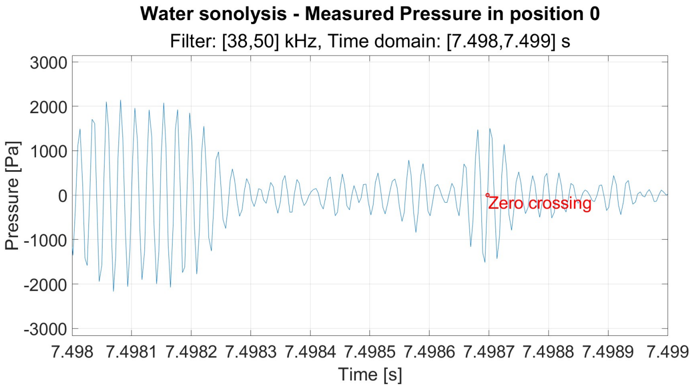

Figure 4.11: Measured water sonolysis pressure trend in position 0 ($r = 0\,mm$), time domain $[7.498\,s, 7.499\,s]$. Pressure filtered in $[38, 50]\,kHz$. Focus on the point closest to zero pressure value ($t = 7.49869\,s$, $p = 0.52\,Pa$).

Analyzing the zero crossing point from Figure 4.10, and more specifically from Figure 4.11 for a closer inspection, it occurs at $7.49869\,s$. The maximum and minimum pressure values instead occur within a difference of just $1 \times 10^{-5}\,s$. The maximum pressure, $2.47 \times 10^5\,Pa$, is reached at $10.85104\,s$, while the minimum, $-2.46 \times 10^5\,Pa$, occurs at $10.85105\,s$. Figures 4.12, 4.13 and 4.14 show the measured pressure maps for water sonolysis at $t = 7.49869\,s$, $t = 10.85104\,s$ and $t = 10.85105\,s$, respectively, corresponding to the instants just examined.

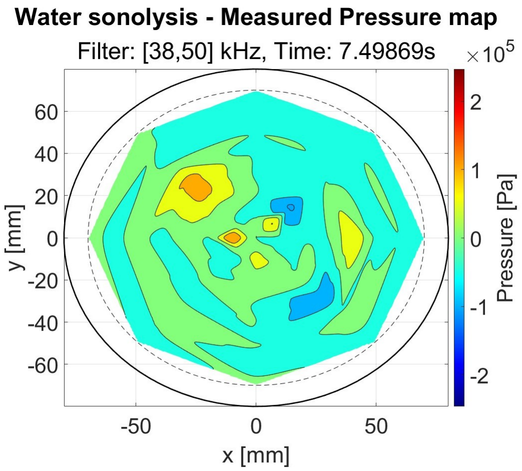

Figure 4.12: Measured water sonolysis pressure map at time $7.49869\,s$, instant in which is present the point closest to zero pressure value in position 0 ($0.52\,Pa$) in time domain $[0\,s, 15\,s]$.

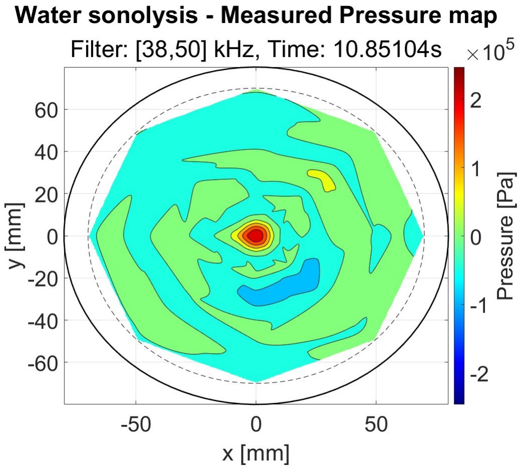

Figure 4.13: Measured water sonolysis pressure map at time $10.85104\,s$, instant in which is present the maximum pressure value in position 0 ($2.47 \times 10^5\,Pa$) in time domain $[0\,s, 15\,s]$.

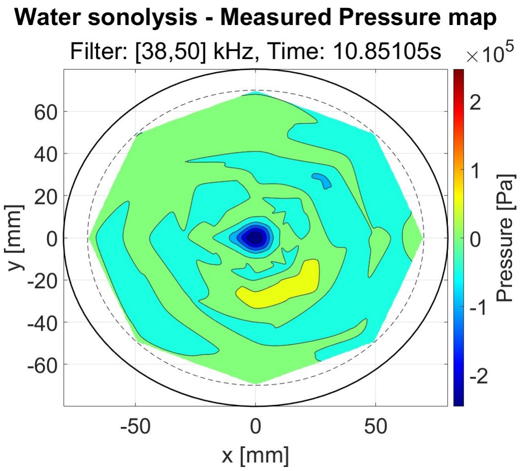

Figure 4.14: Measured water sonolysis pressure map at time $10.85105\,s$, instant in which is present the minimum pressure value in position 0 ($-2.46 \times 10^5\,Pa$) in time domain $[0\,s, 15\,s]$.

It is eye catching that the symmetries are not present in any of the displayed frames, and actually the pressure field varies significantly at each instant. Figures 4.13 and 4.14 are quite similar, with only minor differences in shape and a reversed sign of pressure at every point of the mesh.
Figure 4.15 shows the time-ordered sequence of frames just discussed, related to the water sonolysis in the first $15\,s$ of signal acquisition.

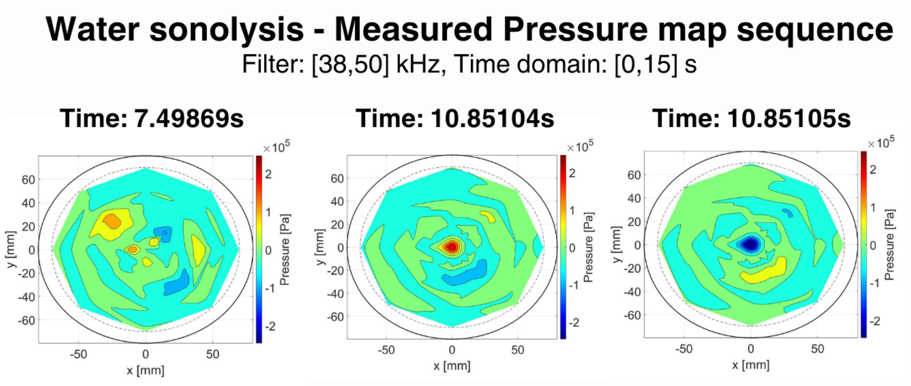

Figure 4.15: Measured water sonolysis pressure map, time-ordered frames sequence in the time domain $[0\,s, 15\,s]$.

The same frame selection approach is applied to water sonolysis under high power US stimulation. Figures 4.16 and 4.17 highlight the identification of the maximum, minimum and closest-to-zero pressure within the time interval $[35\,s, 50\,s]$.

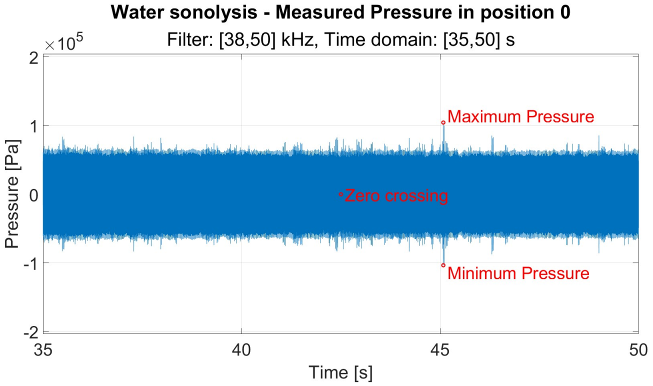

Figure 4.16: Measured water sonolysis pressure trend in position 0 ($r = 0\,mm$), time domain $[35\,s, 50\,s]$. Pressure filtered in $[38, 50]\,kHz$. Focus on the maximum pressure value ($t = 45.08098\,s$, $p = 1.04 \times 10^5\,Pa$), minimum pressure value ($t = 45.08099\,s$, $p = -1.03 \times 10^5\,Pa$) and the point closest to zero pressure value ($t = 42.50287\,s$, $p = 11.58\,Pa$).

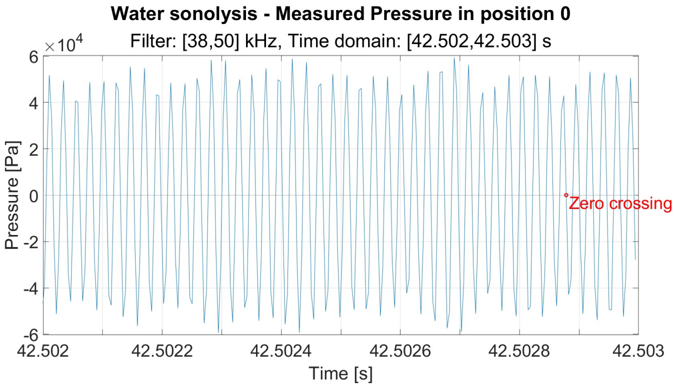

Figure 4.17: Measured water sonolysis pressure trend in position 0 ($r = 0\,mm$), time domain $[42.502\,s, 42.503\,s]$. Pressure filtered in $[38, 50]\,kHz$. Focus on the point closest to zero pressure value ($t = 42.50287\,s$, $p = 11.58\,Pa$).

Once again, the zero-crossing point selected near the $42.5\,s$ instant, as shown in detail in Figure 4.17, occurs at $42.50287\,s$. The maximum pressure ($1.04 \times 10^5\,Pa$) and minimum pressure ($-1.03 \times 10^5\,Pa$) occur at $t = 45.08098\,s$ and $t = 45.08099\,s$, respectively, with a difference of only $1 \times 10^{-5}\,s$ between them. It is noteworthy to compare these pressure levels, along with the entire pressure trend at the central position in Figure 4.16, to the pressure levels under low-power US stimulation presented in Figure 4.10: all the pressure peaks consequence of an high power input are lower in module (lower maxima and higher minima) respect those of low power input, and this holds true only for the central positions, as indicated by the pressure maps in the $[35\,s, 50\,s]$ interval (Figure 4.18, 4.19 and 4.20). A possible explanation of this phenomenon could be related to the interaction between the acoustic disturbance wave propagation and the formation and explosion of the cavitation bubble, which primarily arises in the central position, just above the transducer position of the sono-reactor. As anticipated, Figures 4.18, 4.19 and 4.20 present the pressure maps corresponding to the selected frames just discussed.

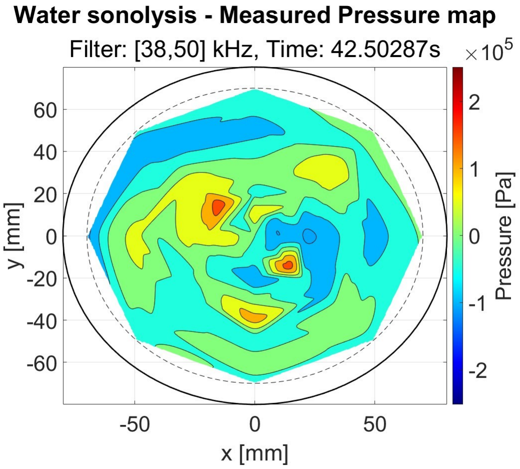

Figure 4.18: Measured water sonolysis pressure map at time $42.50287\,s$, instant in which is present the point closest to zero pressure value in position 0 $(11.58\,Pa)$ in time domain $[35\,s, 50\,s]$.

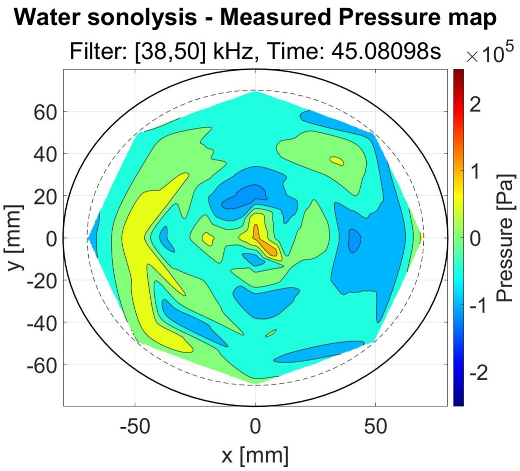

Figure 4.19: Measured water sonolysis pressure map at time $45.08098\,s$, instant in which is present the maximum pressure value in position 0 ($1.04 \times 10^5\,Pa$) in time domain $[35\,s, 50\,s]$.

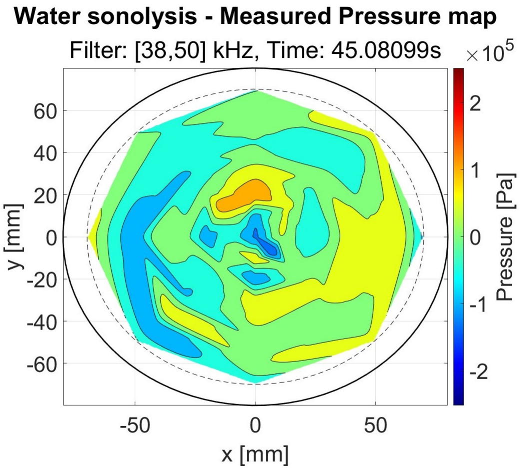

Figure 4.20: Measured water sonolysis pressure map at time $45.08099\,s$, instant in which is present the minimum pressure value in position 0 ($-1.03 \times 10^5\,Pa$) in time domain $[35\,s, 50\,s]$.

Noticeable is the fact that in all the three images of the reactor stimulated by the highest power level of the US transducer, the highest and lowest pressure levels are not located at the centre, but appear at random positions. Similar to the case of low power stimulation, the maximum and minimum pressures at the

centre occur within just $1 \times 10^{-5}\,s$ of each other, and the pressure map shapes remain comparable. However, aside from the change in sign of the pressure throughout the reactor, a closer examination of the pressure map shapes reveals more pronounced differences compared to the low power input case. This suggests that higher power US stimulation leads to sharper and more random pressure variations.
Figure 4.21 presents the time-ordered sequence of pressure map frames in the time interval $[35\,s, 50\,s]$.

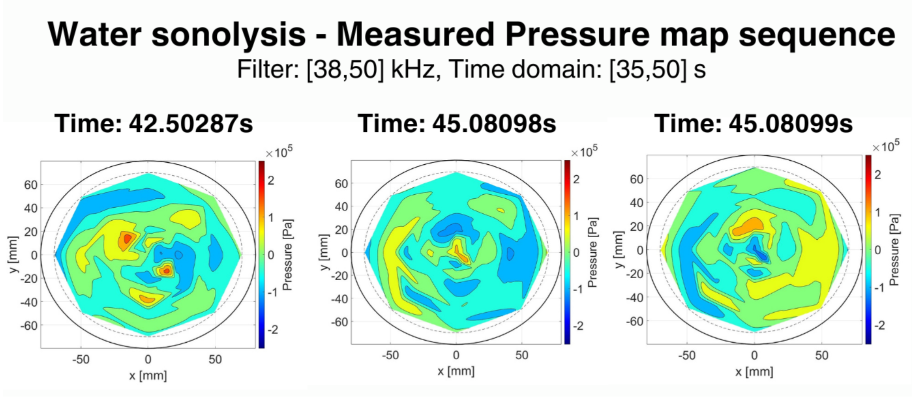

Figure 4.21: Measured water sonolysis pressure map, time-ordered frames sequence in the time domain $[35\,s, 50\,s]$.

The analysis of the acoustic field for the water-$NiAlTi$ mixture sonolysis follows the same procedure as outlined for the water sonolysis.
Focusing first on the $[0\,s, 15\,s]$ acquisition interval, characterized by the lowest transducer power induced in the sono-reactor, the selected frames are displayed in the time-domain pressure plots at the central position, as shown in Figures 4.22 and 4.23.

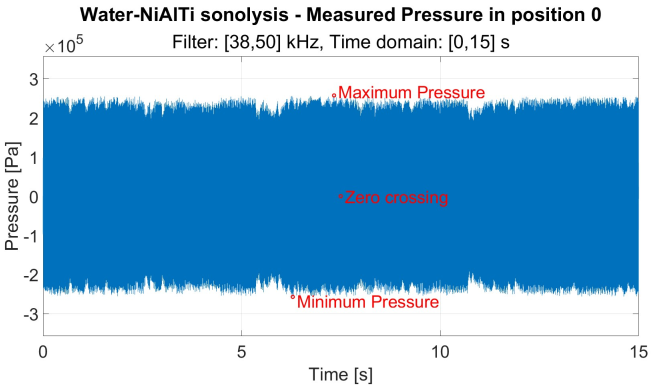

Figure 4.22: Measured water-$NiAlTi$ sonolysis pressure trend in position 0 ($r = 0\,mm$), time domain $[0\,s, 15\,s]$. Pressure filtered in $[38, 50]\,kHz$. Focus on the maximum pressure value ($t = 7.32893\,s$, $p = 2.57 \times 10^5\,Pa$), minimum pressure value ($t = 6.28915\,s$, $p = -2.57 \times 10^5\,Pa$) and the point closest to zero pressure value ($t = 7.49659\,s$, $p = 2.36\,Pa$).

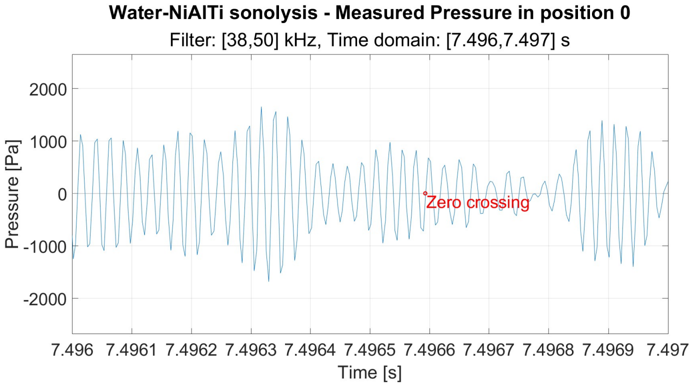

Figure 4.23: Measured water-$NiAlTi$ sonolysis pressure trend in position 0 ($r = 0\,mm$), time domain $[7.496\,s, 7.497\,s]$. Pressure filtered in $[38, 50]\,kHz$. Focus on the point closest to zero pressure value ($t = 7.49659\,s$, $p = 2.36\,Pa$).

The selected instant for the zero crossing of pressure occurs at $7.49659\,s$, while the minimum and maximum pressures at position 0 manifest at $6.28915\,s$ and $7.32893\,s$, respectively. The maximum pressure value in this case reaches $2.57 \times 10^5\,Pa$, while the minimum pressure is $-2.57 \times 10^5\,Pa$, suggesting that only a simple sign inversion occurred. However, the pressure maps presented in Figures 4.24, 4.25 and 4.26 challenge this hypothesis, as the pressure at all the other points in the reactor exhibits distinctly different behavior, with values that, at first glance, appear completely random.

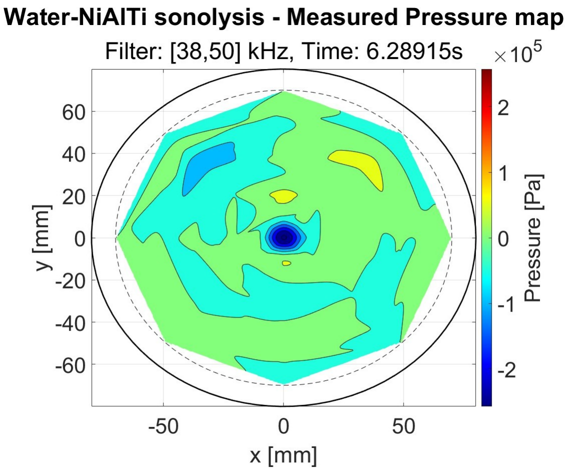

Figure 4.24: Measured water-$NiAlTi$ sonolysis pressure map at time $6.28915\,s$, instant in which is present the minimum pressure value in position 0 ($-2.57 \times 10^5\,Pa$) in time domain $[0\,s, 15\,s]$.

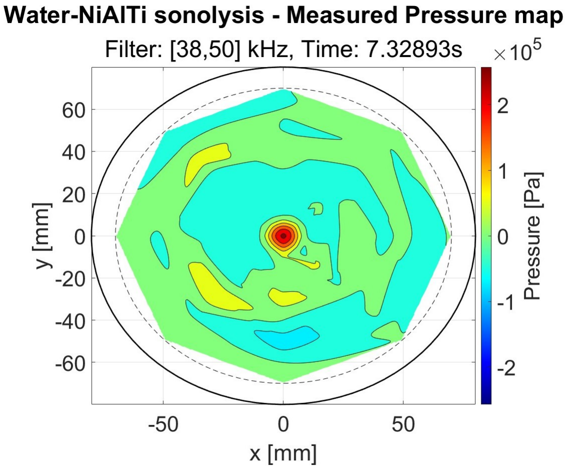

Figure 4.25: Measured water-$NiAlTi$ sonolysis pressure map at time $7.32893\,s$, instant in which is present the maximum pressure value in position 0 ($2.57 \times 10^5\,Pa$) in time domain $[0\,s, 15\,s]$.

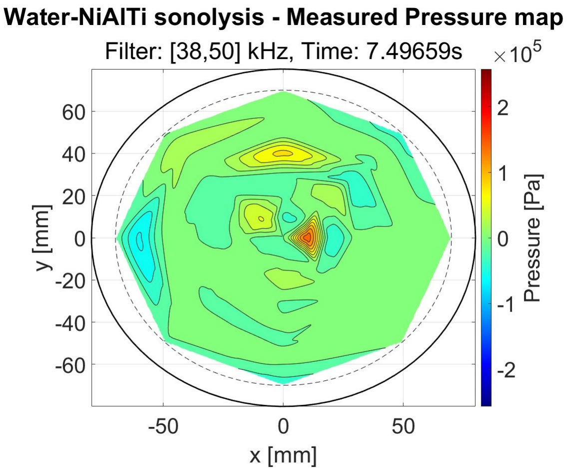

Figure 4.26: Measured water-$NiAlTi$ sonolysis pressure map at time $7.32893\,s$, instant in which is present the point closest to zero pressure value in position 0 ($2.36\,Pa$) in time domain $[0\,s, 15\,s]$.

While the pressure map shapes for the cases of maximum and minimum pressure occurrence do not exhibit significant differences compared to the low power water sonolysis, aside from the different time instants at which they occur, the slightly higher pressure values at the centre and a more concentrated peak near the central coordinates, the zero-crossing frame displays a more regular shape near the $0\,Pa$ pressure value (despite some scattered peaks in both positive and negative directions, with in particular one peak close the position 0). This pattern contrasts with the sonolysis involving only water presented in Figure 4.12, which is characterized by a more variable pressure behaviour.
Figure 4.27 represents the time-ordered pressure map frames for the low power water-$NiAlTi$ mix sonolysis.

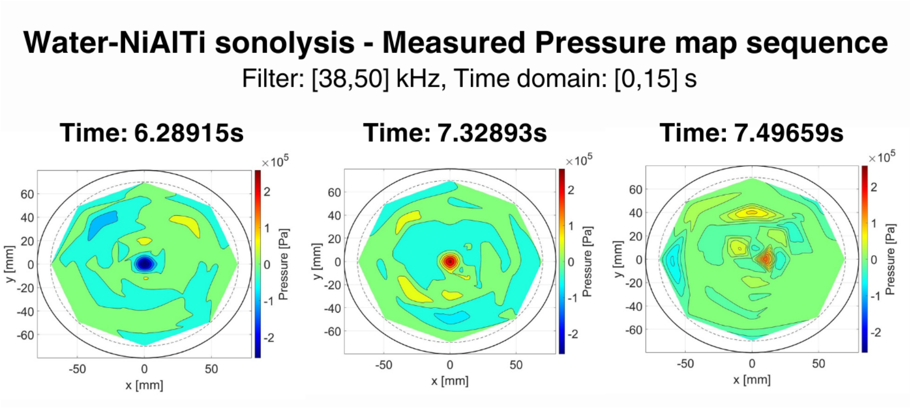

Figure 4.27: Measured water-$NiAlTi$ sonolysis pressure map, time-ordered frames sequence in the time domain $[0\,s, 15\,s]$.

Regarding the high power US-stimulated sonolysis of water mixed with the $NiAlTi$ photocatalyst, Figures 4.28 and 4.29 illustrate the filtered pressure signal at position 0, highlighting the selection of relevant instants.

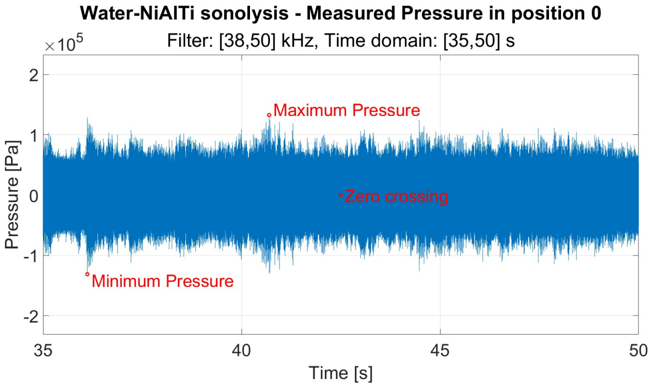

Figure 4.28: Measured water-$NiAlTi$ sonolysis pressure trend in position 0 ($r = 0\,mm$), time domain $[35\,s, 50\,s]$. Pressure filtered in $[38, 50]\,kHz$. Focus on the maximum pressure value ($t = 40.69485\,s$, $p = 1.33 \times 10^5\,Pa$), minimum pressure value ($t = 36.11560\,s$, $p = -1.31 \times 10^5\,Pa$) and the point closest to zero pressure value ($t = 42.49954\,s$, $p = 20\,Pa$).

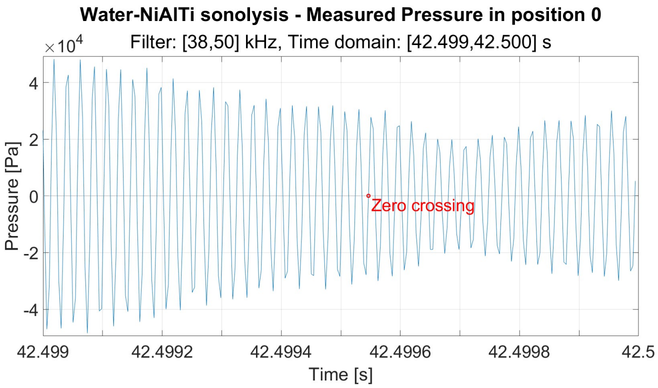

Figure 4.29: Measured water-$NiAlTi$ sonolysis pressure trend in position 0 ($r = 0\,mm$), time domain $[42.499\,s, 42.500\,s]$. Pressure filtered in $[38, 50]\,kHz$. Focus on the point closest to zero pressure value ($t = 42.49954\,s$, $p = 20\,Pa$).

The pressure value closest to zero at the centre occurs at $t = 42.49954\,s$, while the maximum pressure of $1.33 \times 10^5\,Pa$ is recorded at $t = 40.69485\,s$, and the minimum pressure of $-1.31 \times 10^5\,Pa$ occurs at $t = 36.11560\,s$. The increase in transducer power results in a reduction of pressure oscillations at the central position, similar to the behavior observed in the water-only case. Figures 4.30, 4.31 and 4.32 present the pressure map frames of the water-$NiAlTi$ sonolysis are shown.

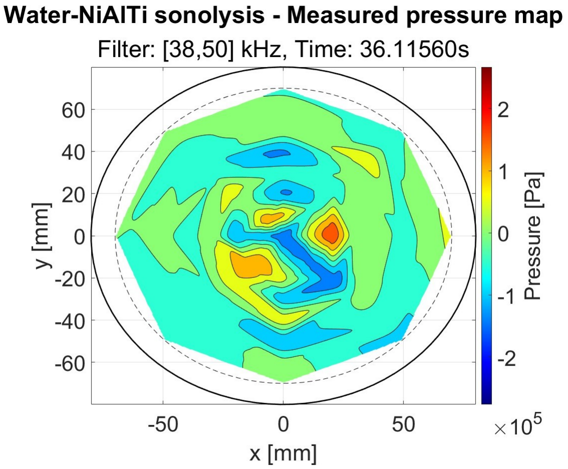

Figure 4.30: Measured water-$NiAlTi$ sonolysis pressure map at time $36.11560\,s$, instant in which is present the minimum pressure value in position 0 ($-1.31 \times 10^5\,Pa$) in time domain $[35\,s, 50\,s]$.

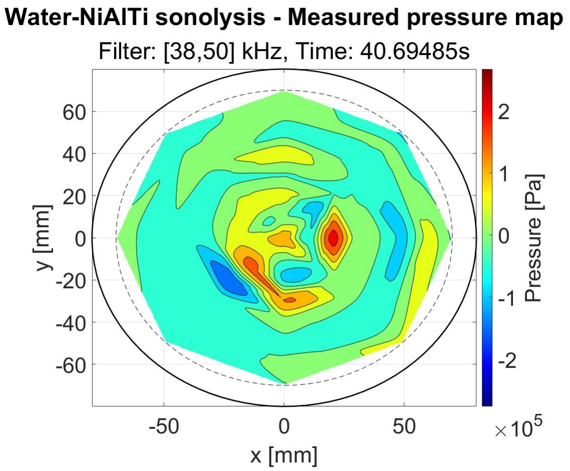

Figure 4.31: Measured water-$NiAlTi$ sonolysis pressure map at time $40.69485\,s$, instant in which is present the maximum pressure value in position 0 ($1.33 \times 10^5\,Pa$) in time domain $[35\,s, 50\,s]$.

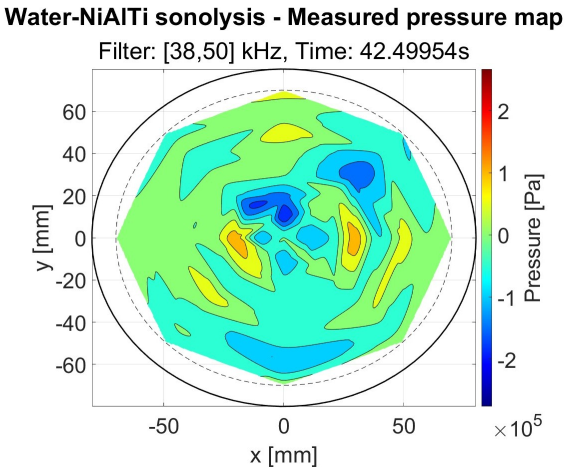

Figure 4.32: Measured water-$NiAlTi$ sonolysis pressure map at time $42.49954\,s$, instant in which is present the point closest to zero pressure value in position 0 ($20\,Pa$) in time domain $[35\,s, 50\,s]$.

The pressure maps for the high-power-induced sonolysis in water-photocatalyst mixture exhibit chaotic behaviour at all the three selected time steps, and in general the maximum and minimum pressure peaks are not located at the central position as it happens when the stimulation was characterized by a low

power input. The differences between the water sonolysis case and the water-$NiAlTi$ evidence just a different chaotic pressure trend within the reactor.
Figure 4.33 presents the time-ordered pressure map frames for the water-$NiAlTi$ sonolysis in the $[35\,s, 50\,s]$ time interval.

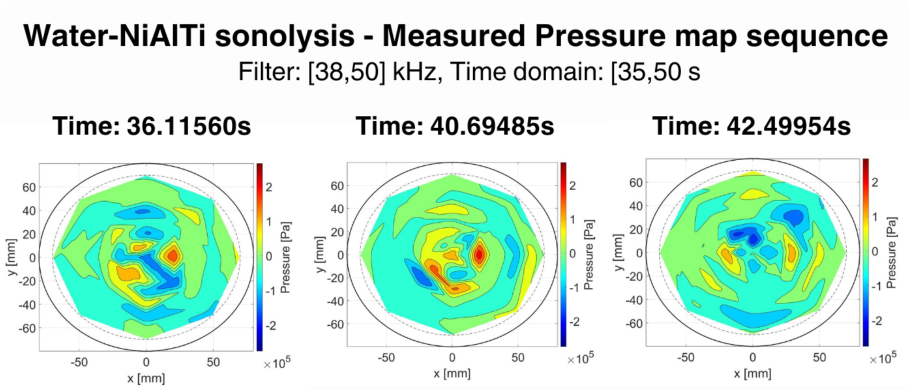

Figure 4.33: Measured water-$NiAlTi$ sonolysis pressure map, time-ordered frames sequence in the time domain $[35\,s, 50\,s]$.

4.2.2 Pressure-height plots

In this subsection, the post-processing pressure results are analyzed at various heights within the reactor, focusing solely on positions 0, 5, 19, 33 and 47. Specifically, the pressure-height plots highlight the maximum and minimum pressure amplitudes at each position and height, retrieved at the same time instants analyzed in Section 4.2.1, for both low and high US transducer power inputs.
Figures 4.34 and 4.35 display the maximum and minimum pressure amplitude plots across different heights and positions for the case of water sonolysis.

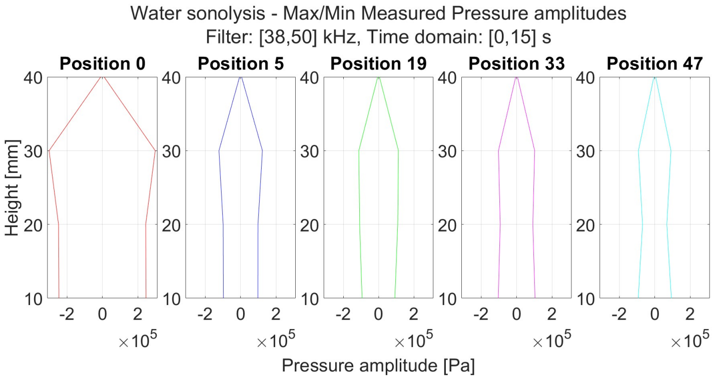

Figure 4.34: Measured water sonolysis maximum and minimum pressure amplitude trend at different height from the bottom in position 0 ($r = 0\,mm$), position 5 ($(r, \theta) = (50\,mm, 0°)$), position 19 ($(r, \theta) = (50\,mm, 90°)$), position 33 ($(r, \theta) = (50\,mm, 180°)$) and position 47 ($(r, \theta) = (50\,mm, 270°)$). Time domain $[0\,s, 15\,s]$. Pressure filtered at $[38\,kHz, 50\,kHz]$.

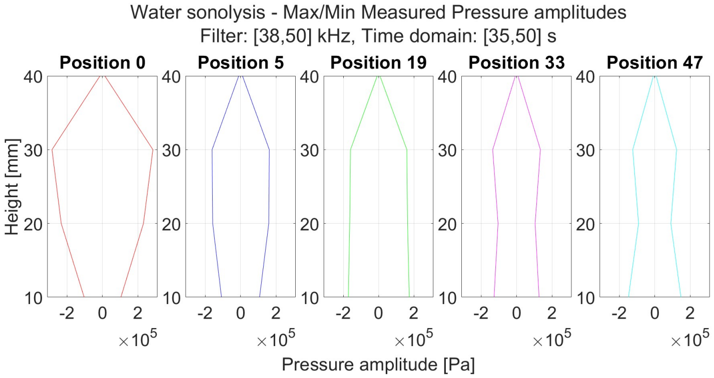

Figure 4.35: Measured water sonolysis maximum and minimum pressure amplitude trend at different height from the bottom in position 0 ($r = 0\,mm$), position 5 ($(r, \theta) = (50\,mm, 0°)$), position 19 ($(r, \theta) = (50\,mm, 90°)$), position 33 ($(r, \theta) = (50\,mm, 180°)$) and position 47 ($(r, \theta) = (50\,mm, 270°)$). Time domain $[35\,s, 50\,s]$. Pressure filtered at $[38\,kHz, 50\,kHz]$.

The first notable observation, applicable to both the $[0\,s, 15\,s]$ and $[35\,s, 50\,s]$ intervals, is that the pressure amplitudes across different heights in all examined positions and time domains share approximately the same trend, characterized by a relatively stable pressure between $10\,mm$ and $30\,mm$ from the bottom, typically reaching its peak amplitude at $30\,mm$, and a sharp reduction towards very low pressure amplitudes at $40\,mm$, just $10\,mm$ below the water surface.

Position 0 is the one that exhibits the highest pressure amplitudes within the reactor, indicating a greater pressure oscillation over time (despite its random nature), with the maximum amplitude located at $30\,mm$ that is $\pm 3 \times 10^5\,Pa$ in the low power stimulation case, while $\pm 2.8 \times 10^5\,Pa$ in the high power stimulation case. As noted in Section 4.2.1, position 0 experiences a reduction in pressure oscillation when the US transducer power is increased, whereas other positions show an increase in pressure amplitude with stronger US stimulation.

The situation is similar for the water-$NiAlTi$ sonolysis, as evidenced by Figures 4.36 and 4.37.

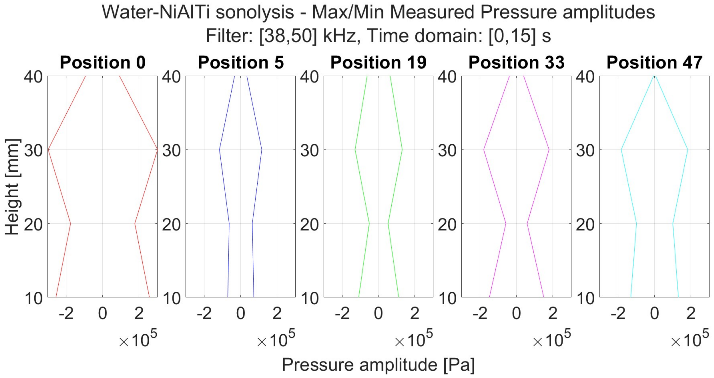

Figure 4.36: Measured water-$NiAlTi$ sonolysis maximum and minimum pressure amplitude trend at different height from the bottom in position 0 ($r = 0\,mm$), position 5 ($(r,\theta) = (50\,mm, 0°)$), position 19 ($(r,\theta) = (50\,mm, 90°)$), position 33 ($(r,\theta) = (50\,mm, 180°)$) and position 47 ($(r,\theta) = (50\,mm, 270°)$). Time domain $[0\,s, 15\,s]$. Pressure filtered at $[38\,kHz, 50\,kHz]$.

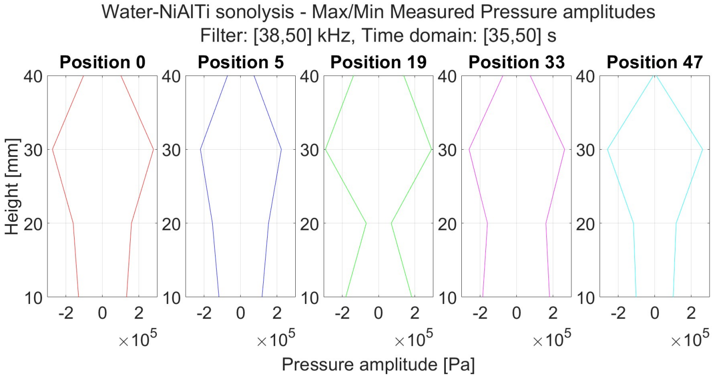

Figure 4.37: Measured water-$NiAlTi$ sonolysis maximum and minimum pressure amplitude trend at different height from the bottom in position 0 ($r = 0\,mm$), position 5 ($(r,\theta) = (50\,mm, 0°)$), position 19 ($(r,\theta) = (50\,mm, 90°)$), position 33 ($(r,\theta) = (50\,mm, 180°)$) and position 47 ($(r,\theta) = (50\,mm, 270°)$). Time domain $[35\,s, 50\,s]$. Pressure filtered at $[38\,kHz, 50\,kHz]$.

The maximum and minimum pressure amplitude trends with height are nearly identical to those observed in the case of water sonolysis, with the exception of a more pronounced reduction in amplitude at $20\,mm$ from the bottom in positions 19 and 33. The highest amplitude consistently occurs at $30\,mm$ from the bottom, and the position 0 displaying the largest values, reaching $\pm 3 \times 10^5\,Pa$ in the$[0\,s, 15\,s]$ interval and $\pm 2.7 \times 10^5\,Pa$ in the $[35\,s, 50\,s]$ interval. Notably, as shown in Figure 4.37, under the maximum US power, the highest amplitude is not found at position 0, as it was in the case of water sonolysis (even after the reduction in pressure oscillation at higher power regimes), but instead at position 19, with a value of $\pm 2.9 \times 10^5\,Pa$. Overall, all the positions, except the centre, show significantly higher pressure amplitudes with increased power input, and this effect is more pronounced when the mixture subjected to sonolysis is water-$NiAlTi$ rather than pure water.

The analysis of the pressure trends with height suggest the presence of a multi-layer cavitation field within the cylindrical sono-reactor, and this phenomenon warrants further investigations to fully understand its potential.

4.3 Comparison between simulation results and experimental set-up results

This section focuses is on the differences between the simulated results and the data acquired and post-processed from a real cylindrical reactor. Understanding these discrepancies is crucial in assessing whether this type of simulation, currently the most widely used in literature, is reliable in predicting the real sonolysis behaviour, the acoustic pressure field and the formation and collapse of the cavitation bubbles.

Firstly, it is important to note, comparing Figure 4.10 and 4.22 with Figure 4.4, as well as Figure 4.16 and 4.28 with Figure 4.4, that the simulated pressure in the time domain appears more regular than the measured pressure, that exhibits more randomness, despite being filtered within the $[38, 50]\,kHz$ spectrum range while the simulated pressure is constructed from all the modal components within the same frequency range. Furthermore, the measured signals respond differently to changes in the US input power, whereas the simulated pressure does not vary with different power inputs. These comparative results are displayed in Figures 4.38 and 4.39

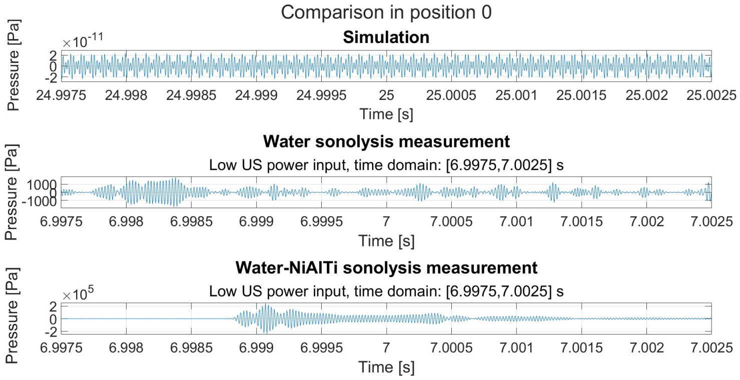

Figure 4.38: Comparison between pressure signals in position 0. The measured pressures are analyzed for a restricted time domain of $0.005\,s$ —$[6.9975, 7.0025]\,s$ —.

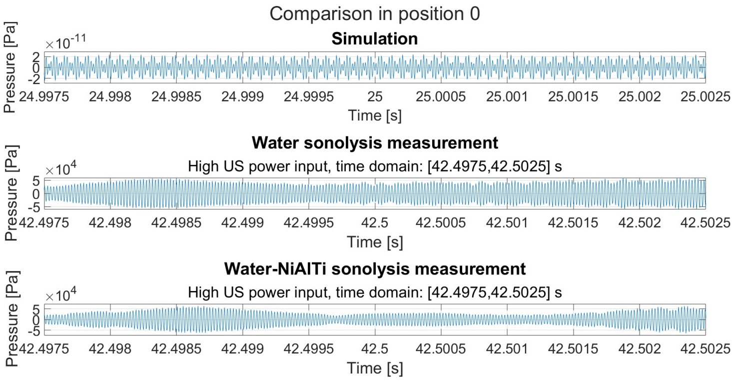

Figure 4.39: Comparison between pressure signals in position 0. The measured pressures are analyzed for a restricted time domain of $0.005\,s$ — $[42.4975, 42.5025]\,s$ —.

Another critical comparison arises when examining the differences between the pressure maps: across all comparisons (whether between simulated and measured pressure maps at zero crossing frames, maximum peak pressure or minimum peak pressure frames, for both low and high power stimulation) the most significant discrepancy relates to the symmetry. In the simulations, every results consistently exhibits symmetry along a diameter, for every possible frame selection and at every instant of the simulation. Differently, the measured data shows no symmetry at all, and generally the acoustic pressure field behaves in a completely random manner.

In the simulated pressure maps, maximum and minimum peaks are always specular in position 11 $(r, \theta) = (40\,mm, 45°)$ and position 55 $(r, \theta) = (40\,mm, 315°)$, as shown in Figures 4.3 and 4.7. However, in real experiments, the maximum and minimum pressure peaks always occur in random positions within the sonoreactor, making it impossible to predict where the acoustic pressure will reach significant amplitudes and potentially lead to bubbles formation. Figures 4.40 and 4.41 effectively summarize this concept.

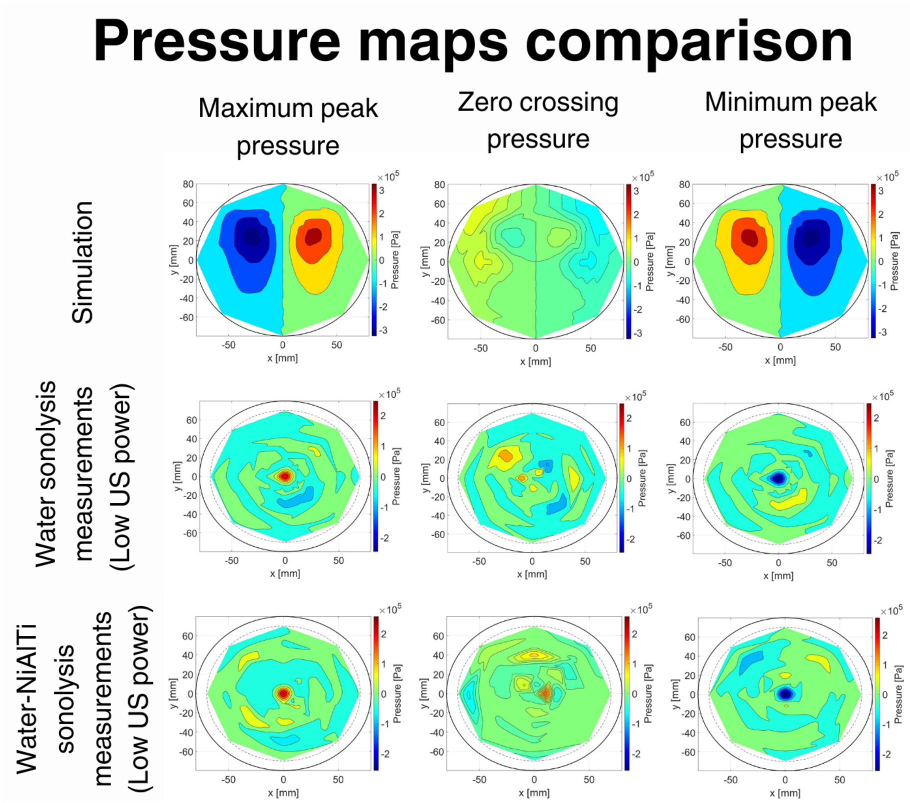

Figure 4.40: Pressure maps comparison. The measured maps are selected in the time domain $[0, 15]\,s$, when the reactor is stimulated by low US power.

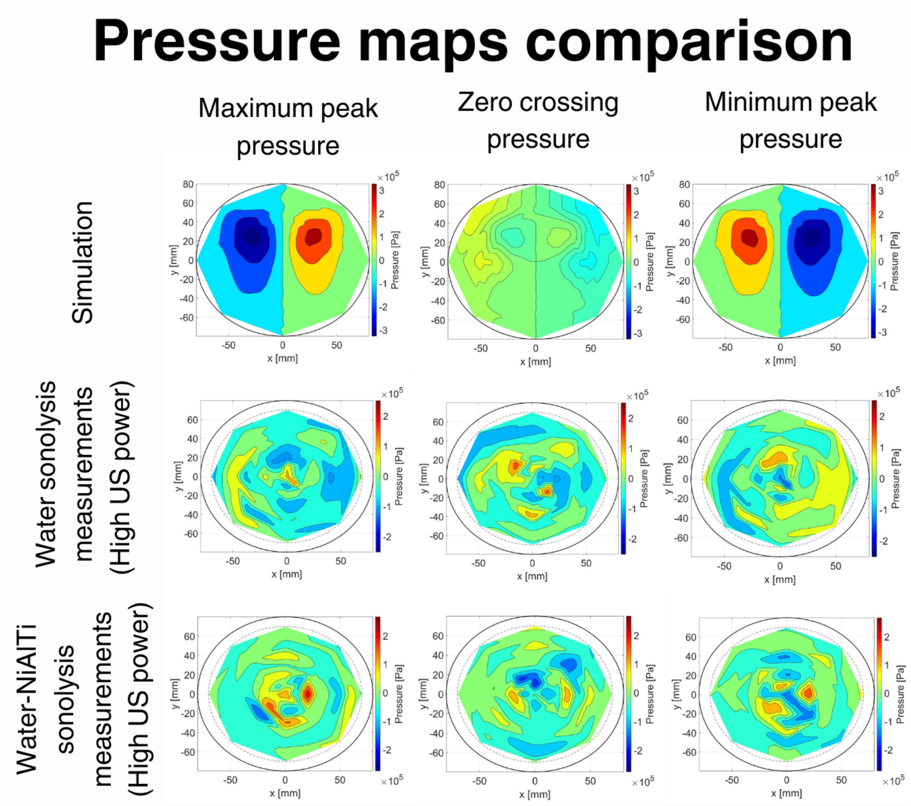

Figure 4.41: Pressure maps comparison. The measured maps are selected in the time domain $[35, 50]\,s$, when the reactor is stimulated by high US power.

The symmetric outcome of the simulation arises from the modal analysis described in Section 3.2, where the pressure behavior is largely dictated by the geometry of the reactor. Given the cylindrical symmetry of the sono-reactor, the simulation results inherently exhibit symmetry as a direct consequence of the mathematical model. However, the comparison presented in this section highlights that the influence of reactor geometry on the ultrasonic acoustic field, particularly in the context of cavitation phenomena, may not accurately reflect real-world conditions.

Lastly, a comparison can be drawn between the pressure-height plots, specifically between Figure 4.9 with Figures 4.34 and 4.36 or between Figure 4.9 and Figures 4.35 and 4.37. The only similarity between the simulation results and the measurements is that both indicate that the $20\,mm$ height from the bottom acts as a bottleneck for the maximum and minimum pressure amplitudes. However, while the simulations associate this height with the minimum oscillation amplitude possible, the measurements consistently show the real minimum at

$40\,mm$, the position closest to the top surface of the liquid. At this height, where the simulations display their maximum pressure amplitude, the real data shows the lowest pressure oscillation. Additionally, while in the measurements the pressure amplitudes in all analyzed positions share the same order of magnitude ($10^5\,Pa$), and reveal no detectable symmetries along the height, the simulation results show a distinct behavior: the amplitude varies across the positions, and at positions 5, 0 and 33 the amplitude remains in the order of $10^{-11}\,Pa$, while positions 19 and 47 exhibit an amplitude in the order of $10^5\,Pa$. Moreover, the simulation suggests a specular relationship between positions 19 and 47, which is absent in the experimental data. Figures 4.42 and 4.43 highlight the comparison along different height.

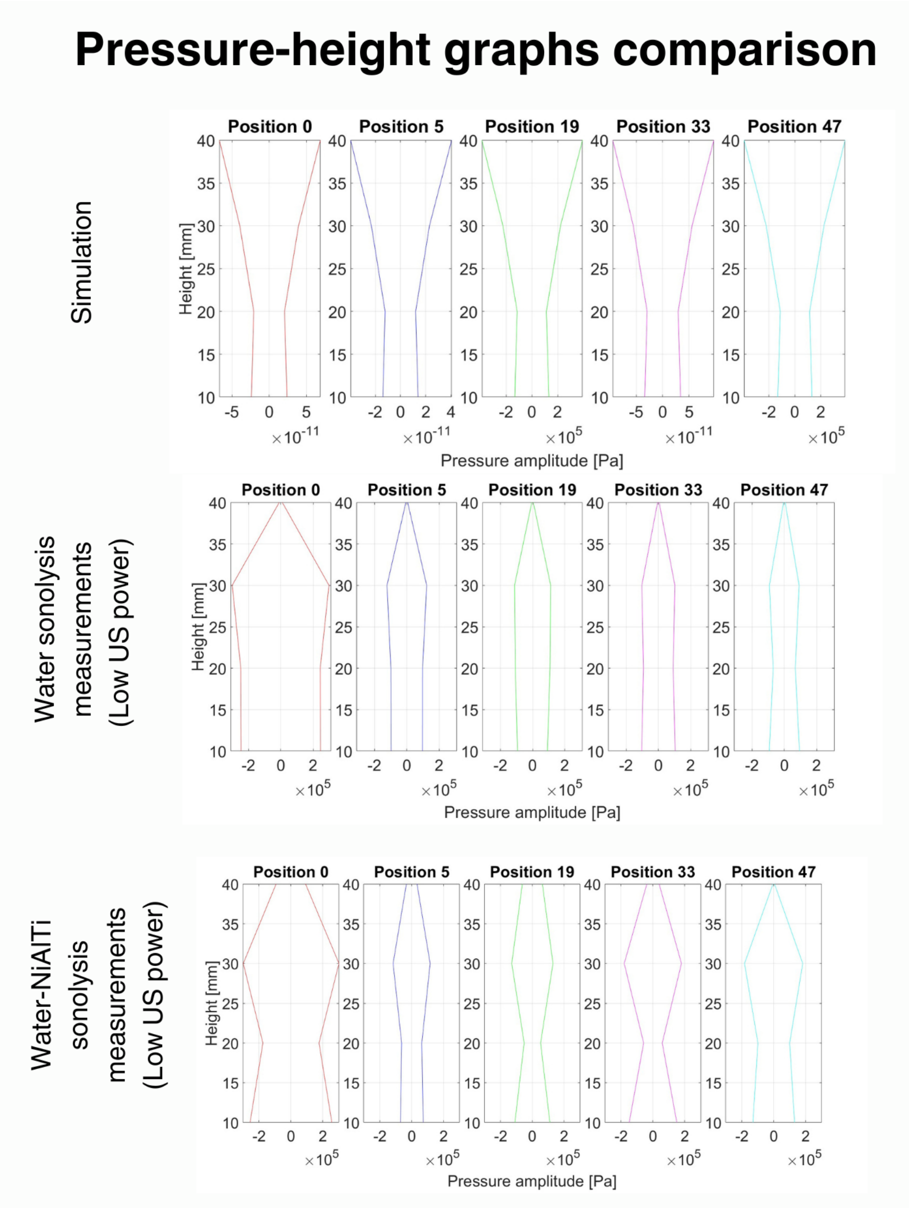

Figure 4.42: Pressure-height graphs comparison. The measured pressure-height plots are evaluated in the time domain $[0, 15]\, s$, when the reactor is stimulated by low US power.

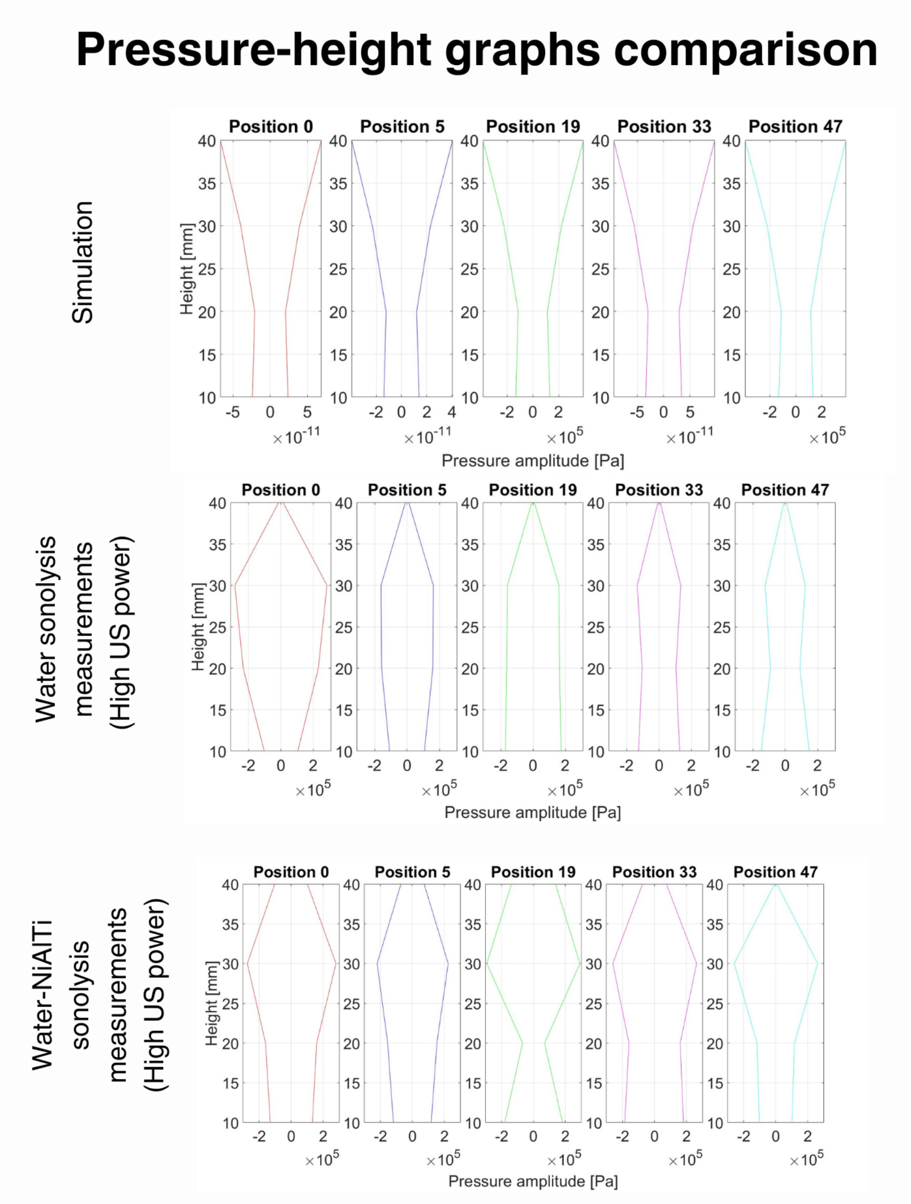

Figure 4.43: Pressure-height graphs comparison. The measured pressure-height plots are evaluated in the time domain $[35, 50]\,s$, when the reactor is stimulated by high US power.

4.4 Conclusions

Following the analysis of the results derived from the simulation procedure outlined in Section 4.1, the experimental set-up results analysis discussed in Section 4.2 and the comparative assessment between these two different procedures presented in Section 4.3, it is evident that the current approach to sonolysis simulation, based on the mathematical model described in Section 3.2 and widely spread in the existing literature, does not conform to the experimental observations obtained for both water and water-NiAlTi sonolysis within a cylindrical sono-reactor.

The discrepancies observed between the simulation results and the experimental data can be attributed to several simplifying assumptions inherent the mathematical model employed for the simulations: the assumption of Laplace's hypothesis — all fluid compression or expansion processes occur isentropically, thereby neglecting any internal heat flow —, the ideal fluid assumption — the model treats the fluid as ideal and devoid of viscosity, which precludes the ability to distinguish between the different fluids undergoing sonolysis —, the linear approximation of acoustic relations — that may not adequately capture the complexities of real-world acoustic phenomena —, the Neumann boundary condition for the top and bottom circular surfaces — considered as rigid implies a perfect reflection of the acoustic wave and zero normal velocity —, the Robin boundary condition for the lateral walls — considered as rigid and imprinting a phase shift on the acoustic pressure oscillation —, the use of an approximated speed of sound, the assumption of constant amplitude pressure harmonics — that may not represent the variability encountered in experimental conditions —, the assumption of a constant phase shift for azimuthal modes — with the consequent neglecting of the complexities associated with phase variations in real systems —, the use of numerical approximations for radial modes — which can induce errors in the results —, the consideration of limited number of radial and azimuthal modes — made to reduce the computational burden, but this may sacrifice accuracy —.

To enhance the alignment between simulation results and experimental evidence, it is imperative to modify or eliminate several of these assumptions. Potential strategies for improvement include:

1. Removal of the ideal fluid hypothesis: incorporating the viscosity of the fluid mixtures being subjected to acoustic disturbances would allow for a more accurate characterization of fluid response;
2. Acknowledging the effects that may emerge from ultrasonic stimulation can provide a more holistic understanding of the process;
3. Consideration of acoustic scattering that may arise when the pressure waves interacts with cavitation bubble creation, motion and implosion;
4. Integration of advanced modeling frameworks: employing sophisticated modeling approaches, such as molecular-scale computational models, could yield insights better suited for analyzing sonochemistry.

In conclusion, further research is essential to deepen the understanding of the acoustic pressure field within a reactor, maybe experimenting with the same methodology exposed in this thesis on different geometrical shape reactors that present an evident symmetry and potential influence of the modal response, as for squared or cylindrical sections. This understanding will elucidate the potential of sonolysis and explore its synergies with photolysis and the more established electrolysis processes. By addressing the identified discrepancies and refining the simulation methodologies, it is possible to enhance the predictive capabilities of sonolysis models and optimize their applications in various chemical processes.

Bibliography

[1] URL: `https://www.rsc.org/periodic-table/element/1/hydrogen`. (accessed: 26/07/2024).

[2] URL: `https://afdc.energy.gov/files/pdfs/hyd_economy_bossel_eliasson.pdf`. (accessed: 02/08/2024).

[3] URL: `https://www.gartner.com/en/information-technology/glossary/hydrogen-economy`. (accessed: 02/08/2024).

[4] URL: `https://ec.europa.eu/eurostat/web/interactive-publications/energy-2024#energy-sources`. (accessed: 12/08/2024).

[5] URL: `https://energy.ec.europa.eu/topics/energy-systems-integration/hydrogen_en`. (accessed: 12/08/2024).

[6] Rona Aldo. “The acoustic resonance of rectangular and cylindrical cavities”. In: *Journal of Algorithms Computational Technology* (2007).

[7] Aissa Dehane; Slimane Merouani; Oualid Hamdaoui; Muthupandian Ashokkumar. “An alternative technique for determining the number density of acoustic cavitation bubbles in sonochemical reactors”. In: *Ultrasonics Sonochemistry* (2022).

[8] Mathieu Legay; Nicolas Gondrexon; Stéphane Le Person; Primius Boldo; André Bontemps. “Enhancement of Heat Transfer by Ultrasound: Review and Recent Advances”. In: *International Journal of Chemical Engineering* (2011).

[9] P. Domenighini; A.M. Gambelli; F. Rossi; F. Cotana. “Hydrogen production by water photo-sonolysis: a modal approach to enhance the ultrasonic acoustic field in the solution”. In: *Journal of Physics: Conference Series* (2023).

[10] Piergiovanni Domenighini; Ferdinando Costantino; Pier Luigi Gentili; Anna Donnadio; Morena Nocchetti; Alceo Macchioni; Federico Rossi; Franco Cotana. “Future perspectives in green Hydrogen production by catalyzed sono-photolysis of water”. In: *Sustainable Energy Fuels* (2024).

[11] P.R. Gogate; S. Shaha; L. Csoka. “Intensification of cavitational activity in the sonochemical reactors using gaseous additives”. In: *Chemical Engineering Journal* (2014).

[12] Godula-Jopek Agata; Stolten Detlef. “Hydrogen production by electrolysis”. In: Weinheim : Wiley-VCH, 2015. Chap. 1. Introduction.

[13] Godula-Jopek Agata; Stolten Detlef. “Hydrogen production by electrolysis”. In: Weinheim : Wiley-VCH, 2015. Chap. 2. Fundamentals of Water Electrolysis.

[14] International Renewable Energy Agency; Abu Dhabi. *Green hydrogen strategy: A guide to design.* Tech. rep. IRENA, 2024.

[15] Stolten Detlef; Bernd Emonts. “Hydrogen Science and Engineering”. In: Weinheim : Wiley-VCH, 2015. Chap. 5. Solar Thermal Water Decomposition.

[16] Slimane Merouani; Oualid Hamdaoui; Yacine Rezgui; Miloud Guemini. “Computational engineering study of hydrogen production via ultrasonic cavitation in water”. In: *International Journal of Hydrogen Energy* (2016).

[17] Slimane Merouani; Oualid Hamdaoui. “The size of active bubbles for the production of hydrogen in sonochemical reaction field”. In: *Ultrasonics Sonochemistry* (2016).

[18] Hottinger Brüel & Kjær. *Transducers: Hydrophone Types 8103, 8104, 8105 and 8106.* 2021.

[19] Christian Koch. “Sound field measurement in a double layer cavitation cluster by rugged miniature needle hydrophones”. In: *Ultrasonics Sonochemistry, Volume 29* (2016).

[20] Sandip Mazumder. “Numerical Methods for Partial Differential Equations: Finite Difference and Finite Volume Methods”. In: Academic Press, 2016. Chap. 2. The Finite Difference Method.

[21] Allan D. Pierce. “Acoustics: An Introduction to Its Physical Principles and Applications”. In: Springer Nature, 2019. Chap. 1. The Wave Theory of Sound.

[22] Md H. ISlam; Odne S. Burheim; Bruno G. Pollet. “Sonochemical and sonoelectrochemical production of hydrogen”. In: *Ultrasonics - Sonochemistry* (2019).

[23] Sherif S. Rashwan; Ibrahim Dincer; Atef Mohany; Bruno G. Pollet. “The Sono-Hydro-Gen process (Ultrasound induced hydrogen production): Challenges and opportunities”. In: *International Journal of Hydrogen Energy* (2019).

[24] Franco Cotana; Federico Rossi. In: *3rd international green energy Conference.* 2007.

[25] Massimo Santarelli. “Proprietà H2 ed esigienze FC”. ’Polygeneration and Advanced Energy Systems’ lecture taken @ Politecnico di Torino in 02/12/2022.

[26] Başak Savun-Hekimoğlu. “A Review on Sonochemistry and Its Environmental Applications”. In: *Acoustics* (2020).

[27] Zongsu Wei; Linda K. Weavers. “Combining COMSOL modeling with acoustic pressure maps to design sono-reactors”. In: *Ultrasonics Sonochemistry* (2016).